Robotic farming on marginal, highly sloped lands

by

Chetan Manik Badgujar

B.Tech., Dr. P.D.K.V., Akola, India, 2015

M.Tech., Punjab Agricultural University, India, 2017

AN ABSTRACT OF A DISSERTATION

submitted in partial fulfillment of the
requirements for the degree

DOCTOR OF PHILOSOPHY

Carl and Melinda Helwig Department of Biological and Agricultural Engineering
Carl R. Ice College of Engineering

KANSAS STATE UNIVERSITY
Manhattan, Kansas

2022

Abstract

One of the most pressing issues of our time is how to feed around 9.7 billion people by 2050. Cropland expansion is one of the leading factors in global agricultural production growth to meet the rising demands of an escalating population. Arable steep grassland, hills or uneven terrain present difficulties to farming with large conventional agriculture machinery and equipment's. The current technology is unsafe and unsuitable to operate on sloping terrain. This technological barrier to slope farming has prevented thousands of hectares of arable land from being cultivated, primarily in the United States Great Plains region. Therefore, we proposed a fleet of small Autonomous Ground Vehicles (AGVs) to expand farming to marginal, uneven, and highly sloped terrain. The proposed fleet aims to perform the essential agricultural operations ranging from seeding to harvesting on sloping terrain. The research aimed to explore the potential, capabilities, and limitations of small ground vehicles to perform the sloped crop work. The dissertation consisted of five chapters. The first chapter introduced the undertaken problem, background, and proposed solution. It also outlined the included chapters with goals and significance.

The second chapter laid the foundation of a multi-AGV fleet by determining the single AGV's suitability and capabilities and by quantifying its physical limits for sloped crop work in a controlled soil bin setup. A standard drawbar pull test was performed in a soil bin to evaluate the AGV's performance against the varying slope, speed, and drawbar. The AGV delivered optimum power efficiency and generated enough drawbar pull with optimum travel reduction. The results found that the prototype AGV can successfully operate on slopes up to 18°, indicating that high-sloped terrain or hills could be farmed with the proposed system.

The vehicle behavior models in a sloping environment are essential for fleet operation, path planning, and developing a control algorithm. Hence, Chapter 3 aimed to develop the AGV's behavior models from laboratory soil bin data. Artificial neural network (ANN)

models were developed. Shallow ANNs were fast, accurate, and reliable tools to predict AGV behavior in a controlled laboratory setup (i.e., sloped soil bin). The predictive AGV's behavior model from a control laboratory setup proved to be an excellent starting point for optimizing the vehicle control parameters. However, these models cannot be extended to predict the AGV's behavior in a continuously varying slope environment. Therefore, Chapter 4 aimed to develop machine learning-based models on data collected from a real-field environment. Machine learning and deep learning-based models were developed and analyzed. The study found that the deep neural networks (DNN) model was well-suited for predicting the AGV's behavior in a sloped, real-field environment. Chapters 3 and 4 explored the capabilities of an artificial intelligence methods to simulate the AGV's behavior on sloping terrain. The developed models predicted the AGV's specific dynamic response, including traction, slip, and energy from the inputs of AGV's velocity, applied load, and slope.

A small and lightweight AGV was unable to provide the downforce and drawbar required for a traditional seeder. Hence, these AGVs would need a specialized robotic grain drill. The feed mechanism is the heart of the grain drill, and its design and performance influence the plant population and crop yield. Therefore, Chapter 5 aimed to design and develop a screw auger type feed mechanism. The feed mechanism was developed and tested in a laboratory setup against speed, vibration, and slope as control variables. The study delivered a bulk feed mechanism for wheat drilling, which can be easily scaled and adopted by small autonomous vehicles or mobile robots.

The dissertation laid the foundation for robotic farming on the sloped terrain, and the envisioned multi-AGV fleet may provide a valid solution to farm the arable uneven, highly sloped terrain. The findings provide a groundwork for robotics and automation, which has the potential to solve the emerging problems in the food production system by producing food, fuel, and fiber for the growing population.

Robotic farming on marginal, highly sloped lands

by

Chetan Manik Badgujar

B.Tech., Dr. P.D.K.V., Akola, India, 2015

M.Tech., Punjab Agricultural University, India, 2017

A DISSERTATION

submitted in partial fulfillment of the
requirements for the degree

DOCTOR OF PHILOSOPHY

Carl and Melinda Helwig Department of Biological and Agricultural Engineering
Carl R. Ice College of Engineering

KANSAS STATE UNIVERSITY
Manhattan, Kansas

2022

Approved by:

Major Professor
Daniel Kent Flippo

Copyright

Abstract

One of the most pressing issues of our time is how to feed around 9.7 billion people by 2050. Cropland expansion is one of the leading factors in global agricultural production growth to meet the rising demands of an escalating population. Arable steep grassland, hills or uneven terrain present difficulties to farming with large conventional agriculture machinery and equipment's. The current technology is unsafe and unsuitable to operate on sloping terrain. This technological barrier to slope farming has prevented thousands of hectares of arable land from being cultivated, primarily in the United States Great Plains region. Therefore, we proposed a fleet of small Autonomous Ground Vehicles (AGVs) to expand farming to marginal, uneven, and highly sloped terrain. The proposed fleet aims to perform the essential agricultural operations ranging from seeding to harvesting on sloping terrain. The research aimed to explore the potential, capabilities, and limitations of small ground vehicles to perform the sloped crop work. The dissertation consisted of five chapters. The first chapter introduced the undertaken problem, background, and proposed solution. It also outlined the included chapters with goals and significance.

The second chapter laid the foundation of a multi-AGV fleet by determining the single AGV's suitability and capabilities and by quantifying its physical limits for sloped crop work in a controlled soil bin setup. A standard drawbar pull test was performed in a soil bin to evaluate the AGV's performance against the varying slope, speed, and drawbar. The AGV delivered optimum power efficiency and generated enough drawbar pull with optimum travel reduction. The results found that the prototype AGV can successfully operate on slopes up to 18°, indicating that high-sloped terrain or hills could be farmed with the proposed system.

The vehicle behavior models in a sloping environment are essential for fleet operation, path planning, and developing a control algorithm. Hence, Chapter 3 aimed to develop the AGV's behavior models from laboratory soil bin data. Artificial neural network (ANN)

models were developed. Shallow ANNs were fast, accurate, and reliable tools to predict AGV behavior in a controlled laboratory setup (i.e., sloped soil bin). The predictive AGV's behavior model from a control laboratory setup proved to be an excellent starting point for optimizing the vehicle control parameters. However, these models cannot be extended to predict the AGV's behavior in a continuously varying slope environment. Therefore, Chapter 4 aimed to develop machine learning-based models on data collected from a real-field environment. Machine learning and deep learning-based models were developed and analyzed. The study found that the deep neural networks (DNN) model was well-suited for predicting the AGV's behavior in a sloped, real-field environment. Chapters 3 and 4 explored the capabilities of an artificial intelligence methods to simulate the AGV's behavior on sloping terrain. The developed models predicted the AGV's specific dynamic response, including traction, slip, and energy from the inputs of AGV's velocity, applied load, and slope.

A small and lightweight AGV was unable to provide the downforce and drawbar required for a traditional seeder. Hence, these AGVs would need a specialized robotic grain drill. The feed mechanism is the heart of the grain drill, and its design and performance influence the plant population and crop yield. Therefore, Chapter 5 aimed to design and develop a screw auger type feed mechanism. The feed mechanism was developed and tested in a laboratory setup against speed, vibration, and slope as control variables. The study delivered a bulk feed mechanism for wheat drilling, which can be easily scaled and adopted by small autonomous vehicles or mobile robots.

The dissertation laid the foundation for robotic farming on the sloped terrain, and the envisioned multi-AGV fleet may provide a valid solution to farm the arable uneven, highly sloped terrain. The findings provide a groundwork for robotics and automation, which has the potential to solve the emerging problems in the food production system by producing food, fuel, and fiber for the growing population.

Table of Contents

List of Figures

List of Tables

Acknowledgments

I want to express my deepest gratitude to my major professor, Dr. **Dan Flippo** for providing me the opportunity to pursue my doctoral degree. His time, guidance, support, and mentorship allowed me to accomplish this monumental undertaking. Likewise, great appreciation is extended to the members of my supervisory committee; Dr. **Steve Welch**, Dr. **Ajay Sharda**, and Dr. **Naiqian Zhang**, for their time and valuable suggestions in my research and other scholarly endeavors. Also, I would like to thank Dr. **Sanjoy Das** and Dr. **Edwin Brokesh** for their guidance and mentorship in my research projects. Additionally, I am thankful to the National Institute of Food and Agricultural (NIFA-USDA) for research funding.

I am also grateful to **Hasib** and **Harman** for their assistance and feedback during my stay at K-State. Likewise, to the 2050 Research Lab members: Lillian Schmitz, Jason Scheer, Owen Li, Calvin, Igor Sheshukov, and Ben Weinhold. Fellow graduate students: Prashanta, Manoj, Ketan, Mingqiang, Rahul Singh, Rahul Harsha, and Lucas; K-State friends: Anish, Nitin, Rupinder, Akash, and Gauresh, thank you all for the friendship which made graduate school a lot more meaningful and enjoyable experience. Additionally, I extend my heartfelt thanks to my fiancée **Swetha** and my family for their unwavering love, understanding, and continuing support in completing this research work.

Profound thanks to Dr. Joseph Harner, Dr. Naiqian Zhang, Arlene Jacobson, Eli Shepperd, Jamie Boeckman, and other faculty and staff members in the Department of Biological and Agricultural Engineering for all their unwavering support.

Dedication

I dedicate this work to

my parents, Shobhabai and Manik Badgujar,

sister Dhanashri,

my extended family Babybai and Rajendra Badgujar,

fiancée Swetha.

Chapter 1

Introduction

The global population is projected to grow from 8 billion in 2022 to a projected 9.7 billion by 2050[1], so meeting the growing population's demands (e.g., food, fiber, and fuel) is a pressing issue. Population dynamics necessitate an increase in global agricultural production by 70% from the current level to accomplish the 2050 food security goals[2]. Presently, the annual percentage crop yield increase is only half of the required yield increase needed to meet projected food needs. Moreover, climate change, water scarcity, land degradation, cropland losses, species infestations, diet shifting, and other challenges may (all together) cause projected yields to be 5-25% short of the 2050 demand[3–6]. One counterstrategy under development is to advance the crop gain rate by combining a genomic information and technology with an automated collection of information on plant traits (i.e., high throughput phenotyping). Another approach is improving the crop resource use efficiencies via precision agricultural technology, which exploits the sensors and automated data acquisition systems.

A third strategy is the sustainable cropland expansion. Around 97% of our food sources come from arable land[7]. Still, arable land expansion remains a critical factor in food production growth to meet the demands of a growing population. Deforestation and inappropriate agricultural practices had degraded about 2 billion ha of the world's agricultural land[8]. In addition, satellite measurements showed an absolute decline in productive land across 12% of the global land between 1981-2003[9]. Moreover, escalating non-food crops (e.g., fiber and fuel crops) demand raises concerns about having sufficient food crop production area[10;11]. For example, the global fuel market required around 1% of biofuel for transport in 2005; however, by 2050, biofuels are projected to increase up to 25% of the global fuel market[4].

Therefore, the arable land expansion will remain an important factor in crop production growth in many countries, including the United States[12]. It is projected that an additional minimum of 100 million ha of agricultural land is required by 2050[13] to assist the 2050's food security goals.

In summary, population pressure, lack of prime or good-quality land options[14], higher farm exports market prices[15] and growing demands for non-food crops are creating incentives and an imperative need to bring marginal land under production[16–18]. Marginal land is defined as land currently unfit for production for several reasons, including limited water supply, poor soil quality, pollution from prior use, and lack of transportation network[19;20]. Other characteristics of marginal land are its excessive steepness (slopes $\geq 6^0$), hills, and uneven terrain. We believe there is substantial potential to increase needed food production on this marginal, highly sloped land in the Great Plains.

The Great Plains is a major physiographic region in North America, occupying approximately 33% of the United States. These plains are arable land for croplands, hay pastures, and grazing[21]. However, the majority of the Great Plains region is characterized by gently rolling hills, a broad expanse of prairie with little or moderate elevation change, steppe, and grassland, which are often categorized as marginal land. The marginal arable land is usually left for cattle grazing but could be farmed for food grain production in the near future. Firstly, it is essential to determine the available marginal land in the Great Plains region. Therefore, we used three different datasets to quantify the amount of the marginal land currently under shrubs or herbs, unprotected, and 6^0 to 25^0 steep slopes on the Great Plains. This dataset was as follows: (1) the 2011 National Land Cover Database (NLCD), (2) the most recent Protected Areas Dataset (PADUS), and (3) the 10-m resolution National Elevation Dataset (NED). Within the twelve Great Plains states, we estimated that a total of 116,000 km^2 area is categorized as marginal, highly sloped land, as shown in Figure 1.1, which compared the area in the Great Plains to a total of about 200,000 km^2 of wheat planted nationwide. Apart from North America, Shaxson (1999) estimated that the steep land (i.e., slopes >12%) constituted around 35% of the total land area in both wet and dry tropical zones (which occurred between 5° and 20° latitude). Further, Shaxson (1999) estimated that in Asian regions, around 39% of the total land area falls under 8 -30% slope[22;23].

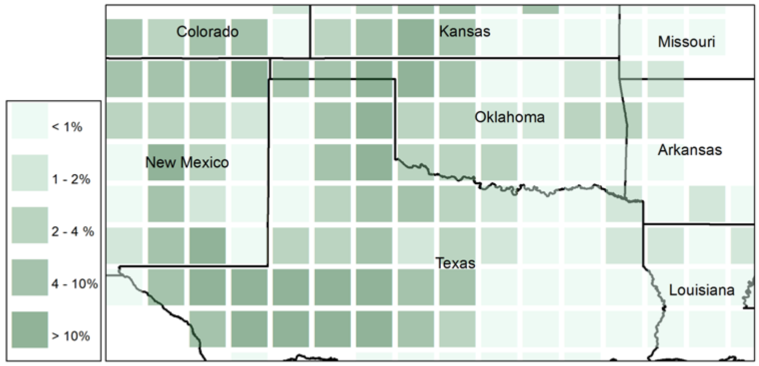

Figure 1.1: *The percentage of available and potentially profitable land (per 1×1 degree tile) in selected states, which was too steep for current farming technology*

The estimated marginal sloped land in the Great Plains region and other parts of the world, constituted a significant proportion of arable land. A sustainable expansion of wheat production to these steep grasslands and uneven terrain would almost double the land area used for this crop from 4% of the Great Plains region to 7%. However, it is unsafe to cultivate arable land with slope steeper than 6° with large conventional farm machinery or implements. On sloping terrain, the agricultural vehicles (e.g., tractors) and other off-road vehicles carry a very high risk of roll-overs. In the United States, approximately 120 farmer casualties were reported per year in accidents related to tractor roll-overs while operating on steep slopes[24]. This risk is one of the reasons why hills or uneven terrain are not farmed, and are currently left for cattle grazing in the United States, mainly in the Great Plains.

The technological barrier to slope farming could be potentially solved by exploiting an advanced robotic system or small automated vehicles. Today's mobile robots or ground vehicles are well-positioned to tackle the numerous complex problems in agriculture, ranging from seeding to harvesting[25–31]. Multiple small ground vehicles, working with coordination and optimized mission planning can finish work comparable to large machine with improved safety[32] and reduced soil compaction[33]. Unlike heavy machines, Autonomous Ground Vehicles (AGVs) can operate on relatively wet soil without causing damage, and even when one AGV becomes inoperative, the others could finish the operation. Moreover, a relatively small AGV (< 1m) is best suited for crop scouting and target-specific input application; those are essential components of precision agriculture technology[34]. A small vehicle fleet has the potential to increase food production, lower production costs, and replace labor shortages[26;35].

Therefore, we proposed a fleet of Autonomous Ground Vehicles (AGVs) to farm the marginal, highly sloped land. The fleet would perform a primary agricultural operation on marginal, sloped terrain, aiming toward an arable land expansion to boost the food grain production in the region. In this study, we plan to use a multiple AGVs to farm ground with slopes of up to 20°. However, the successful operation of the proposed AGV fleet on sloping terrain was dependent on multiple components focusing on:

1. Vehicle characteristics: traction, mobility, and energy consumption.

2. An AGV's predictive behavior models on slope.

3. Design and development of a robotic seeder prototype

Therefore, the study consisted a specific components aiming to build a fleet of AGVs to perform the primary agricultural operation on marginal, sloped land. The components and associated chapters were explained and illustrated with the help of Figure 1.2.

1.1 AGV's characteristics

Firstly, it was imperative to understand an individual AGV's traction, mobility, and energy consumption characteristics on varying slopes, speeds, and drawbar, in a controlled laboratory environment. This would lay a foundation for an AGV fleet operating on marginal, sloped land by determining the single AGV's suitability, capabilities, and by quantifying the physical limits. The data obtained from this study would be used for building a mobility model for the AGV's.

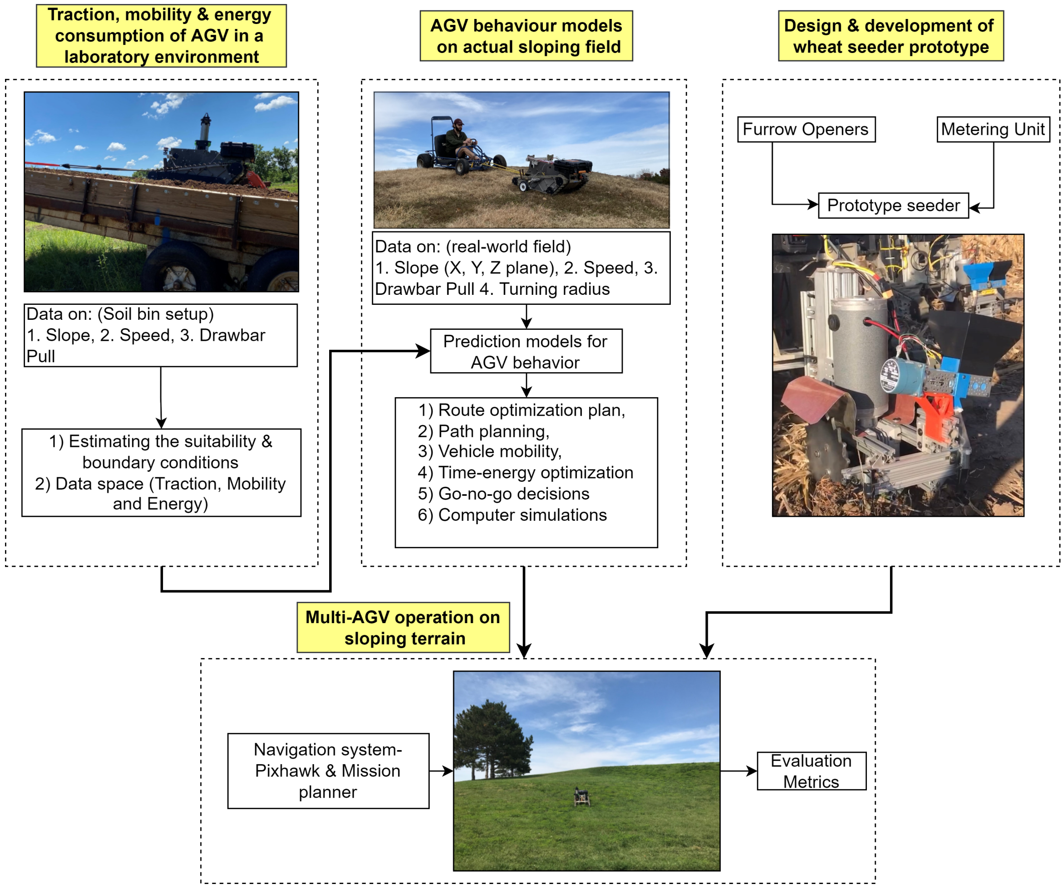

Figure 1.2: *Components of the AGV fleet operating on marginal, highly sloped land*

1.1.1 Experimental investigation on traction, mobility, and energy usage of tracked AGV on a sloped soil bin (Chapter 2)

The Chapter 2 introduced to (1) the prototype AGV and soil bin setup, (2) the instrumentation setup, experimental setup, and testing procedure of off-road vehicle on a controlled sloped environment, and (3) the application of the generated database, obtained results, and significant findings. The data generated from this study would also be used for developing the traction, mobility, and energy consumption models on sloped soil bin.

1.2 AGV's predictive behavior models

The fleet needed an optimized path planning and efficient control algorithm since the cost of going uphill versus going downhill would not be the same on continuously varying terrain. Therefore, the AGV's predictive behavior models were essential for solving the multiple objectives ranging from optimizing the AGV control variables, traction, mobility, energy, time, efficiency, safe operation, and negative soil impacts.

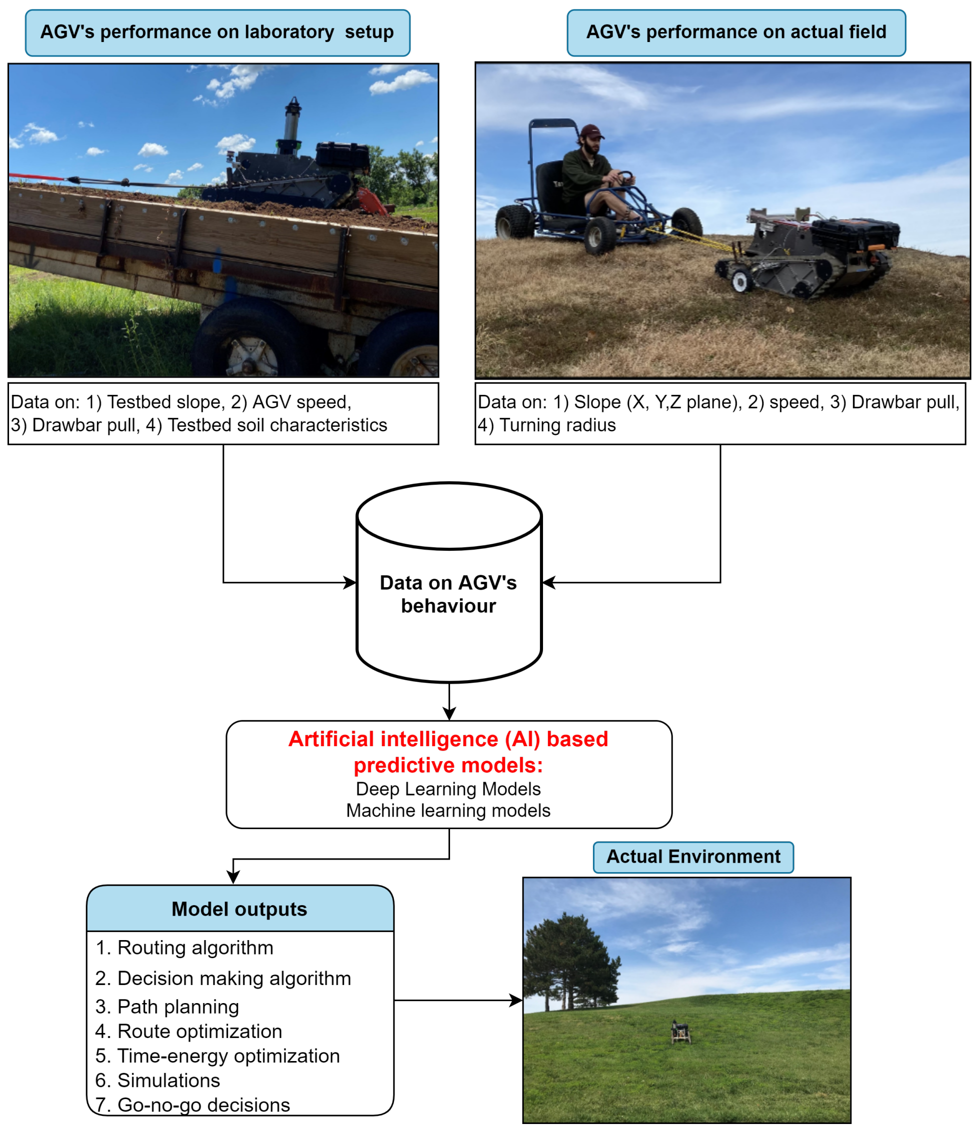

Figure 1.3: *AGV's predictive behavior models in a sloping environment*

1.2.1 Artificial neural network to predict traction performance of the AGV on a sloped soil bin and uncertainty analysis (Chapter 3)

We explored the ability of a deep learning-based model to predict the traction performance of a single AGV, from the data obtained in a controlled laboratory setup. This chapter discussed (1) the limitations of traditional modeling methods, (2) the development of neural network models to predict the AGV traction performance on a sloped soil bin as a function of slope, speed, and drawbar pull, and (3) the investigation the output uncertainty of the developed neural network models with a Monte-Carlo simulation-based method. The resulting traction prediction model would assist in improving the AGV's performance by optimizing the operational variables. Moreover, it would help in vehicle design, safety, and in optimizing the energy and mobility of the AGV on highly sloped and uneven terrain.

1.2.2 Deep neural networks to predict AGV's behavior on sloping terrain field (Chapter 4)

The model built in a control laboratory setup (Chapter 3) was an excellent starting point for optimizing the vehicle control parameters. However, these models were unable to extend for predicting the AGV's behavior in an actual continuously varying slope environment. Therefore, building a deep learning-based models on the data obtained from the real-field environment, including the continually varying terrain, was essential. The chapter discussed (1) the instrumentation setup and testing procedure for the field testing of the AGV, (2) the data collection methods (3) the development of various machine learning-based traction, mobility, and energy consumption models for the AGV from the experimental data. These models would predict the specific dynamic response, including traction, slip, and energy from the inputs of vehicle velocity, applied load, and slope.

1.3 Design and development of robotic grain drill

The proposed fleet operating on marginal, highly sloped terrain necessitated that a multiple equipment's or implements perform a basic agricultural operation, ranging from tillage to harvesting. Initially, the grain drill was targeted because it provided a proof that slope farming was feasible with these small vehicles. Additionally, the grain drill enabled the creation of a testbed for other prototype equipment to be used in later stages of the production cycle. The robotic grain drill would open the furrow and disperse the seeds into the furrow at a pre-determined rate while operating on varying sloped terrain. The feed mechanism unit and furrow openers were crucial components of the seeder, and their design and performance influence the plant population and crop yield.

1.3.1 Design, fabrication, and experimental investigation of screw auger type feed mechanism for a robotic wheat drill (Chapter 5)

The feed mechanism is the heart of the grain drill, and its constructional design and operation parameters determined the seed rate. The chapter discussed (1) the design and fabrication of a screw auger type feed unit for a robotic wheat seed drill and (2) the experimental investigation of the developed feed mechanism at varying speed, vibration, and slope inclination. The developed feed mechanism would be incorporated into the prototype robotic grain drill. The study aimed to deliver a bulk feed mechanism for wheat drilling, which could be easily scaled and adopted by small autonomous vehicles or mobile robots.

1.4 Summary and conclusions (Chapter 6).

The dissertation's significant findings and conclusions were reported, and future research goals or suggestions were briefly discussed.

Chapter 2

Experimental investigation on traction, mobility and energy usage of a tracked autonomous ground vehicle on a sloped soil bin[1]

2.1 Abstract

Excessive steepness of grasslands, hills, or uneven terrain present difficulties for farming with large conventional equipment. Therefore, a fleet of Autonomous Ground Vehicles (AGVs) was proposed to perform primary agricultural operations on high sloped hills or terrain. However, it was imperative to understand how an individual AGV functions on sloping terrain under varying load and speed. Hence, this study aimed to investigate the traction, mobility, and energy consumption characteristics of AGVs on a sloped soil bin environment. A drawbar pull performance of the prototype AGV was evaluated on a level terrain and variable slope of 10° and 18°, both uphill and downhill, at varying drawbar pull (P) and AGV speed. The AGV's performance metrics included power efficiency (PE), travel reduction (TR), and power number (PN) which related to the AGV's traction, mobility, and energy usage, respectively. The AGV generated a drawbar pull equivalent to its weight only on a downhill run for reduced PE. On a level terrain (0°), the peak PE was 0.20 and was found

[1]Results were published as a peer-review article. Badgujar, C., Flippo, D., Brokesh, E., & Welch, S. (2022). Experimental Investigation on Traction, Mobility & Energy usage of the Tracked Autonomous Ground Vehicle on a Sloped Soil Bin. *Journal of the ASABE*, 10.13031/ja.14860.

to be 108.3% and 328.6% higher on 10° and 18° downhill run than uphill with a 55.5% and 133% increase in drawbar pull, respectively. Both applied drawbar pull and uphill operations caused the AGV's TR. The TR, corresponding to a peak PE, increased from 10% to 30%, respectively, on 0° and both 10° and 18° uphill. The optimum values of power number ranged from 2 to 4. The AGV delivered the optimum PE and generated enough drawbar pull with an optimum TR to perform a range of agricultural operations on a slope up to 18°. The study explored the suitability and established the boundary conditions of small size ground vehicles for high-sloped farming. Besides this, the study also aimed to generate an AGV's slope traction database to optimize its control variables, design optimization, and develop a mobility model for sloped terrain.

2.2 Introduction

Approximately 97% of our food comes from arable land[7], but arable land expansion remains a critical factor in food production growth to feed continuously burgeoning population. An additional minimum of 100 million ha of agricultural land use is needed by 2050 to meet the growing food demands[13]. However, deforestation and inappropriate agricultural practices had already degraded around 2 billion ha of the world's agricultural land[8]. Satellite data showed a decline in 12% of the global agricultural land from 1981 to 2003[3]. Moreover, escalating non-food crops demands raise concerns for having sufficient food crop production area[10;11]. For example, in 2005, only 1% of biofuel was utilized for transport in the global fuel market; however, by 2050, biofuels are projected to increase up to 25% of the global fuel market[4]. In summary, population pressure, diminishing prime or good-quality land options[14], higher farm export market prices[15], and a growing demand of non-food crop production area may create incentives to bring marginal land, currently unfit for agriculture, into production[16;18;19]. Marginal land, including excessive steepness of grasslands, hills, and uneven terrain (slope $> 6°$), is unsafe for large conventional farm equipment. Tractor roll-overs are more frequent during farm operations on steep slopes and are one of the leading causes of farmer injury or death[24;36;37]. Therefore, these steep grasslands are typically not suitable for agricultural vehicles[38], and are usually left for grazing, particularly in the Great Plains, USA[21], which are characterized by gently rolling hills, steppe, and grasslands[39]. The 2011 National Land Cover Database suggested that, within the twelve Great Plains states, an estimated 11.6 million ha of plains and grasslands are under shrubs or herbs, unprotected, and at a $6°$ to $25°$ slope[40]. There is a substantial potential to profitably increase food production on these steep grasslands and uneven terrains.

Therefore, a fleet of small autonomous ground vehicles (AGVs) is envisioned to perform basic agricultural operations on steep slopes, hills, and uneven terrain. Multi-AGV is a fast-growing trend on smart farms[41;42] and is considered a prime candidate for future outdoor farms[42–44]. An AGV fleet accomplishes the work equivalent to a large machine with reduced soil compaction, while supporting mission coordination and reconfiguration with improved safety[45–47]. The AGV can be programmed to perform repetitive tasks or operations with peak efficiencies. However, it is imperative to understand how an individual AGV functions on sloping terrain under varying load and speed conditions, especially regarding traction, mobility, and power required. Moreover, the vehicle's physical limits must be established before planning a large-scale AGV operation on sloped terrain.

Off-road vehicle performance varies with vehicle type, configuration, and intended function[48–50]. The drawbar pull test has emerged as a valuable tool to characterize off-road vehicle performance, e.g., tractors, cross-country, and space exploration vehicles[50]. During a drawbar pull test, a vehicle must generate sufficient gross traction to counteract motion resistance and the applied drawbar pull. On soft soil or uphill run, an increase in drawbar pull force results in both increased wheel or track slip and energy loss. The vehicle can be immobilized, with sufficient drawbar pull which may restrict the AGV operation on high slope terrain. The drawbar pull test measures the vehicle's total tractive ability, mobility, and energy consumption on specified soil conditions[49;51]. Three popular methods reported in the literature for drawbar pull testing of robots or ground vehicles were as follows: (1) testing a single traction element (e.g., track or wheel) in a soil bin[52–55], (2) testing the entire vehicle in a soil bin[56–58] and (3) testing a vehicle in actual application environments[59;60]. However, testing a single traction element typically does not represent the entire vehicle or system performance. Contrastingly, the actual application environment lacks test repeatability due to field variation which may introduce error. Moreover, operating a heavy ground vehicle on actual sloping terrain may be hazardous to both vehicle and operator during testing. Hence, testing the entire AGV in a controlled soil bin environment seems appropriate.

In the last several decades, the drawbar pull performance of human-operated tractors, ground vehicles and robots has been extensively studied to optimize operational parameters and control variables, either on unprepared fields or in controlled soil bin environments[61–64]. Soil conditions significantly influenced the drawbar pull performance of off-road vehicles. Soil bin facilities have emerged as model laboratories for traction experiments for off-road vehicles[65]. Soil bin facilities helped to evaluate the soil-machine interaction, traction element design and performance, in addition to optimizing tractive efficiency for various off-road vehicles under varying soil conditions. In most soil bin studies, the influence of soil properties (i.e., moisture content, bulk density, soil type, soil strength) on traction elements or vehicle performance were extensively studied[65–69]. A soil bin capable of slopes from 0 to 11° was developed by Liu et al. (2002)[70]. Otherwise, no literature is available on varying the soil bin slope and its influence on vehicle performance.

In this study, a prime function of a prototype AGV was to traverse on level terrain and steep slopes (up to 20°) with an adequate drawbar pull and load-carrying capacity to perform basic agricultural operations. Therefore, a drawbar pull test was performed on a prototype AGV to investigate the traction, mobility, and energy usage characteristics on level terrain and uphill and downhill travel on a variable slope ranging up to 20° at varying operating drawbar pull and speed. The drawbar pull performance test would quantify the AGV's available reserve power and help establish its performance curves[71]. For a track vehicle, the test would measure the net traction developed by each track, while ascending and descending slopes, with or without additional applied drawbar pull. The magnitude of an additional drawbar pull would determine the nature of the agricultural operation (e.g., tillage type, seeding, spraying, harvesting, etc.) the AGV could perform on sloping terrain. The experimental investigation would be fundamental to understanding the limitations and capabilities of the AGV in a sloping environment. The study would also explore the suitability and establish the boundary conditions of small size ground vehicles for high slope farming. Another goal is to generate an AGV's traction database, which could be utilized to develop vehicle mobility models for highly sloped terrain. These models could predict specific dynamic responses, including power efficiency, travel reduction, energy consumption rates from inputs on a slope, applied drawbar pull, and vehicle speed. Mobility models could be used to optimize prototype design, components in path planning, and control algorithms that optimize multiple objectives including energy and time efficiency. The traction database is an important first step towards developing the AGV's mobility models.

2.3 Materials and methods

2.3.1 Experimental setup

Autonomous Ground Vehicle (AGV)

A continuous track-type AGV prototype, shown in Figure 2.1, was used in this study. This skid-steer AGV was developed at the 2050 Robotics Laboratory (Kansas State University, Manhattan, KS, USA) to perform an agricultural operation on steep slopes and uneven terrain. The technical details of the AGV and traction element (tracks) were given in Table 2.1. A positive drive sprocket drove each of the two rubber belts, which had teeth molded into their inner surfaces. The AGV was compact, so its overall width was less than a typical crop row spacing of 0.76 m, and it was lightweight (102 kg). Additionally, it was equipped with an on-board microcontroller, a reconfigurable input-output device (myRIO, National Instruments, Austin, TX, USA) that required a system-design platform in LabVIEW, proprioceptive sensors such as amperage (Analog 20 A Gravity series, dfrobot, Shanghai, China), voltage (30 VDC, Phidgets Inc., Calgary, Canada), and a track encoder (Encoder products, Sagle, Idaho, USA). The AGV was powered by a rechargeable 22.2 V, 13 Ah, and 15 C Lithium Polymer (Li-Po) battery (Venom Power, Rathdrum, Idaho, USA). The AGV accommodated the two battery packs and each battery pack included two batteries connected in a parallel configuration which resulted in 26 Ah capacity. The prototype accommodated two separate battery packs with a total amp-hour capacity of 52 Ah and 22.2 V, which was sufficient for at least 4 -6 hours of continuous operation at standard operating conditions where the AGV operated on a concrete road without drawbar loading. The AGV was tele-operated and connected wirelessly via remote device software to a tablet computer (iPad, Apple Inc, Cupertino, CA).

Table 2.1: *Technical details of the AGV and fitted track*

AGV		Track	
Mass, kg	102	Track style	Continuous
Length, mm	1160	Thickness, mm	5
Width, mm	640	Belt width, mm	50
Height, mm	550	Belt contact length, mm	2410
Gauge, mm	500	Diameter of sprockets and idler, mm	126
Longitudinal CG location from front axis, mm	400	Sprocket to idler center distance, mm	910
Longitudinal CG location from rear axis, mm	700	Lug height, mm	12
Vertical CG location, mm	200	Pitch, mm	55
Hitch height, mm	200		

Soil bin

An off-road vehicle's tractive ability was derived from the soil through its traction elements[49;72]. The DP performance of a vehicle varied greatly by soil[73] and soil conditions, i.e, soil moisture[74], bulk density and cone index[75]. A soil bin ($5.0m \times 2.5m \times 0.2m$), fitted with a hydraulic lift attachment was used in the study because it provided an adjustable tilt bed (0°- 20°) for vehicle testing in both horizontal straight runs and sloped runs, including uphill and downhill. The soil bin was filled with silt loam, and soil characteristic was evaluated for soil bulk density on a dry basis (g/cm^3), water content (%), cone index (kPa) and cone index gradient (kPa/mm).

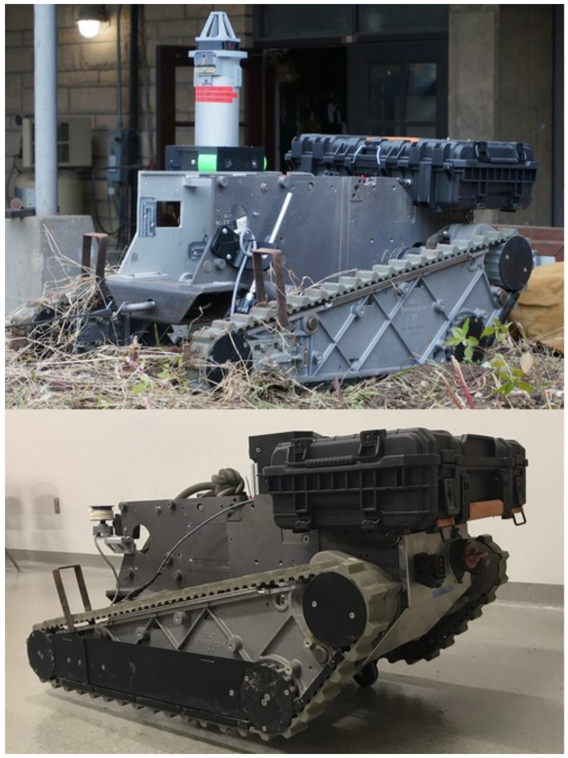

Figure 2.1: *AGV used in the study*

Instrumentation setup

An instrumentation setup was established to measure the AGV's energy consumption, travel reduction, applied drawbar pull, and soil bin testbed characteristics. The AGV was equipped with amperage-voltage sensors and track encoders to measure its energy consumption and theoretical velocity, respectively. An S-type load cell (HT Sensor Technology Co., Ltd, Xi'an, China), with a capacity of 200 kg and $\pm 0.02\%$ accuracy, was calibrated and used to measure the applied drawbar pull. The track encoder data were used to compute the velocity of the AGV track peripheries relative to the chassis i.e., theoretical velocity. A towed fifth wheel, equipped with a shaft encoder (Encoder products, Sagle, Idaho, USA) was attached to the AGV chassis to measure vehicle travel velocity. However, the fifth wheel slipped on the testbed soil surface so, this initial fifth wheel was not successful and was replaced with a 3D-printed spool with a cotton thread wrapped around its circumference. During the experiments, the thread was tied to the soil bin frame. The thread wrapped and unwrapped along the spool circumference with respect to the AGV's position, and the encoder data were recorded. The spool-thread arrangement, hereafter referred to as Ground Truth Encoder, measured the AGV's travel velocity. The myRio microcontroller was accountable for the AGV operation, data collection, and storage (via USB thumb-drive), and was connected to an iPad (tablet computer) via Wi-Fi.

The cone penetrometer test (CPT) is a test for in situ measurement of soil penetration resistance, which is an indicator of soil firmness[76;77]. A digital recording cone penetrometer (Rimik model: CP40II, Rimik Pvt. Ltd., Toowoomba, Australia) with a cone apex angle of 30° and base area of 323 mm^2 (ASABE Standards, 2019[78]) was used to measure cone index (kPa) and cone index (CI) gradient (kPa/mm). In addition, a soil bulk density on a dry basis (d.b.) was measured with a bulk density soil sampling kit (AMS Inc., American Falls, Idaho) using cylindrical soil cores with a 49 mm diameter and a 100 mm height. Gravimetric water content was determined using a standard oven-dry method, with soil samples dried at 105°C for 24 h. A digital protractor (Mini-MAG, Fowler High Precision, Newton, MA, USA) was used to set the desired testbed slope.

Figure 2.2: *Drawbar pull test experimental setup: (a) conceptual drawing, (b) AGV operating on sloped soil bin. Direction of forward travel is from left to right*

Drawbar loading device

A rubber resistance band was used to apply drawbar pull to the AGV. The drawbar pull increased as the stretching length of the rubber band increased; the magnitude of the drawbar pull was not controlled with any control system. One end of the resistance band was attached to the soil bin frame and the other to the load cell, which was hooked to the AGV's hitch point, keeping the line of pull parallel to the soil bin terrain (Figure 2.2). A load cell measured the applied drawbar pull. In this study, a ramped-drawbar pull test technique[50;57] was implemented. Therefore, a complete range of drawbar pull from zero (AGV self-propelled condition) to the maximum drawbar pull (100% slip) could be observed in a single run. The experimental setup for conducting the drawbar pull test was shown in Figure 2.2.

2.3.2 Experiment design

Preparation of soil bin

We strived to minimize variabilities in soil physical properties throughout the experiment. A soil preparation method consisting of soil loosening, pulverization, and leveling, was employed on each slope as mentioned in[50;57]. However, repeated vehicle passes were compacting the soil, cumulatively increasing the soil bulk density. A 15 tine bow rake (Model: 63141, Razor-Back professional tools, Orlando, FL, USA) was used for soil preparation. This steel rake was perfect for loosening or breaking up compacted soil and leveling the area. The trafficked soil was loosened and leveled with the rake.

The ramped- drawbar pull test was conducted on level terrain 0°(S_0) and sloping 10° and 18° terrain, both uphill (S_{10U} and S_{18U}) and downhill (S_{10D} and S_{18D}). The range of the AGV's actual velocity was 1 to 5 m/min (Table 2.2). During the experiment, the soil bin slope was first fixed, and the AGV was operated at each speed. Each experiment was replicated three times. The independent variables and response variables were shown in Table 2.2. During each of the three replicates, the AGV was operated on untrafficked soil. The soil bin was 2.5 m wide, and the single-track width was 50 mm, enabled multiple runs of the AGV on untrafficked soil. The performance of the AGV was assessed in terms of metrics that relate to traction analysis, vehicle mobility-immobility, and energy consumption.

Table 2.2: *Variables used in the experiment*

Predictor			Response
Slope, °	Speed, (m/min)	Drawbar pull, N	
0 (S_0) 10 Uphill (S_{10U}) & Downhill (S_{10D}) 18 Uphill (S_{18U}) & Downhill (S_{18D})	1.0 2.0 3.0 4.0 5.0	Variable Pull, 0-1500 N	Power efficiency, η Travel Reduction, s Power Number, PN Energy Consumption Rate, ECR

Vehicle traction ratio is the ratio of the drawbar pull (P) to the AGV's load normal to the tractive surface (W). The AGV's weight included the vehicle weight and the weight of removable batteries. Traction ratio (P/W), allowed a dissimilar vehicle weight comparison[49;50]. Travel reduction (s) indicated the reduction in the AGV's forward progress caused by shear within the soil, slip between the track and terrain, and flexing of the track[49;50], and was defined as:

$$s = 1 - \frac{V}{V_{\mathrm{t}}} \tag{2.1}$$

where V was the AGV's actual velocity derived from the ground truth encoder. The theoretical velocity (V_t) was the product of track sprocket angular velocity and track rolling radius at the sprocket. The track angular velocity was derived from track encoder data. Power loss during the conversion process prevented the AGV from converting all electrical power into practical work. Therefore, a power efficiency, η, indicated the efficiency of an AGV in transferring the electrical power to an available drawbar power and was defined as:

$$\eta = \frac{P \times V}{P_{\mathrm{B}}} \tag{2.2}$$

where P_B was the power delivered by the battery and P was the drawbar pull. We use "power efficiency" and not "tractive efficiency" because ASABE Standards (2013)[79] defined tractive efficiency as the ratio of output power to input power for a traction device. The input power for the track was the axle power, which was the product of input torque applied to the track sprocket and the sprocket angular velocity. The input power, we measured was the electrical power delivered by the battery, which was not axle power. As a result, some power was lost because the efficiency of the motor and its circuitry in converting electrical power to motor output shaft power, was less than 100%.

The drawbar pull and vehicle velocity may influence the vehicle's power efficiency. The optimized power efficiency significantly improved the AGV's field performance[80]. There is an optimum range of drawbar pull or velocity that maximizes the PE. Hence, it was important to optimize power efficiency by selecting the proper values of drawbar pull and velocity. A velocity loss or drawbar pull loss results in tractive inefficiency[81].

Battery capacity restricts the AGV's continuous operation, which would influence the mission planning and impact the overall efficiency of the AGV system. Additionally, the AGV's speed, and, drawbar pull, coupled with the slope may influence energy consumption. Therefore, it was important to establish the AGV's power-energy consumption characteristic curves on level and sloped terrain to optimize energy efficiency. Power Number (PN), defined as the ratio of power used to the product of the AGV's weight and velocity (eq. 4.3), quantified mobility power cost. It estimated the power required to travel with an external load on a specific terrain, and was thus valuable for mission planning[50].

$$PN = \frac{P_{\mathrm{B}}}{W \times V} \tag{2.3}$$

An energy consumption rate (ECR) was a distance-specific energy consumption expressed in Wh/km for electric vehicles derived from the PN. The ECR calculated the energy required (Wh) to travel one km distance[82;83] and was defined with equation 2.4. ECR measured the relative efficiency of the AGV while operating under different conditions (i.e., slope climbing or level terrain)[84].

$$ECR = \frac{PN \times W}{3.6} \tag{2.4}$$

2.3.3 Experimental conditions

Drawbar pull test procedure

Initially, the testbed slope was fixed, and the AGV was teleoperated at the desired speed (Table 2.2). As the AGV moved on a testbed, the resistance band ramped up the P from zero to the maximum P until the AGV immobilized (i.e. 100% slip condition). This ramped-drawbar pull test technique permited a full P versus power efficiency (η) curve, P versus travel reduction, and P versus power number to be completed in a single run. Each experiment was replicated three times before proceeding to the next (Table 2.2).

Data collection and analysis

Before conducting the drawbar pull test, the testbed condition was measured, and the mean values were reported (Table 2.3). The soil cone index (CI) was recorded for the 0-150 mm depth range at eight randomly selected locations on the testbed as per the ASAE standards[78]. The CI gradient (kPa/mm) was computed from available data, which described the soil's penetration resistance per unit depth[50]. Six soil cores for bulk density and water content were taken randomly on the testbed. During the drawbar pull test, data from the load cell, each track encoder, the ground-truth encoder, and the amperage-voltage sensors were recorded by a microcontroller (myRio) device at a frequency of 10 Hz. The response variables, power efficiency, and power number were calculated from the recorded sensor data (i.e., load cell and amperage-voltage sensors). The travel reduction was determined by comparing the theoretical velocity (V_t) to the actual velocity (V) (eq. 4.2). A multiple comparison procedure (Least significant difference, LSD) was used to analyze the testbed soil characteristics to ascertain if a significant difference existed among the soil properties CI, bulk density, and water content on the S_0, S_{10} and S_{18} terrain. The testbed slope with its S_0, S_{10} and S_{18} terrain conditions did not significantly affect CI, CI gradient, or water content. Testbed slope did significantly affect soil bulk density (P=0.02). A MATLAB program (Software version - R2018a, MathWorks, Natick, MA, USA) was used to generate a contour plot of dependent variables including power efficiency, travel reduction, and power number as a function of P/W and the AGV's speed.

Table 2.3: *Testbed soil conditions and properties**

Testbed slope	Cone Index (kPa) [a]	CI gradient (kPa/mm)	Water content (% db)	Bulk density (g/cm^3)
0 (S_0)	493.3 ± 92.3[a]	2.5 ± 0.5 [a]	17.2 ± 4.0 [a]	1.5 ± 0.1[a], [b]
10 (S_{10})	464.4 ± 97.6 [a]	2.4 ± 0.5 [a]	18.8 ± 5.7 [a]	1.4± 0.1 [a]
18(S_{18})	461.5 ± 59.8 [a]	2.4 ± 0.3[a]	18.5 ± 1.8 [a]	1.6 ± 0.04 [b]
P-value	0.59	0.73	0.77	0.02

[a] Within each column, mean values with the same letter are not significantly different at P=0.05 (LSD test).
* Soil properties are recorded for the 0-150 mm depth range.

2.4 Results and discussion

2.4.1 Traction performance

The traction performance of the AGV on both level terrain (S_0) and sloping (S_{10} and S_{18}) terrain was expressed in terms of power efficiency and travel reduction as a function of P/W and the AGV's speed, shown in Figures 2.3 and 2.4, respectively. A general shape of the PE performance curve showed that PE increased as P/W increased, reaching the peak and maintaining it for a small range of P/W, as illustrated in Figure 2.3. After reaching the peak, PE started to decline with further increase in P/W while the travel reduction rapidly increased after hitting the maximum P/W value, eventually immobilizing the AGV when track slip reached 100% (Figure 2.4). The PE contour plot depicted an efficient zone of operation, indicating that the maximum desirable driving condition was at the P/W and speed setting, where travel reduction was at a minimum and PE was at the peak. The efficient zone of the AGV operation, on a level terrain (S_0), was observed at ≥3 m/min speed and 0.50-0.60 P/W range, where PE was 0.20, and travel reduction was 0.10 (Figure 2.3 and Table 2.4).

The AGV was capable of generating drawbar pull equal to its weight, with a traction ratio

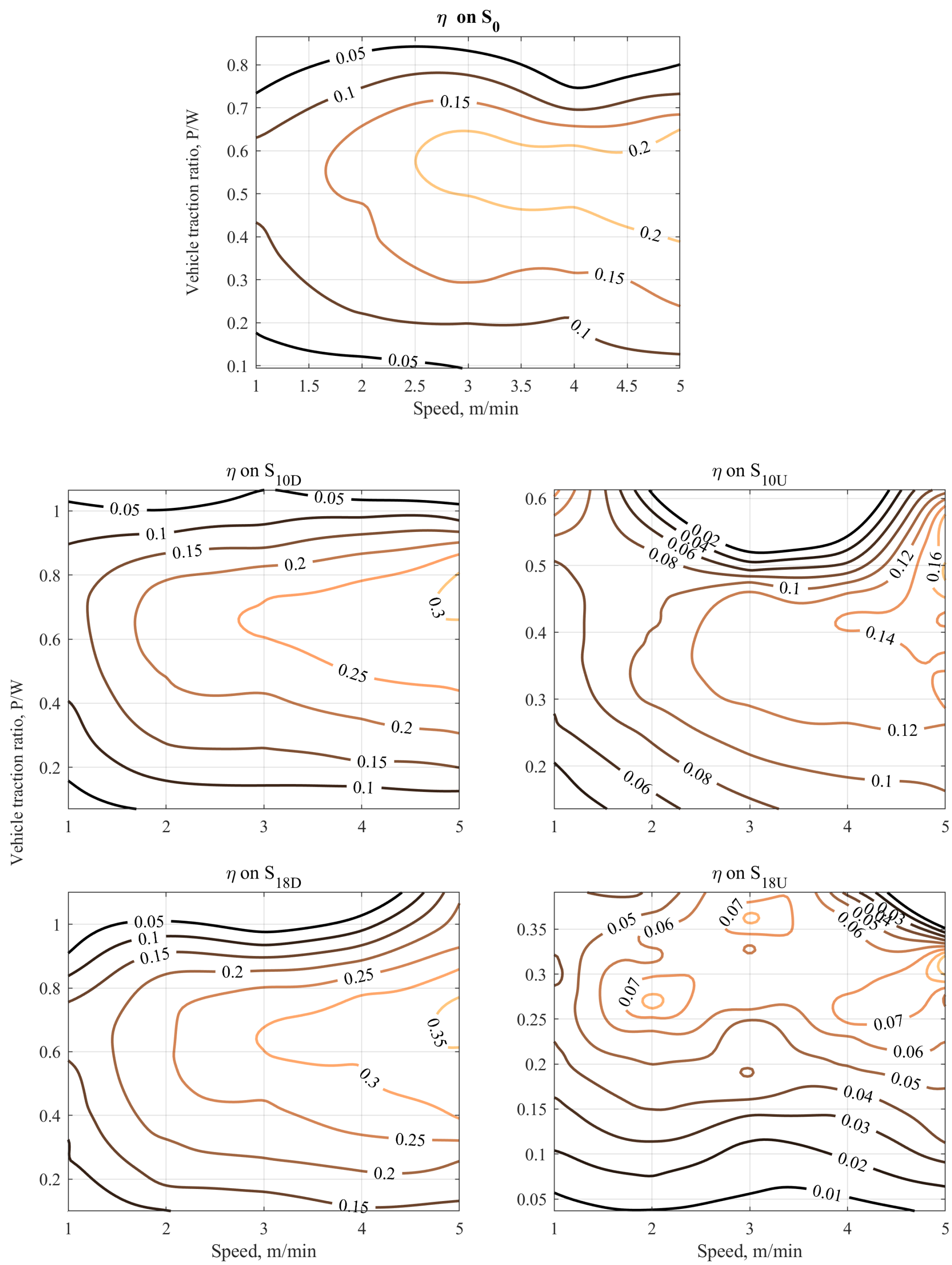

Figure 2.3: *Power efficiency, η, as a function of vehicle speed and traction ratio, P/W, for AGV traveling on level surface, downhill slope, and uphill slope*

of 1, at the cost of reduced PE which was observed only on the downhill operation $\eta \leq 0.5$ and η =0.10 on S_{10D}, and S_{18D}, respectively (Figure 2.3). However, the peak PE observed on S_0, S_{10D}, and S_{18D} was 0.20, 0.25 and 0.30 at 0.55, 0.70, and 0.70 P/W, respectively, illustrating

Table 2.4: *Tractive performance of AGV on slope surface*

Slope	S_0	S_{10D}	S_{18D}	S_{10U}	S_{18U}
η_{max}	0.20	0.25	0.30	0.12	0.07
P/W at η_{max}	0.55	0.70	0.70	0.45	0.30
TR at η_{max}	0.10	0.10	0.10	0.20-0.30	0.20-0.30
PN at η_{max}	2-3	3	3	4-7	4-7
Efficient zone	0.50-0.60 (P/W)	0.50-0.70 (P/W)	0.50-0.70 (P/W)	0.35-0.55 (P/W)	0.25-0.35 (P/W)

that the maximum PE and the maximum P/W cannot be achieved simultaneously[85]. On the other hand, the AGV was unable to generate a drawbar pull equivalent to its weight on the level surface and uphill operation. The maximum P/W was 0.80 for S_0, 0.60 for S_{10U}, and 0.35 for S_{18U} (Figure 2.3).

On a level terrain (S_0), the AGV's peak PE was 0.20, observed at 0.50 -0.60 P/W range and $\geq$ 3 m/min speed with a travel reduction of around 0.10. However, AGV's downhill operation (10 to 18°) showed a significant increase in peak PE with a slight increase in P/W. The peak PE increased by 25% and 50% on slopes 10° (S_{10D}) and 18°(S_{18D}), respectively, compared to 0°(S_0) with a slight increase in P/W from 0.55 to 0.70 (Figure 2.3). The maximum recorded PE was 0.30, observed on 18°(S_{18D}) at a 0.50 -0.70 P/W range and $\geq$ 3 m/min speed with travel reduction ranging between 0.10 and 0.20. However, the AGV's uphill slope (0-18°) operation showed a significant PE decline. The peak PE decreased from 0.20 to 0.12 to 0.7, on 0°(S_0), 10°(S_{10U}), and 18°(S_{18U}), respectively, with a subsequent decline in P/W from 0.55 to 0.45 to 0.30 P/W, respectively (Figure 2.3). Peak PE decreased by 30% and 65% on slope 10°(S_{10U}) and 18°(S_{18U}), respectively, compared to 0°(S_0). This decreased in peak PE could be explained by an increase in the travel reduction from 0.10 to 0.30 on 0°(S_0) and on both 10 and 18° (S_{10U} and S_{18U}), respectively (Table 2.4 and Figure 2.4). Operating the AGV at speed $\leq$ 2m/min was less efficient for the PE than speed $\geq$ 3m/min, except on S_{18U}.

The AGV on 10° slope resulted in the peak PE of 0.25 at 0.70 P/W and 0.12 at 0.45 P/W on S_{10D} and S_{10U}, respectively (Figure 2.3). This AGV's downhill operation generated 108.3% higher PE than the uphill operation with a 55.5% increase in P/W. Similarly, on

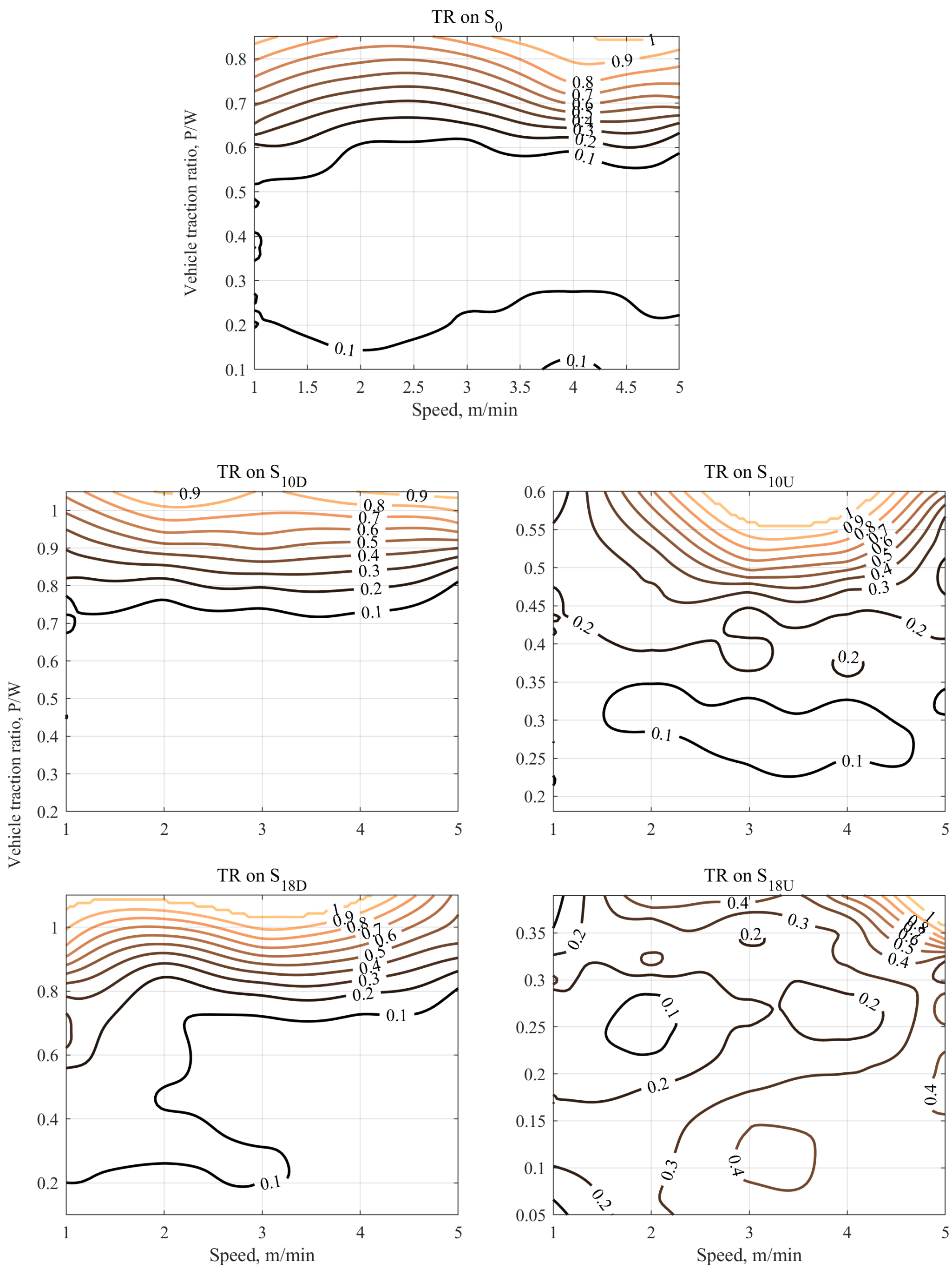

Figure 2.4: *Travel reduction, s (decimal), as a function of vehicle speed and traction ratio, P/W, for AGV travelling on level surface, downhill slope, and uphill slope*

the 18° slope, the peak PE was 0.30 at 0.70 P/W and 0.07 at 0.30 P/W on S_{18D} and S_{18U}, respectively (Figure2.3). This AGV's downhill operation generated 328.6% higher PE than the uphill operation with a 133% increase in P/W. The uphill operation showed a significantly lower PE and P/W than a downhill operation, which could be explained by the increase in travel reduction from 0.10 to 0.30 (Figure 2.4). In other words, there was a 200% increase in travel reduction for both 10° and 18° compared to 0° slope (Table 2.4). The fact that AGV operation was more efficient on a downhill than an uphill slope may sound trivial, but these generated data will be a prerequisite to develop or train mobility models on a sloping terrain environment.

The phenomenon of an increase in PE with a downhill slope, and a decrease in PE with an uphill slope was explained by the AGV's free body diagram on an inclined plane (Figure 2.5). The gravity force (f_{g}) on an incline was resolved into two force components: parallel ($f_{\parallel}$) and perpendicular ($f_{\perp}$). On a level terrain (θ= 0), $f_{\parallel}$ became zero and $f_{\perp}$was at the maximum, balancing the normal force (f_{n}) and gravity force (f_{g}). As slope angle (θ) increased from 0° to 18°, the magnitude of $f_{\parallel}$ increased, and $f_{\perp}$decreased. Thus, $f_{\perp}$ directed opposite to f_{n}, keeping the balance. However, the unbalanced $f_{\parallel}$ increased the net force acting on the AGV. The presence of unbalanced $f_{\parallel}$ (gravity force component) increased with slope angle (θ). The $f_{\parallel}$ caused the AGV to accelerate down the incline. There was greater gravity-induced acceleration of the AGV with a greater slope angle, resulted in higher PE for $\mathrm{S_{18D}}$ compared to $\mathrm{S_{10D}}$. The presence of motion resistance would oppose the AGV gravity-induced acceleration. However, this resulting acceleration became negative in the case of an uphill operation, pulling the AGV downslope, subsequently increasing the travel reduction and reducing the PE for both $\mathrm{S_{10U}}$ and $\mathrm{S_{18U}}$ (Figure 2.3 and Figure 2.4). The AGV's weight transfer and its effect on the track-soil contact pressure distribution may also help explain the AGV's behavior on sloping terrain, but this was not within the scope of the study.

Any drawbar pull exerted to the AGV's hitch point would produce the AGV's travel reduction, due to a track-soil slip and loss within traction elements. Figure 2.4 indicated the range of P/W that delivered the optimum travel reduction (0.10-0.20) and maximum achievable P/W, the AGV can operate before becoming immobilized (s = 100%). The AGV maintained the optimum travel reduction ≤0.20 for a wide range of P/W before reaching the limiting P/W (i.e., maximum value of P/W) that rapidly increased the travel reduction. The

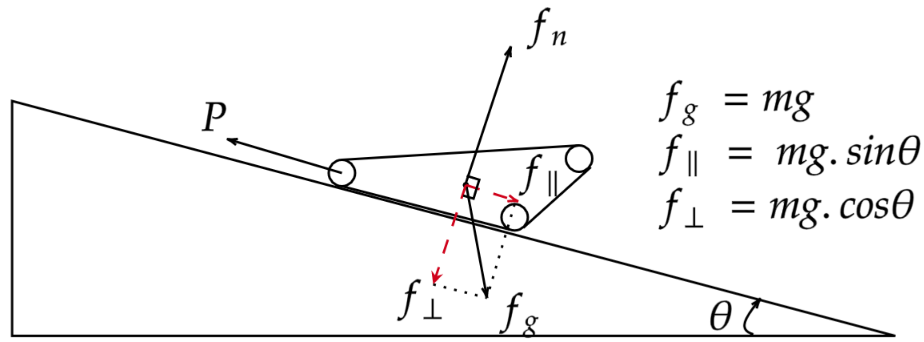

Figure 2.5: *Free body diagram explaining the forces acting on AGV, on a slope*

limiting P/W was observed to vary with the slope angle and was 0.60, 0.80, and 0.80 on S_0, S_{10D} and S_{18D}, respectively (Figure 2.5). On S_0, TR less than 10% was observed for a traction ratio of 0.55-0.60, and after that, TR increased monotonically as the vehicle traction ratio increased (Figure 2.4). A similar trend was observed in Zoz and Grisso (2003)[81] for large agricultural tractors, where TR of less than 10% was observed for a traction ratio of 0.50, and after that, TR increased as the vehicle traction ratio increased. This small AGV' traction performance was in good agreement with the big agricultural tractors traction performance results reported in Zoz and Grisso (2003)[81]. However, on the uphill slope, a gravity-induced acceleration ($f_{\|}$) applied a downslope pulling force to the AGV, increasing travel reduction from 0.10 to 0.30, respectively, on S_0 and both S_{10U} and S_{18U}. Crossing the limiting P/W on an uphill slope did not immobilize the AGV, but pulled the AGV in the direction of the drawbar pull vector. This uncontrolled rapid slide may result in a collision either with an adjacent operating AGV in fleet systems. The AGV was unable to generate substantial PE with applied drawbar pull on S_{18U}, which may restrict the nature of the agricultural operation the AGV could perform on uphill slope greater than 18°.

2.4.2 Mobility energy consumption

An AGV operating on sloping terrain at a minimum energy consumption was desirable. The mobility energy consumption of the AGV on level terrain (S_0) and sloping (S_{10} and S_{18}) terrain was expressed in terms of power number, as a function of P/W and the AGV's speed, as shown in Figure 2.6. The higher the power number the higher the energy consumption. The general shape of power number curve indicated that an increase in P/W increases the power number (Figure 2.6). The P/W influenced the travel reduction and PN, which further influenced the AGV mobility cost. The PN was less than 4 as long as the AGV's travel reduction was around 10% and it increased to a higher value before approaching infinity as travel reduction increased to 100%. The contour plots in Figure 2.6 depicted a maximum PN of 20. A PN value of infinity corresponds to 100% travel reduction because the vehicle's tracks spinning in place would expend all its energy, thereby increasing the cost of mobility.

The contour plots reveal the physical limits for PN corresponding to P on a slope taken under the study. The downhill operation showed a slightly lower PN than the uphill operation, with an increased P/W. The PN corresponding to the peak PE was summarized in Table 2.4. The developed PN versus P/W chart for each slope can be used to estimate the power required to travel on a specific terrain with drawbar load. Hence, this was very useful for mission planning of robotics systems on various terrains.

The ECR computed the AGV's energy expenditure and battery replacement frequency from the available power number data. The ECR at peak PE was calculated with the corresponding power number, and it was 1.0 kWh/km (PN= 3) on S_0, S_{10D} and S_{18D}, and 2.0 kWh/km (PN= 6) on S_{10U} and S_{18U}.

2.4.3 Application of traction database

The study also aimed to generate an AGV's traction-mobility database and characteristic curves on level terrain and variable slopes from -20° to 20° at varying operating drawbar pull and speeds. During the experiment, an efficient zone of the AGV operation (maximum PE for a given set of P/W and speed) was found to shift with the slope angle and direction

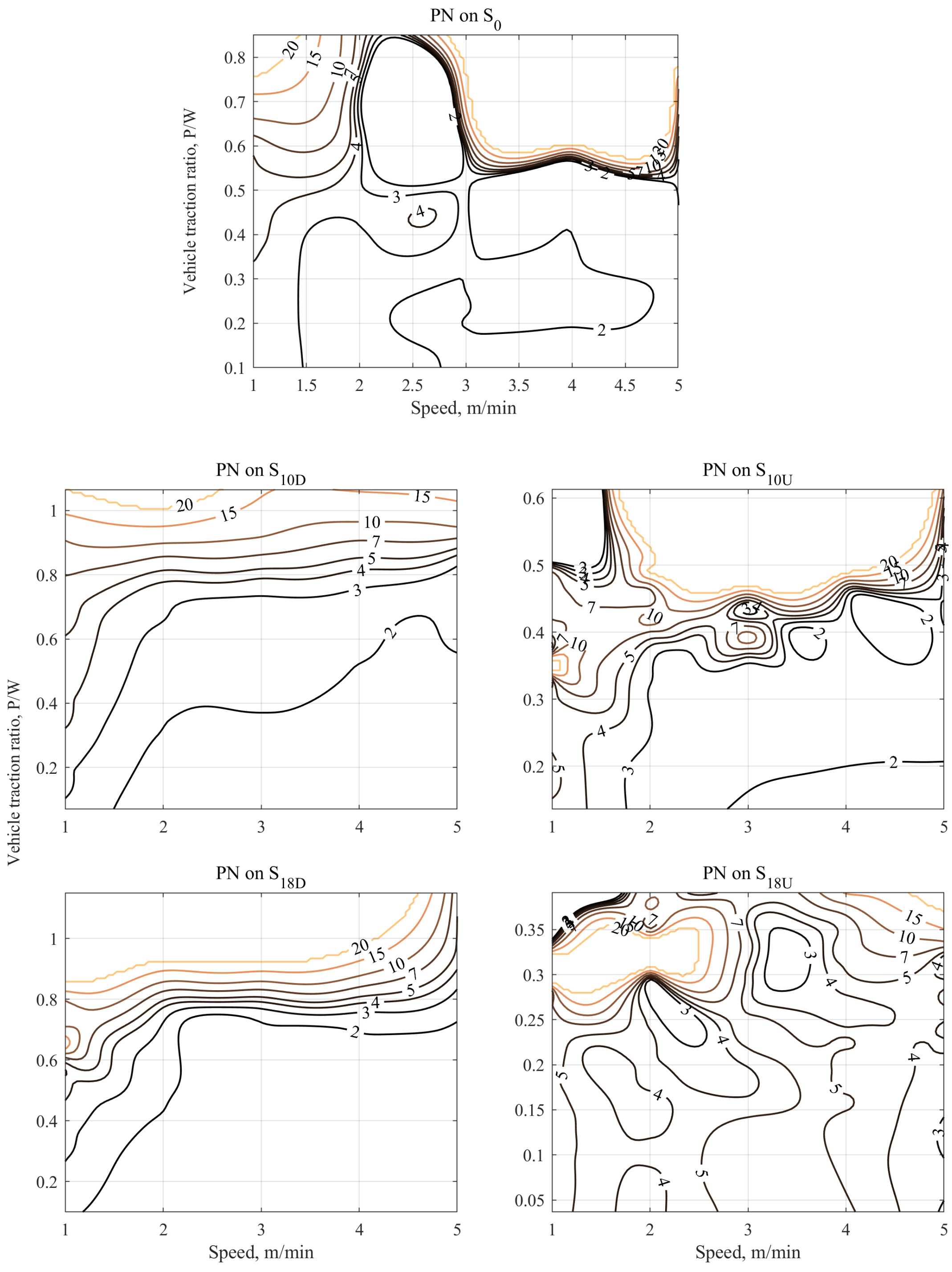

Figure 2.6: *Power number, PN, as a function of vehicle speed and traction ratio, P/W, for AGV travelling on level surface, downhill slope, and uphill slope*

of travel (uphill and downhill). To maximize the AGV's performance, it was important to monitor the shifting efficient zone for each slope angle and direction. Applying P/W beyond the limiting value immobilized the AGV, resulted in 100% travel reduction. However, the optimum range of P/W gave the minimum travel reduction and would decide the nature of the agricultural operation the AGV could perform on a slope. Moreover, peak PE and peak P/W cannot be achieved simultaneously; thus, it was necessary to prioritize between the peak PE or the peak P/W, depending upon the agricultural operation. The AGV was unable to generate significant PE with applied drawbar pull on an uphill slope (18°), eventually causing the AGV to slide in the direction of the drawbar pull vector, which could jeopardize the operation of the entire AGV system. The AGV's operational variables, such as speed and P/W needed to be optimized to maximize the AGV's performance on sloping terrain. To make all these decisions in a dynamic environment, there needs to be a centralized routing algorithm. The data on PE and travel reduction could be utilized to develop a central decision-making algorithm, which generated vehicle mobility, design, safety, and route-optimization models for highly sloped soil terrain. The power number data would be used for mission planning, energy optimization, battery swapping frequency, and path optimization models since, for a given P/W, the cost of going uphill was greater than the cost of going downhill. This would assist in achieving an efficiently powered AGV system. Also, before the AGV's actual field operation, computer simulations can be performed on a digital terrain model for the desired slope to check and predict the AGV's application feasibility and go-no-go situation. The developed centralized algorithm or models generated from a traction database in a controlled laboratory environment can be extended to a sloping environment. These models would predict specific dynamic responses, including PE, travel reduction, and power numbers from inputs including duty cycle, P/W, terrain slope, and soil characteristics (Figure 2.7).

2.5 Conclusions

A prototype AGV's tractive performance was evaluated on a level terrain and variable slope up to 18° (both uphill and downhill) at varying drawbar pull and operating speed conditions on a soil bin. The performance was expressed in power efficiency, travel reduction, power

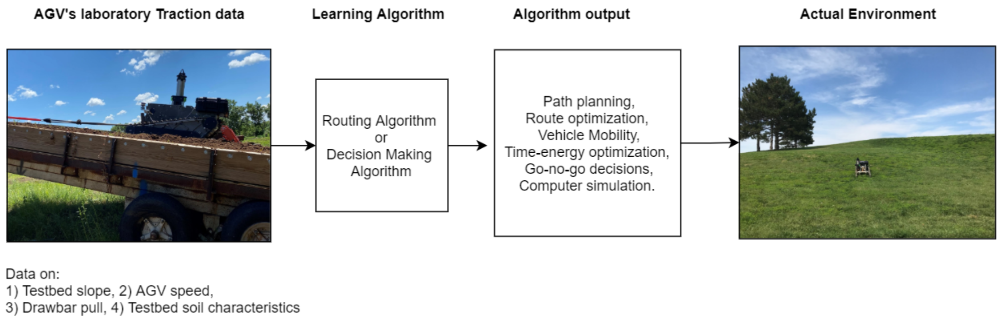

Figure 2.7: *Traction data application for proposed robotic system*

number and energy consumption rate. From the observed data, the following conclusions can be drawn.

- The AGV generated a drawbar pull equivalent to its own weight (P/W = 1) at the cost of reduced PE only on a downhill slope. Maximum PE and maximum P/W cannot be achieved simultaneously. However, the AGV on the uphill slope resulted in significantly lower P/W and the maximum value of 0.6 and 0.4 P/W was observed on 10° and 18° uphill, respectively.

- Power efficiency increased with an increase in the downhill slope angle with a slight increase in P/W and was significantly higher for downhill than uphill operations for the same slope angle but with a significant increase in drawbar pull. Power efficiency increased by 25% and 50% on 10° and 18° downhill slopes, respectively compared to 0°. Power efficiency was 108.3% and 328.6% higher on the downhill than uphill run with a 55.5% and a 133% increase in P/W, on 10° and 18° slopes, respectively.

- Travel reduction was a major source of power loss caused by applying drawbar pull. However, the AGV maintained the optimum TR $\leq$ 20% for a wide range of P/W before reaching the limiting P/W 0.60, 0.80, and 0.80 on 0°, 10° and 18° downhill slopes, respectively.

- The optimum values of power number ranged from 2 to 4. The ECR, at maximum PE, ranged from 1.0 kWh/km to 2.0 kWh/km.

In summary, the AGV delivered optimum power efficiency and generated enough drawbar pull with optimum travel reduction and power number. This study found that the prototype AGV can successfully operate on slopes up to 18°, so high-sloped terrain or hills could be farmed with the proposed AGV system. Nevertheless, the AGV system serving on high-sloped terrain needs a robust and efficient decision-making algorithm to predict and optimize the AGV's operating parameters on various terrains.

Chapter 3

Artificial neural network to predict traction performance of autonomous ground vehicle on a sloped soil bin and uncertainty analysis[1]

3.1 Abstract

A fleet of autonomous ground vehicles (AGVs) is envisioned to expand farming to arable land suitable for production except for being too steep for conventional equipment. The success of the proposed AGV system largely depends on the traction performance of the individual AGVs on unevenly sloped terrain and optimization of the AGVs control variables. Therefore, the drawbar pull performance of a prototype AGV was evaluated in a soil bin at varying slopes, speeds, and drawbar pull (DP). The AGV's traction performance was expressed in three metrics: tractive efficiency (TE), travel reduction ratio (TRR), and power number (PN). Optimizing the control variables is intricate and ill-defined, which requires an accurate model to predict the performance of the proposed system. Hence, this study aimed to design an artificial neural network (ANN) to estimate the traction behavior of the AGV on a sloped testbed as a function of the AGV's speed, applied DP, and slope. A multi-layer perceptron

[1]Results were published as a peer-review article. Badgujar, C., Flippo, D., & Welch, S. (2022). Artificial neural network to predict traction performance of autonomous ground vehicle on a sloped soil bin and uncertainty analysis. *Computers and Electronics in Agriculture*, 196:106867, 2022. doi: 10.1016/j.compag.2022.106867

feed-forward ANN architecture with a single hidden layer trained with a back-propagation algorithm was adopted. A series of ANN models with increasing complexity and different hidden layer activation functions were developed for each response variable, i.e., ANN-TE, ANN-TRR, and ANN-PN. A re-sampling-based method called, K-fold cross-validation, was employed to estimate the model generalization error. The model success was evaluated via Mean Squared Error (MSE) and the Coefficient of Determination (R^2) against a test set. The final predictive model was trained on the entire data set, and the observed R^2 was 0.933, 0.882 and 0.858, respectively, for ANN-TE, ANN-TRR, and ANN-PN. Subsequently, a Monte-Carlo Simulation based uncertainty analysis was carried out to demonstrate the model strength and the degree of uncertainty by constructing a 95% prediction interval. The study showed that ANN as a promising, robust, and reliable method to predict traction performance in agricultural tillage-traction studies and developed models can empower the robotic system on steep-uneven slope terrain.

3.2 Introduction

Cropland expansion remains one of the leading factors in global agricultural production growth to meet the rising demands of food, fiber, and fuel of an escalating population[38;86;87]. However, hills, uneven terrain, and excessive steepness of grassland ($> 6°$) preclude farming with conventional agricultural machines[38]. On sloping terrain, tractor rollovers are more frequent and one of the leading causes of farmer injury and/or death during farm operations[36;37]. This impediment could be potentially and sustainably addressed with a fleet of small autonomous ground vehicles (AGV). Multi-AGV systems are rapidly gaining interest for smart farming and are prime candidates for future outdoor agriculture[35;88]. AGVs can accomplish work equivalent to a large conventional machine but with reduced soil compaction, better accuracy and can be programmed to work at peak efficiency without human intervention[47;89–93]. There is abundant evidence suggesting robots/AGVs can perform various agricultural operations, including seeding and transplanting[94–96], plant protection and weed control[97;98], fruit-vegetable harvesting[99–101]; with robust field localisation and mapping[102–104].

The success of the proposed system largely depends on the traction performance of the individual AGVs on unevenly sloped terrain. Traction performance is defined by the net traction ratio and the tractive efficiency[105;106], which quantifies the amount of tractive effort generated for the agricultural task, the power consumed, and the nature of the agricultural operation (i.e., tillage types and input carrying capacity) the AGV could perform. Major factors affecting ground vehicle performance on sloping terrain are terrain tilt, operating direction (i.e., uphill, downhill, sideways), lateral slippage, applied drawbar pull, and vehicle speed[107]. Therefore, to understand sloped terrain AGV performance, controlled laboratory experiments must be carried out to develop models explaining the influence of the AGV's operational variables on these parameters. The resulting models can describe vehicle behavior, help to improve the vehicle design, optimize operational parameters, and minimize energy consumption. Furthermore, a performance model from limited laboratory experiments can be extended to a dynamic terrain environment for a decision support system, path planning, route optimization, power optimization, and so on.

In the last few decades, a variety of modeling techniques including analytical, empirical, and semi-empirical, have been implemented to predict or measure the traction performance of both wheeled and tracked vehicles either on controlled soil bin conditions or unprepared fields[75;108–117]. These models helped to understand and establish vehicle traction performance (primarily tractor) to improve and optimize its operational parameters[117]. In analytical methods, traction parameters were determined from soil-tire/track contact surface geometry and stress distribution (normal and shear). Nevertheless, the complex nature of soil-tire interactions, varying soil parameters, and inadequate information of boundary conditions were major challenges for its adoption[117;118]. Empirical traction models are obtained from large amounts of experimental data, and often yield constants and coefficients pertaining to specific experimental conditions. This restricted their applicability in a dynamic agricultural environment as well as for different vehicle type/configurations[117;119]. Semi-empirical models are easy to use and are derived from both experimental data and fundamental analysis of soil-tire interaction. However, assumption-dependent model development processes limited their accuracy in different terrain and vehicle types.

The limitation of existing modeling techniques, demands for models with better prediction capabilities and advancements in data-driven computer science and has inspired researchers to develop traction models based on machine learning approaches, such as artificial neural networks (ANN). ANN is a robust modeling method that draws on loose analogies to natural neural tissue combined with an automated model selection process. In recent years, ANN has emerged as a promising tool to model and analyze very complex problems in biological and agricultural domains[120]. ANN was widely used to predict the traction performance of tractors and tillage implements as affected by various machine and soil parameters[106;107;121–127].

The predictive capability of several ANN configurations was assessed by Almaliki et. al.,(2016)[125] for tractor performance, in terms of tractive efficiency, drawbar power, rolling resistance, and fuel consumption. Their results confirmed ANN ability to learn the relationships among input variables and tractor performance parameters. Ekinci et.al.,(2015)[106] designed seven different ANN models with a single hidden layer to predict the tractive performance (i.e., tractive efficiency) of radial tires fitted on off-road vehicles. Given inputs of lug height, axle load, inflation pressure, drawbar pull, and trained with the Levenberg–Marquardt algorithm, the resulting ANN successfully predicted tractive efficiency. While, as exemplified by the citations above, ANNs have frequently been used to model the performance of human-operated tractors. To the best of our knowledge, this has not been done for AGVs. Neither, apparently, has terrain slope been used as a predictor variable and its influence on AGV's traction performance is unknown to date.

ANN model development is stochastic in nature, and an identical ANN trained on the same data produced different results on each run owing to random data splitting methods and random ANN parameter initialization. Therefore, it is necessary to quantify the prediction uncertainty of the final model, especially given that it will be utilized to optimize control variables and decision making. Uncertainty analysis (UA) assesses the model output error and quantifies the output variability based on input variability. Monte-Carlo Simulation (MCS) is a well-established technique to quantify the uncertainty of ANN model prediction. It computes the model error emerging from data uncertainty (inherent noise) and model uncertainty. The MCS was first proposed by Marce et.al., (2004)[128] for ANN and since then has been implemented in several other studies, mostly in environment and climate[129–132]. However, very little if any information is available on ANN uncertainty analysis in agricultural tillage and traction domain.

Therefore, the objective of this study was to develop an ANN model to predict AGV traction performance in a sloped soil bin as a function of slope, speed and drawbar pull. Moreover, to investigate the output uncertainty of the developed ANN model, an MCS-based uncertainty analysis was carried out. The resulting traction prediction model would improve vehicle performance by optimizing its operational variables and establish the boundary conditions on sloped terrain. Moreover, the traction prediction model would assist in vehicle design, safety, and the optimization of the energy and mobility aspects on highly sloped and uneven terrain.

3.3 Materials and methods

To develop the AGV's traction model, a large amount of data is a prerequisite. A standard drawbar pull (DP) test characterizes off-road vehicle performance[50] and measured a vehicle's total tractive ability[49]. Thus, a DP performance of the AGV was carried out in a soil bin on a testbed slope ranging from 0-20° for both uphill and downhill runs. The AGV's details, testbed conditions, testing procedure, instrumentation setup, experimental setup, data collection and pre-processing were described in detail in Chapter 2. The generated traction data in Chapter 2 was used to develop the AGV's traction model. The statistical summary of the response variables were presented in Table 3.1.

3.3.1 ANN model development

ANNs are adaptive systems using interconnected computational units called neurons arranged in a layered structure, and able to learn a complex and nonlinear relationship be-

Table 3.1: *Statistics of experimental data for the response variable*

Response	Minimum	Maximum	Mean	Standard deviation
Tractive efficiency (TE)	0.00	0.48	0.14	0.09
Travel reduction ratio (TRR)	0.02	1.00	0.33	0.33
Power number (PN)	0.77	20*	6.07	5.59

* PN explodes to infinity (when TRR =1), therefore upper limit 20 is considered.

tween inputs and outputs. ANNs integrate several distinct information processing layers (eg., input, hidden, and output layers) composed of nodes ("neurons") with weighted interconnections that present the previous layer's output to the next layer as inputs. Each node has an activation function, that converts its inputs to outputs. In the learning phase, the interconnection weights are iteratively adjusted according to a specified learning method until the desired output is obtained for each training sample.

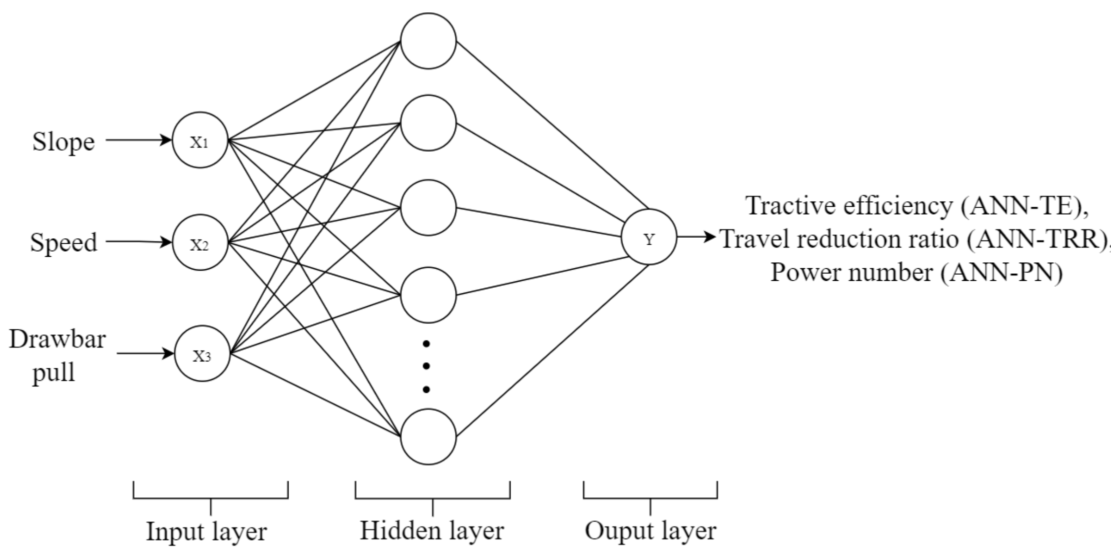

Figure 3.1: *Multi-layer perceptron ANN architecture implemented in study*

The development of an ANN model with linearly dependent inputs is a methodological mistake[133]. Linearly correlated inputs may lead to a multi-colinearity problem[132;134]. Therefore, before developing an ANN model, possible linear correlations between inputs were examined by computing the Pearson correlation coefficients. A multi- layer perceptron (MLP) ANN trained with the Levenberg-Marquardt back-propagation (LMBP) algorithm was implemented as shown in Figure 3.1. The inputs to the ANN were slope, speed and drawbar pull and a single response neuron produced the output. Therefore, three independent predictive ANN models were developed: ANN-TE, ANN-TRR and ANN-PN.

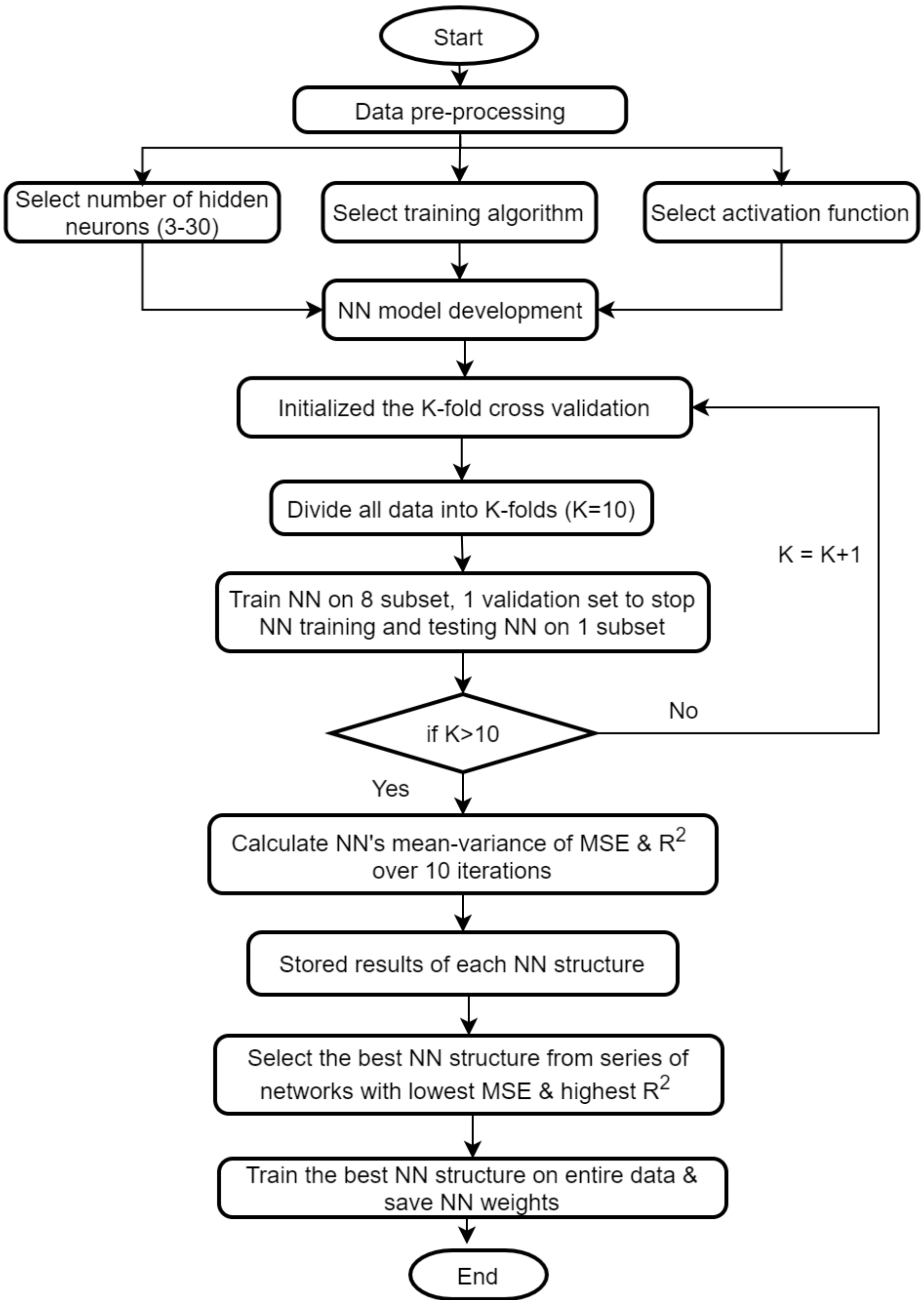

Figure 3.2: *Flowchart for selection of the best multi-layer feed forward network architecture*

The flowchart of ANN model development was shown in Figure 3.2. The data pre-processing step included the input data normalization to a mean zero and unit variance. The pre-processing step facilitated a network training process to extract the relevant information as well as to speed up the training. In MLP, the input and output layer neurons were decided by the number of model input and output variables, respectively. The number of neurons in the hidden layer significantly influenced the model performance but there was no analytical solution available to determine how many to use. Thus, this choice was left to trial and error[125;126;133]. In this study, the number of neurons in the hidden layer was varied from 3 to 30 for each ANN model, with each additional neuron increasing the ANN complexity. The neuron weights and biases were randomly initialized and then iteratively adjusted by the LMBP algorithm to minimize prediction errors against the set of training data[135;136]. An early stopping criterion was used to prevent model overfitting – namely, training was stopped when the validation set performance increases for a set number of iterations (here 6). The weights and biases at the minimum of the validation error were preserved. Two different nonlinear activation functions (i.e., log-sigmoid and hyperbolic-tangent sigmoid) were evaluated for use in the hidden layer to capture the complex and non-linear relationships within data. A linear activation function (purelin) was used in the output layer because the target variables were continuous. The various numbers of hidden neurons (3 -30) in combination with the two different activation functions generated 56 independent ANN structures for each output variable.

A re-sampling-based model validation technique called K-fold cross-validation (CV) was employed to elect the best ANN from each set of 56 ANN and to estimate the generalization error[137;138]. In K-fold CV, the traction data (1288 observation) was divided into K (here 10), approximately equal-sized and non-overlapping subsets. The ANN was trained on eight subsets (1032 observations) and the remaining two subsets (each 128 observations) served, respectively, as an early-stopping validation set to prevent over-fitting and a test set to assess model performance. This process was repeated ten times, selecting alternate subsets to train each ANN structure and to assess the performance on the corresponding test subset. The model performance was evaluated with two metrics: Mean Square Error (MSE) and Coefficient of Determination (R^2). Each ANN model was trained on ten different non-overlapping data subsets, provided that each subset appeared in the test set once and the mean and variance of MSE and R^2 were computed over 10 runs (Figure 3.2). For each dependent variable, the network with the lowest MSE and the highest R^2 on the test set was selected among the series of ANNs. This best performing ANN structure was finally trained on the entire dataset, and split randomly into training (90%), and validation (10%) sets. The weights and biases of the final predictive ANN models were saved in a computer for each dependent variable. During prediction, the ANN model provided a respective output in its original units.

3.3.2 Uncertainty analysis

The ANN model predictions are not certain and the prime source of this uncertainty emerges from random initialization of weights-biases, training data splitting methods, and selection of ANN structure[139–141]. In this study, the uncertainty analysis was performed on the final predictive models, keeping the ANN structure fixed, and the uncertainties emerging from random training data sampling and random weight initialization were quantified. The uncertainty analysis showed the effect of model inputs or model parameters on the ANN simulations results. A Monte Carlo simulation (MCS) was performed to quantify the uncertainty of the final predictive ANN model. MCS involved retraining the ANN multiple times (here 1000) on randomly re-sampled data without replacement, maintaining the train-validation-test set ratio unchanged. Thus, a single ANN structure trained with MCS, generated 1000 outputs corresponding to each observed output. Therefore, a cumulative distribution function of the output was constructed. The 95 percent prediction uncertainties/interval (95 PPU) was determined from the associated output distribution by taking the 2.5$^{\text{th}}$ (X_L) and 97.5$^{\text{th}}$ (X_U) percentiles[129]. The 95 PPU interval provided the range of prediction associated with the ANN model. The ANN uncertainty was expressed interms of the degree of uncertainty $\overline{d_x}$ and the percentage of true data bracketed by the 95 PPU interval as suggested by[129;142].

$$\overline{d_x} = \frac{1}{n} \sum_{i=1}^{n} (X_U - X_L)$$

where, n was the number of true observations. The ideal model delivered 100% of the observations bracketed by 95 PPU and $\overline{d_x}$ reaches to zero. However, the ideal results were not achievable, because of model uncertainty. Thus, a reasonable measure of $\overline{d_x}$ was calculated by d-factor as follows[129;142]:

$$d - factor \ = \ \frac{\overline{d_x}}{\sigma_x}$$

where, σ_x was the standard deviation of the output variable X. The larger d-factor, the higher the uncertainty and vice-versa[142]; values less than 1 were desirable. The true data bracketed by 95 PPU were calculated as follows[129] where a higher percentage of 95 PPU was desirable:

$$Bracketed\ by\ 95\ PPU = \frac{1}{n}\ count(X|X_L \leq X \leq X_U) \times 100$$

3.4 Results and discussions

3.4.1 ANN models

Table 3.2 showed the Pearson Correlation Coefficients between the ANN input variables. A very weak correlation was observed between the speed-slope and speed-drawbar pull, with a coefficient value of 0.01 and 0.06, respectively. A drawbar pull-slope exhibited a positive weak correlation with a coefficient value of 0.39. DP was found to be correlated with other two ANN inputs (speed and slope), with a p-value less than 0.05. However, DP and speed were a major indicator of the AGV's traction performance (TE, TRR and PN) and must be taken into account as input variables. Hence, all three predictors were included in ANN model development.

The performance of the ANN was observed on the test set and the performance statistics (MSE and R^2) of the five best ANN structures for ANN-TE, ANN-TRR and ANN-PN and were summarized in Table 3.3. Lower MSE and higher R^2 values were better. Boldfaced table entries indicated the optimal combinations of hidden layer sizes and activation functions for each output variable. The optimum numbers of hidden neurons were 22, 22 and 30 for

Table 3.2: *Pearson's coefficient (lower left to diagonal) and p-values (α =5%) (upper right to diagonal) for predictor variables*

	Slope	Speed	Drawbar pull
Slope	1	0.60	0.00
Speed	0.01	1	0.02
Drawbar pull	0.39	0.06	1

ANN-TE, ANN-TRR and ANN-PN, respectively. Tansig was the best activation function for ANN-TE, ANN-TRR and logsig for ANN-PN. The final ANN model was trained on an entire data set and the results were presented in Table 3.4. A high value of R^2 (>0.90) and a low value of MSE on the training, validation and entire data sets was obtained for ANN-TE, showing the high model quality. The R^2 of ANN-TRR and ANN-PN models ranged between 0.84-0.88% which was considered satisfactory model performance. A comparatively high sample standard deviation of ANN-TRR (0.33) and ANN-PN (5.6) (Table 3.1) explained the lower value of R^2.

The regression analysis and residual distribution of the ANN-TE, ANN-TRR and ANN-PN models were depicted in Figures 3.3, 3.4 and 3.5, respectively. A high regression correlation was observed for ANN-TE and ANN-TRR as shown in Figures 3.3a and 3.4a, a R^2 of 0.933 and 0.88, respectively. The closeness of the scattered data to a unity slope indicated the good performance. Moreover, no definite pattern was observed in the model residuals for ANN-TE, ANN-TRR and ANN-PN as shown in Figures 3.3b, 3.4b and 3.5b.

The developed traction models successfully demonstrated the ability of ANN to explain a non-linear, complex, and ill-defined relationship of small track ground vehicle traction behavior on sloping terrain as a function of slope, speed, and applied drawbar load. Once trained, ANN models predicted the desired output with good generalization ability at a very high speed, indicating that ANN models were fast, accurate, and reliable. The results of this study were in agreement with the previous similar studies conducted on the agricultural tillage and traction domain. These studies included ANN modeling on laboratory traction data obtained on radial tractor tires[106], ANN model development on data obtained from tractor-implement studied at different field conditions[125], and validation of ANN framework for predicting the tractive efficiency of four-wheel drive agricultural tractor[126]. The studies mentioned above reported the R^2 higher than 90% for the developed ANN model, which showed ANN can capture the input and output relationship with better accuracy. The ANN-based model offered multiple benefits such as speed, robustness, and better accuracy than the traditional modeling approach, including analytical, empirical, and semi-empirical methods. The ANN-based approach would be the best alternative to model intricate agricultural soil, tillage, and traction interactions.

Table 3.3: *K-fold cross-validation results for five best models on the test set*

Predictor	ANN	Hidden-layer activation	MSE_{mean}	MSE_{min}	MSE_{std}	$R^2{}_{mean}$	$R^2{}_{max}$	$R^2{}_{std}$
TE	3-20-1	Logsig	0.0007	0.0004	0.0002	0.917	0.942	0.017
	3-22-1	**Tansig**	**0.0007**	**0.0004**	**0.0002**	**0.919**	**0.938**	**0.018**
	3-25-1	Logsig	0.0007	0.0004	0.0002	0.917	0.940	0.017
	3-26-1	Tansig	0.0007	0.0004	0.0002	0.915	0.937	0.021
	3-29-1	Logsig	0.0007	0.0004	0.0002	0.917	0.937	0.019
TRR	**3-22-1**	**Tansig**	**0.016**	**0.011**	**0.004**	**0.847**	**0.900**	**0.038**
	3-25-1	Logsig	0.016	0.010	0.004	0.844	0.904	0.042
	3-26-1	Tansig	0.016	0.012	0.003	0.846	0.894	0.037
	3-27-1	Tansig	0.016	0.011	0.003	0.843	0.896	0.040
	3-29-1	Tansig	0.016	0.011	0.004	0.844	0.900	0.043
PN	3-23-1	Logsig	5.65	3.31	1.76	0.821	0.883	0.058
	3-26-1	Tansig	5.55	3.37	1.41	0.821	0.883	0.050
	3-27-1	Tansig	5.58	3.58	1.39	0.823	0.872	0.043
	3-30-1	**Logsig**	**5.51**	**3.63**	**1.20**	**0.826**	**0.872**	**0.039**
	3-30-1	Tansig	5.57	3.63	1.40	0.823	0.876	0.046

Table 3.4: *Parameters of ANN's used as best neural models*

Predictor	ANN structure	MSE			R^2		
		train data set	validation data set	all data set	train data set	validation data set	all data set
TE	3-22-1	0.0005	0.0008	0.0006	0.936	0.902	0.933
TRR	3-22-1	0.012	0.015	0.012	0.886	0.847	0.882
PN	3-30-1	4.45	4.42	4.44	0.859	0.841	0.858

Figure 3.6 showed the effectiveness of an early stopping method to prevent overfitting

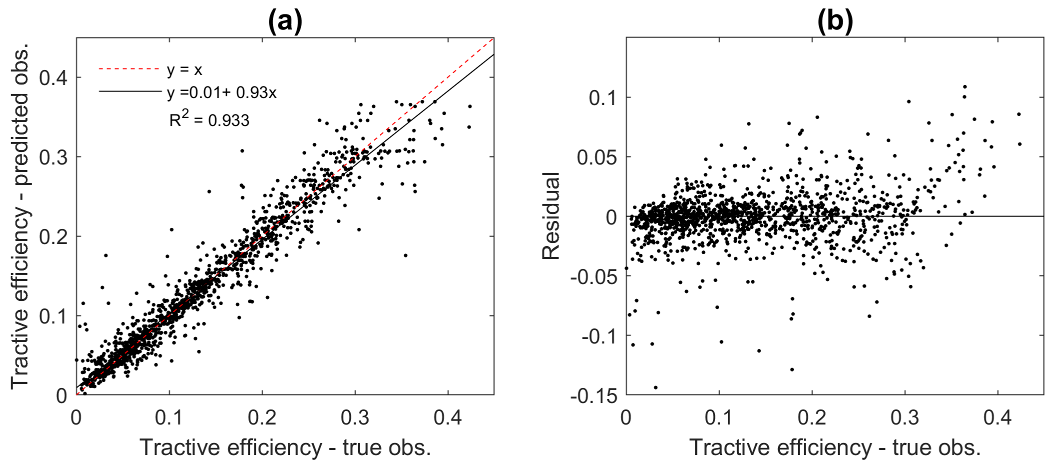

Figure 3.3: *ANN-TE (a) regression between predicted against true obs. (b) distribution of model residual*

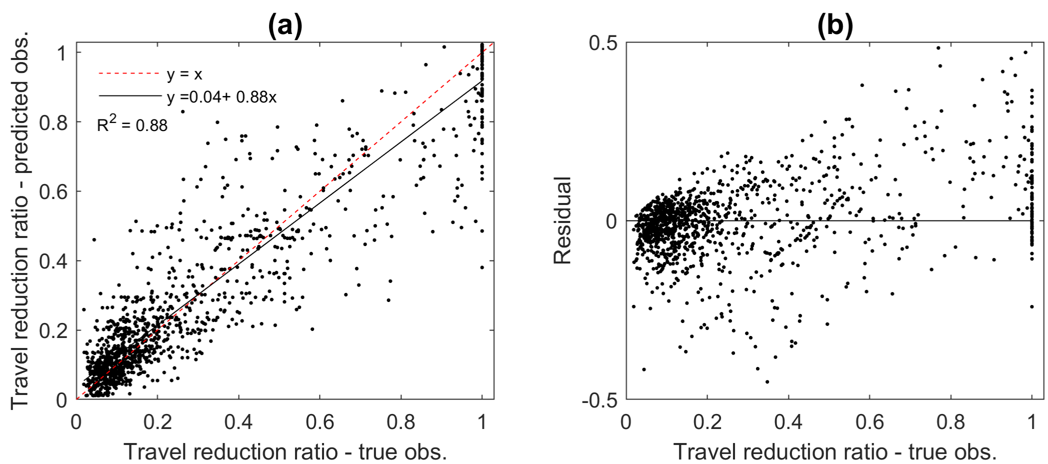

Figure 3.4: *ANN-TRR (a) regression between predicted against true obs. (b) distribution of model residual*

on ANN-TE. It stopped the training at a point when validation performance started to degrade (Figure 3.6b). Without the early stopping method, the validation set was absent, and the ANN trained for a set number of epochs. This overfitted the training data and poor performance was observed on the test set (Figure 3.6a).

3.4.2 Uncertainty analysis

The MCS uncertainty analysis was conducted on the final ANN structure for each output variable and the results were summarized in Table 3.5. A 95 PPU for each output variable

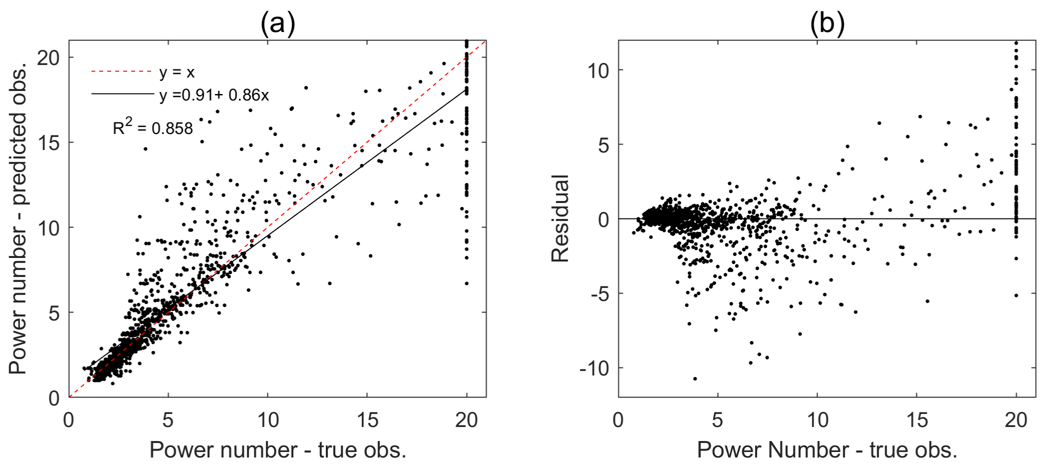

Figure 3.5: *ANN-PN (a) regression between predicted against true obs. (b) distribution of model residual*

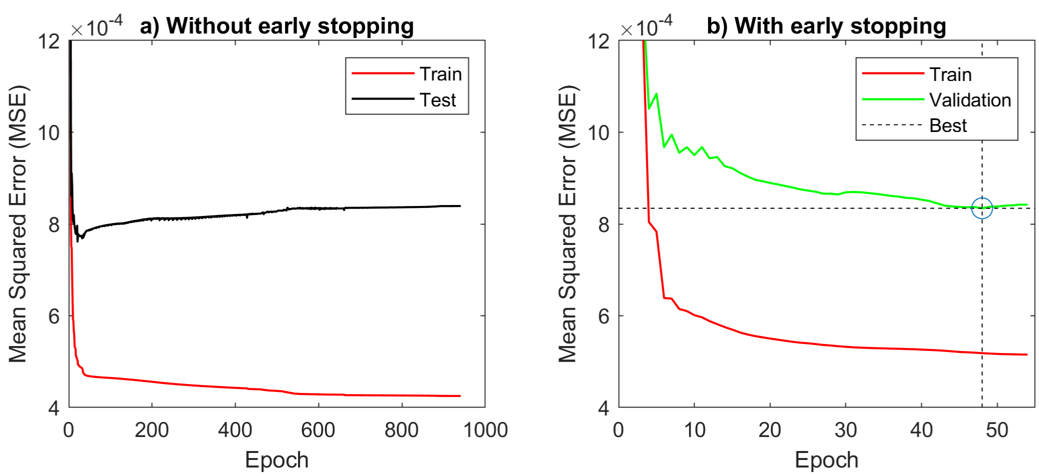

Figure 3.6: *Early stopping criteria: Overfitting prevention strategy for ANN-TE*

was shown in Figure 3.7. The 95 PPU exhibited reasonable general behavior for the true observations, although a few observations tend to exceed the lower and upper bound, as shown in Figure 3.7.

The wider the 95 PPU, the lower the ANN prediction accuracy and vice-versa[129]. Figure 3.7 depicted a wider prediction interval for ANN-PN and ANN-TRR compared to ANN-TE, hence, a greater d-factor was reported for ANN-PN (0.42) and ANN-TRR (0.41) compared to ANN-TE (0.28) which explained the degree of uncertainty associated with each model. Therefore, the ANN-PN and ANN-TRR exhibited higher uncertainty compared to ANN-TE. However, the wider prediction interval enclosed a relatively higher number of predictions

Table 3.5: *Results of uncertainty analysis of ANN models*

Dependent variable	ANN structure	$\overline{d_x}$	d-factor	Bracketed by 95 PPU (%)
TE	3-22-1	0.03	0.28	60
TRR	3-22-1	0.13	0.41	64
PN	3-30-1	2.38	0.42	79

bracketed by 95 PPU for ANN-PN (79%) and ANN-TRR (64%) compared to ANN-TE (60%) as shown in Table 3.5. The 95 PPU explained the robustness of the final ANN model. The average distance between the lower and upper bounds of predictive interval was explained by the $\overline{d_x}$. The d-factor lower than 1 was acceptable, thus, all three ANN models were within an acceptable limit. MCS uncertainty analysis explained the robustness and reliability of the developed ANN models. The constructed prediction interval can be used for decision making of AGV operation on sloped terrain and computer simulations.

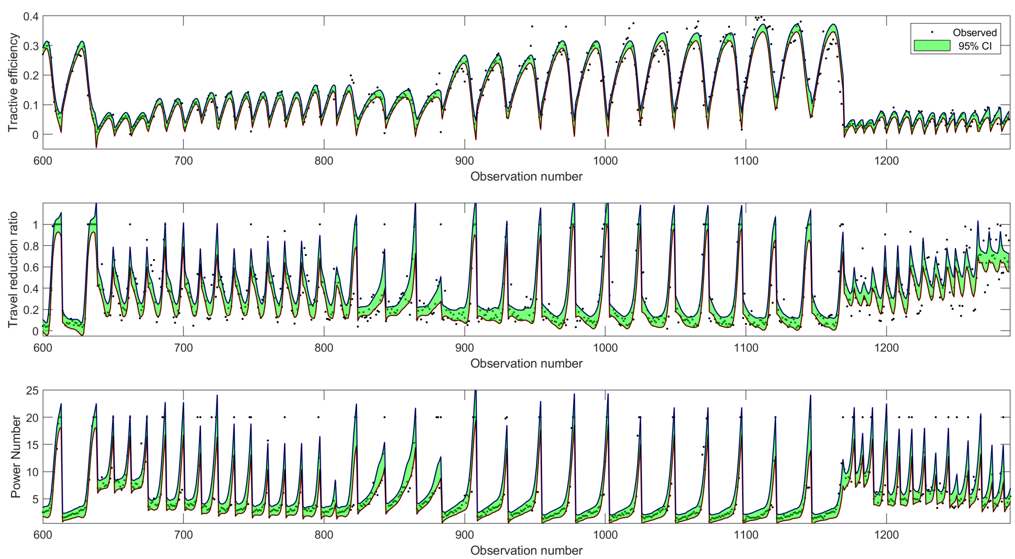

Figure 3.7: *95% PPU for (a) TE-ANN, (b) ANN-TRR and (c) ANN-PN*

3.5 Conclusions

In this study, we investigated the ability of ANN to predict the traction performance of the AGV on slopes in terms of TE, TRR and PN as a function of the AGV's speed, applied drawbar pull and testbed slope. A series of ANN of increasing complexity was developed for each output variable and the 10-fold CV was used to check the generalization ability on the test set. For each output variable, the best ANN structure was identified and a final predictive model trained on the entire data set. A Monte-Carlo simulation analysis (1,000 run) was performed separately on the selected ANN structures. The following conclusions can be drawn from this study,

- A three-layer ANN architecture with a nonlinear activation function can predict the traction performance of AGVs with good generalization ability.
- ANN structure influenced the model performance and increasing the size of the hidden layer ensures improved performance before the start of data overfitting. The optimum number of hidden neurons for TE, TRR and PN were 22, 22 and 30, respectively.
- MCS based uncertainty analysis further strengthened the ANN ability to predict the AGV's traction performance by constructing 95% prediction intervals. It quantified the reliability and robustness of ANN model output. The degree of uncertainty was in acceptable limits for all models, even-though, a few observed data points were outside the 95% prediction interval.
- ANNs were fast, accurate, and reliable tools to predict AGV traction performance in a sloped soil bin.
- Such predictive traction models can empower the entire AGV system operation in a dynamic agricultural environment by assisting in vehicle control variables optimization, establishing the vehicle boundary conditions on slopes, energy optimization and decision making regarding the application feasibility, and go-no-go situation ahead of time.

Chapter 4

Deep neural networks to predict autonomous ground vehicle behavior on sloping terrain field[1]

4.1 Abstract

Uneven terrain or highly sloped hills precludes farming with conventional agricultural machines. In response, a fleet of autonomous ground vehicles (AGVs) is proposed to cultivate marginalized sloped terrain. The fleet traversing the continuously varying terrain needs optimized path planning and a decision-making algorithm. To enable this, the drawbar pull performance of a single AGV was conducted on continuously varying sloping terrain and expressed in terms of traction, mobility, and energy consumption. The experimental data were employed to develop a new machine learning model to predict the AGV traction, slip, energy consumption as a function of vehicle velocity, drawbar, and slope. The proposed model combined multiple deep neural networks with a mixture of Gaussians. A hybrid training method was developed to simultaneously train the model parameters. When compared to other well-known machine learning methods for regression, the proposed model consistently outperformed the others in terms of a set of four performance measures. The study explored the capabilities of the machine learning algorithms to simulate the behavior of small

[1]Results was in under review as a peer-review article. Badgujar, C., Flippo, D., & Welch, S. (2022). Deep neural networks to predict autonomous ground vehicle behavior on sloping terrain field. Journal of the Field Robotics.

track vehicles on sloping terrain. The developed model would empower the fleet's operation on sloping terrain by assisting in vehicle path planning, route optimization, and decision making.

4.2 Introduction

Arable steep grassland ($> 6°$ slope), hills, and uneven terrain pose challenges to farming operations with traditional agricultural machines or implements[38]. Tractors and other off-road agricultural machines operating on steep slopes and uneven terrain are at high risk of rollover and tip-off incidents. In the United States, tractor overturns are frequent; resulting in either severe or fatal injuries to the farmer and approximately 130 deaths are reported each year[143]. This technological barrier to slope farming has prevented arable land from being cultivated. The 2011 National Land Cover Database suggested that, within the twelve Great Plains states, an estimated 11.6 million ha of plains and grassland are under shrubs or herbs, unprotected, and at a 6° to 25° slope[40]. Currently, these areas are primarily used for cattle grazing. A sustainable expansion of wheat production to these steep grasslands and uneven terrain would almost double the land area used for this crop from 4% of the region to 7%. However, the current equipment practices are not safe enough to cultivate the steep grassland and uneven terrain. Therefore, a small autonomous ground vehicle fleet is proposed to expand agriculture to uneven terrain and steep grassland.

Today's mobile robots or ground vehicles are well-positioned to tackle the numerous complex problems in agriculture, ranging from seeding to harvesting[25–31]. Multiple small ground vehicles working with coordination and optimized mission planning can finish work comparable to large machines with improved safety[32] and reduced soil compaction[33]. Unlike heavy machines, the AGV can operate on relatively wet soil without damaging the soil, and even when one AGV becomes inoperative, the others could finish the operation. Moreover, a relatively small AGV (< 1m) is best suited for crop scouting and target-specific input application, an essential component of precision agriculture technology[34]. An AGV fleet has a significant potential to increase food production, lower production costs, and replace labor shortages[26;35].

The success of an AGV fleet operating on sloping terrain requires an efficient control algorithm and path planning that optimizes multiple objectives ranging from AGV operational variables, traction, time, energy efficiency, estimating its physical limits, safe operation, and limiting negative soil impacts. Hence, the AGV traction, mobility, and power consumption models for a continuously varying sloping environment are essential. On sloping terrain, multiple variables affect the ability of an off-road vehicle to perform its intended function. These variables include vehicle velocity, applied drawbar force to push or pull implements, slope magnitude, and AGV direction (ascending, descending, or sideways, i.e. parallel to an elevation contour)[107;118]. The AGVs have to negotiate steep terrain while pushing or pulling an external load, which demands traction capacity in addition to self-propulsion power. A loss of traction is measured by slip, which is inherently present when AGVs operate on any soil terrain[50;144]. The AGV's forward progress with optimum slip is desirable and acceptable; however, higher slip is undesirable as it causes power losses and often immobilizes the vehicle. Therefore, the traction performance of an AGV is of special importance to measure the vehicle traction efficiency and mobility. Tractive efficiency is a ratio of an AGV's output power to input power. The AGV power consumption is vital for optimizing vehicle autonomy and mission completion[145]. The AGV's operating conditions (e.g., speed, applied load, and skid steering) and terrain conditions (e.g., slope or grade, terrain properties) significantly influence the power consumption. A drawbar pull test is a standard procedure employed in off-road vehicle testing, which quantifies vehicle traction, mobility, and power consumption characteristics on particular terrain[50;71].

The first goal of this study was to generate data space on AGV traction, mobility, and energy consumption on sloping terrain. Thus, an AGV's drawbar pull test was conducted on actual sloping terrain. The second goal was to develop a machine learning-based traction, mobility, and energy consumption model for AGV's from the experimental data space. These models would predict specific dynamic responses, including traction, slippage, and energy from inputs on vehicle velocity, applied load, and slope.

In recent years, machine learning algorithms have been widely used to model the complex terrain-vehicle interaction in agricultural and planetary exploration vehicles. The lunar or planetary exploration rovers, including ground vehicles or mobile robots, must explore new territory without getting immobilized or entrapped[144;146]. Therefore, slip estimation and immobilization detection become crucial for exploration mission success. Gonzalez et. al., (2018)[147] employed proprioceptive sensor data to build machine learning models detecting slip and immobilization of an exploration rover. Their results demonstrated that machine learning models were highly accurate and relatively fast (i.e., lower computation time). Gonzalez et. al., (2019)[148] compared the eleven most popular machine learning (e.g., supervised and unsupervised) algorithms, to predict the rover's individual wheel slip (discrete classes) from motor torque, pitch rate, linear and vertical acceleration data. They identified the best machine learning model and the potential difficulties for machine learning models to catch data variability emerging from either slip or due to noise, particularly at slower speeds where the signal-to-noise ratio was very small.

Unlike exploration vehicles, agricultural vehicles are required to traverse a desired terrain or field with sufficient drawbar to push or pull the implements. Therefore, estimating slip and traction force are prime requirements. There is abundant evidence suggesting the application of machine learning algorithms such as neural networks (NN) to predict tire tractive performance[149], shallow NN to predict wheel traction force in soil bin[123], support vector machine, and NN to model tractive performance of radial tractor tires[106], NN to model the tractor performance as a function of its operational variables[125] and NN to model traction behaviors of AGV on controlled soil bin setup[150]. In most of these studies, shallow NN was frequently implemented and identified as a fast, accurate, robust and reliable tool to model vehicle-terrain interaction. However, most of these studies were conducted either on large agricultural tractors or on single traction elements (e.g., wheel), and tested in controlled laboratory setups or in flat field conditions. Very little information was available on small ground vehicle operation on a continuously varying sloping terrain and its traction, mobility, and energy consumption models.

This study will explore the capabilities of machine learning algorithms to accurately model the behavior of small track ground vehicles in an actual sloping terrain environment.

The developed vehicle mobility models would empower the entire AGV system operation by assisting path planning route optimization and delivering the control algorithm for fleets operation.

4.3 AGV's performance test

Drawbar pull test evaluated the AGV's traction capacity (essential to push or pull farming implements) in addition to propulsion power on desired terrain conditions. The drawbar pull test procedure involved operating the AGV on a fixed velocity and resisting its forward motion with external force through a towing hitch. The applied external force was known as drawbar pull which influenced the vehicle slip, and with sufficient drawbar pull, vehicle forward progress can be stopped. The magnitude of drawbar pull determined the type of implements attached and the nature of agricultural operation AGVs can perform on sloping terrain without getting immobilized. Hence, testing a complete range of drawbar pull from zero to maximum was appropriate. Additionally, the terrain slope also affects the drawbar pull performance of the vehicle because the cost of going uphill and downhill will not be the same. Thus, conducting the AGV drawbar pull performance on a continuously varying slope environment was essential.

4.3.1 AGV

A continuous-track type ground vehicle developed by 2050 Research Lab, Kansas State University (Kansas, U.S.), was used in this study (Figure 4.1). The skid-steered prototype vehicle was designed specifically to operate on steep slopes up to 25^0. The mass of the vehicle was 102 kg. The dimensions of the AGV were 1.16 m (length)$\times$ 0.64 m (width) $\times$ 0.55 m (height) and easily accommodated between row crop (0.76 m wide). The AGV was fitted with an onboard micro-controller and the necessary proprioceptive sensor package for teleoperation. The vehicle was powered with a 24V and 50Ah Lithium battery, sufficient for 3 -4 hours of continuous operation.

Figure 4.1: *AGV drawbar pull test on real field conditions (sloping terrain)*

Table 4.1: *Sensor package used in AGV instrumentation setup*

Measurement metrics	Sensor	Manufacture	Specification	Accuracy
Power consumption	Amperage sensor	Gravity series, Dfrobot, Shanghai, China	±20A DC	±1%
	Voltage sensor	Precision voltage sensor, Phidgets Inc., Calgary, Canada	±30 V DC	±2%
Track velocity (reference velocity)	Quadrature encoder	Encoder products Co., Sagle, Idaho, USA	4000 (cycles/revolution)	0.6 arc minutes
Ground truth velocity (actual velocity)	Quadrature encoder	Encoder products Co., Sagle, Idaho, USA	4000 (cycles/revolution)	0.6 arc minutes
Drawbar pull	Load cell	H.T. Sensor Technology Co., Ltd, Xi'an, China	200 kg	±0.02%
Slope inclination	Accelerometer	myRio, National Instruments, Austin, Texas, USA	±8 g	12 bits

4.3.2 Instrumentation setup

The AGV's instrumentation setup was established to measure its power consumption, each track velocity (actual and reference velocity), drawbar, and slope inclination on longitudinal (X-plane), lateral (Y-plane), and vertical (Z-plane) axes. The details of the sensor used in this study were presented in Table 4.1. The AGV was a skid steer, so, the reference velocity and actual velocity of each track was recorded independently. A pre-calibrated load cell was fitted on the AGV's drawbar hitch point to record the drawbar pull. The onboard micro-controller myRio recorded the X, Y, and Z accelerometer data. The data from each sensor (Table 4.1) were time-stamped and recorded at 10 Hz.

4.3.3 Experimental setup

The test was performed on real field conditions where the slope of the terrain was continuously varying. The selected test site was located at CiCo Park (GPS coordinates: 39.20, -96.62) in Manhattan, Kansas. The test site offered a maximum slope of 30°, and the grass was mowed regularly. The soil properties influenced the traction behavior of off-road vehicles and were often mentioned in traction studies or reports. Therefore, the cone penetration readings and soil samples were taken randomly with a cone penetrometer and soil sampling kit. A total of 15 samples were taken on the test area. The terrain properties such as cone index, cone index gradient, bulk density, and moisture content (dry basis) were recorded. The observed cone index, cone index gradient, bulk density, and moisture content were 1079.9±294.9 kPa, 7.2±1.9 kPa/mm, 1.4±0.1 g/cm^3 and 25.7±2.2 %, respectively. The soil properties described the test site where the AGV was tested and will not be mentioned further.

A rideable cart with brakes was used to apply the drawbar pull on the AGV. Hereafter, the rideable cart will be referred to as a drawbar cart. The AGV towed the drawbar cart with the help of a steel chain, which was attached to the AGV's drawbar hitch. The load cell was placed between the steel chain and drawbar hitch to measure the pulling load. The operator rode the drawbar cart and controlled its steering and brakes.

4.3.4 Test procedure

The field tests were performed in September 2021. The AGV was operated remotely and traversed the entire terrain. The vehicle run included uphill, downhill, sideways, and turning maneuvers. The AGV was operated on varying velocities covering the entire velocity range (2 to 10 m/min) of the AGV. Initially, the AGV pulled the drawbar cart for a few meters. Then the operator gradually applied the drawbar cart brakes to increase the magnitude of drawbar pull until the AGV was immobilized (i.e., tracks started slipping in place, 100% slip). Once the AGV was immobilized, the drawbar carts brakes were released, and after a few meters of travel, the AGV's travel velocity was varied by the operator to cover the entire velocity range. The above process was repeated while traversing the terrain. During the test, the data from a load cell, encoders, voltage amperage, and accelerometer were time-stamped, recorded, and stored in an external thumb drive (32 gigabytes) attached to a micro-controller. The drawbar pull test procedure was shown in Figure 4.1.

4.3.5 Data prepossessing

The collected sensor data were used for computing the predictor and response variables in Table 4.2. The calibrated load cell recorded the drawbar force (F_{DP}). The track velocities (reference velocity, V_{ref}) and actual track velocity (ground truth velocity, V_a) were computed from the track and ground truth encoder data. The slope values were obtained from the accelerometer data, and detailed equations can be found here[151]. The vehicle power (P) was obtained from the amperage and voltage sensor data. The tractive efficiency represented the AGV's ability to convert electrical energy from batteries to drawbar power and was defined as follows:

$$TE = \frac{F_{\mathrm{DP}} \times V_a}{P} \tag{4.1}$$

The travel reduction (TR), also known as slip, was computed with Equation 4.2. The power number (PN) was the ratio of vehicle power to the AGV's weight (W). Actual velocity (V_a) and was defined with Equation 4.3. The travel reduction measures the travel efficiency of the AGV, and the power number calculated the cost of mobility.

$$TR = 1 - \frac{V_a}{v_{\mathrm{ref}}} \tag{4.2}$$

$$PN = \frac{P}{W \times V_a} \tag{4.3}$$

The power number for the electric vehicle ranges from 1 to infinity. The relatively higher power number indicated that the AGV's track was 100% slipping without any forward progress, but the AGV was still consuming the power. The most desirable and efficient AGV operation resulted in a PN range of 4 to 10. We preferred to operate the AGV to a maximum PN value of 25. Therefore, all samples with PN$\geq$ 100 were discarded from the dataset since operating the AGV above this number becomes an inefficient operation. The number of remaining sample points was N = 69042, consisting of 6 input fields and 4 output fields. The inputs and outputs were the predictors and the responses, as shown in Table 4.2. Each input field was normalized separately to lie in the interval [0, 1] as shown below,

Table 4.2: *Variables under the study*

Predictor	Response
Drawbar pull force, N	Tractive efficiency (TE)
Right track velocity, m/s	Travel reduction of the left track (TR_L)
Left track velocity, m/s	Travel reduction of the right track (TR_R)
Slope in the X plane	Power number (PN)
Slope in the Y plane	
Slope in the Z plane	

$$x_i^d = \frac{\hat{x}_i^d - \min\limits_i \hat{x}_i^d}{\max\limits_i \hat{x}_i^d - \min\limits_i \hat{x}_i^d} \tag{4.4a}$$

$$y_i^d = \frac{\hat{y}_i^d - \min\limits_i \hat{y}_i^d}{\max\limits_i \hat{y}_i^d - \min\limits_i \hat{y}_i^d} \tag{4.4b}$$

In the above, $\hat{x}_i^d$ denoted a raw scalar input, where $i = 1, ..., N$ was the sample index and $d = 1, ..., 6$ was an input field. The corresponding normalized quantity was x_i^d. The output fields were normalized in the same manner shown above with $\hat{y}_i^d$ and y_i^d being the raw and normalized outputs. Note that as there were only four outputs, the field index $d \in \{1, ..., 4\}$, corresponded to the responses TE, TR_L, TR_R, and PN.

The inputs and outputs were optionally subjected to a noise removal procedure to reduce the amount of random noise that was present. Each field was convolved separately using a Gaussian filter $\mathbf{g} = [g_1 ... g_{2L+1}]$ (where $L = 20$ was the number of relevant time instances from the peak) shown in Figure 4.2. The area under the curve (shaded grey in Figure 4.2) was unity.

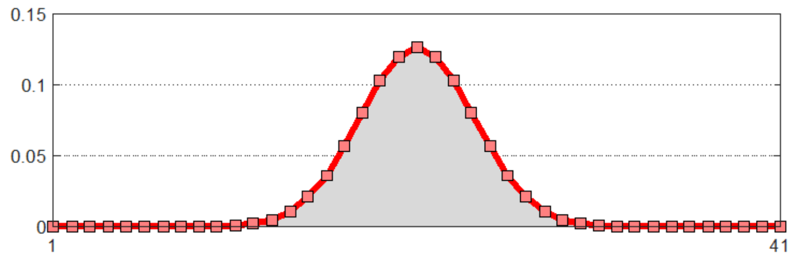

Figure 4.2: *Gaussian filter for noise reduction*

Therefore,

$$x_i^d = \sum_{j=-L}^{L} g_{j+L+1} x_{i-j}^d \tag{4.5}$$

The analogous expression for applying the convolution to each output field can be inferred readily and was not shown.

The task of estimating each output was considered separately. For simplicity, the index d in the outputs was ignored in the following description, as it was evident from the context. Accordingly, the i^{th} sample in the data were a pair $(\mathbf{x}_i, y_i)$ consisting of a six-dimensional input vector $\mathbf{x}_i = [x_i^1\ x_i^2\ x_i^3\ x_i^4\ x_i^5\ x_i^6]$ and an output scalar y_i(which could be any of TE, TR_L, TR_R, or PN).

Initial experiments showed that estimating y from an unknown input $\mathbf{x}$ was a complex regression problem. Hence, a model was specially developed for this research.

4.4 Proposed Model

The core assumption was the presence of K latent statistical processes that determined the response. The probability that process k, $k \in \{1, ..., K\}$ was used to determine response y from $\mathbf{x}$ was represented as $\mathrm{Pr}^{(k)}(\mathbf{x})$. Each process k was associated with a six-dimensional mean vector $\mu^{(k)}$ and a symmetric, positive semidefinite 6×6 covariance matrix $\mathbf{\Lambda}^{(k)}$. It must be noted that these processes, which was hereafter be referred to collectively as a Gaussian mixture, did not have any physical counterparts. The theoretical rationale behind the proposed approach was that such a mixture of Gaussians can approximate an arbitrary probability distribution to any desired degree of accuracy [152].

The inherent nonlinearities in the Gaussian mixture were modeled using DNNs. Thus, if $\mathbf{w}^{(k)}$ denoted the set of all weights of DNN k, the associated process k can be fully parameterized in terms of the 3-tuple $\left(\mu^{(k)}, \mathbf{\Lambda}^{(k)}, \mathbf{w}^{(k)}\right)$. Training the proposed model involved iteratively updating the 3-tuple of parameters for each index $k \in \{1, ..., K\}$. The quantity $\widetilde{y}^{(k)}$, which represented the output of DNN k, can be treated as a nonlinear function as indicated below,

$$\widetilde{y}^{(k)} = f_{NN}\left(\mathbf{x}; \mathbf{w}^{(k)}\right) \tag{4.6}$$

The subscript NN was task-dependent, so that $NN \in \{TE,\ TR_L, TR_R, PN\}$.

There were two underlying hypotheses behind the proposed approach, which were as follows: (i) the probability that process k generated response varies inversely with the Mahalanobis distance $\|\mathbf{x} - \mu^{(k)}\|_{\mathbf{\Lambda}^{(k)}}$between $\mathbf{x}$ and the process mean $\mu^{(k)}$; (ii) the probability that process k generated response y bear an inverse relationship with the difference between the true response y and its estimate $\widetilde{y}^{(k)}$. Accordingly, the expression for the probability $\mathrm{Pr}^{(k)}(\mathbf{x})$ shown below contained a factor corresponding to each hypothesis,

$$\mathrm{Pr}^{(k)}(\mathbf{x}) = \frac{1}{Z}\Psi\left(\mathbf{x}|\mu^{(k)}, \mathbf{\Lambda}^{(k)}\right)\Phi\left(\widetilde{y}^{(k)}|y, \mathbf{w}^{(k)}\right) \tag{4.7}$$

The denominator Z was used for normalization so that,

$$\sum_{k=1}^{K} \mathrm{Pr}^{(k)}(\mathbf{x}) = 1 \tag{4.8}$$

The functions $\Psi(\cdot)$ and $\Phi(\cdot)$ in Eqn. (4.4) were given by,

$$\Psi\left(\mathbf{x}|\mu^{(k)}, \mathbf{\Lambda}^{(k)}\right) = e^{-\frac{\beta}{\tau}\left(\mathbf{x}-\mu^{(k)}\right)^T \mathbf{\Lambda}^{(k)-1}\left(\mathbf{x}-\mu^{(k)}\right)} \tag{4.9}$$

$$\Phi\left(\widetilde{y}^{(k)}|y, \mathbf{w}^{(k)}\right) = e^{-\frac{1-\beta}{\tau}\left(\widetilde{y}^{(k)}-y\right)^2} \tag{4.10}$$

There were two parameters in Eqns. (4.7), (4.9) and (4.10), τ and β. While τ can be assigned any positive value, β must lie between zero and unity (i.e., $\tau \in (0,\ \infty)$ and

$\beta \in [0,\ 1]$). During actual deployment, the model was applied to provide an estimate $\widetilde{y}$ of the true response y, from an arbitrary input $\mathbf{x}$. Since the true response y was unknown, the value of β was set to unity so that $\Phi\left(\widetilde{y}^{(k)}|y, \mathbf{w}^{(k)}\right) = 1$, in which case the probability was dependent on $\Psi\left(\mathbf{x}|\mu^{(k)}, \mathbf{\Lambda}^{(k)}\right)$ which did not require y. On the other hand, when training the model using training samples $(\mathbf{x}, y)$, β can acquire a nonzero value in the interval $[0,\ 1]$.

The role of the other parameter τ in the above expression can be understood by considering its limiting cases. When $\tau \to \infty$ it was clear that $\mathrm{Pr}^{(k)}(\mathbf{x}) \to K^{-1}$. This pertained to the naïve assumption that all K Gaussians had equal probabilities. On the other hand, $\tau \to 0$ produced the maximum likelihood situation where the process with the highest probability was the one that generated the output.

The estimated response $\widetilde{y}$ was computed from the DNN outputs $\widetilde{y}^{(k)}$ as,

$$\widetilde{y} = \sum_{k=1}^{K} \mathrm{Pr}^{(k)}\left(\mathbf{x}\right)\widetilde{y}^{(k)} \tag{4.11}$$

Figure 4.3 showed the schematic of the present model and depicted all variables used in the model except Z, τ, and β. The pathways used during training (described next) were shown using dashed lines; the rest were in solid lines. The product, summation, and exponentiation operators were shown as circles, diamonds, and squares. For simplicity, the squaring operator was not depicted. In all results reported here, estimates $\widetilde{y}$ were obtained with $\beta = 1$ and $\tau = 1$.

4.4.1 Training Algorithm

The training algorithm, which involved iterative updates of all parameters of the model – $\left(\mu^{(k)}, \mathbf{\Lambda}^{(k)}, \mathbf{w}^{(k)}\right)$, $k \in \{1, ..., K\}$, was implemented in MATLAB. Training the DNN weights $\mathbf{w}^{(k)}$ was carried out using the software package's Deep Learning toolbox, which offered a wide variety of built-in training algorithms and other features. Without going into the intricate details of the training algorithm, this section outlined only the main aspects of the training algorithm. For further details, the interested reader was referred to Goodfellow

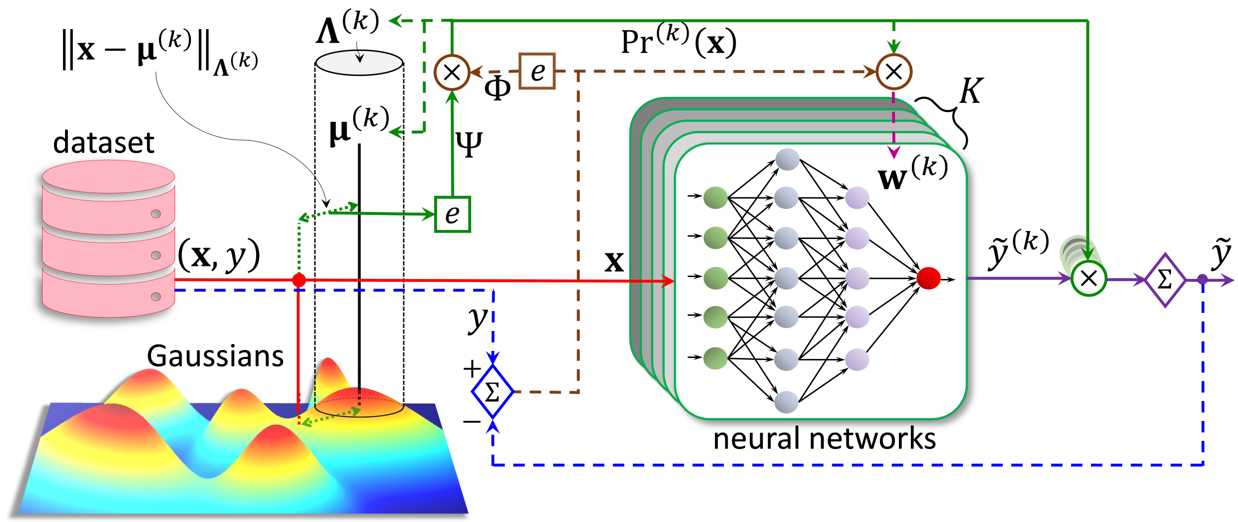

Figure 4.3: *Schematic of the proposed model. The dataset and the two components of the model (mixture of Gaussians and the deep neural networks) were shown. Solid lines depicted signal pathways involved in training and testing, whereas dotted lines pertain to training only*

et.al., (2016)[153].

Training the DNN weights $\mathbf{w}^{(k)}, k \in \{1, ..., K\}$, was based on minibatch gradient descent. In each iteration, the training samples were shuffled randomly and then divided into ten disjoint mini-batches of the same size. A gradient step was implemented using the sum squared error of all samples within the mini-batch. Suppose $\mathcal{B} \subset \{1, ..., N\}$ was one such mini-batch, the weight increment step can be expressed as,

$$\mathbf{w}^{(k-1)} \leftarrow \mathbf{w}^{(k)} - \frac{\eta}{2} \nabla_{\mathbf{w}^{(k)}} \sum_{i \in \mathcal{B}} \mathrm{Pr}^{(k)}(\mathbf{x}_i) \left(\widetilde{y}_i^{(k)} - y_i \right)^2 \tag{4.12}$$

The quantity η above, was the learning rate. The operator $\nabla_{\mathbf{w}}$ denoted the derivative with respect to $\mathbf{w}$. The actual training algorithm was carried out using ADAM, an extension of gradient descent that yielded faster training. Additionally, it involved regularization, which was used to prevent overtraining. For simplicity, the terms corresponding to ADAM and regularization were omitted in the above expression; for further details the reader was referred to Setoodeh et. al (2022)[154]. Dividing the dataset into separate training and test samples was carried out automatically by the toolbox.

The summation in Eqn (4.12) was the sum of the squared errors $\left(\widetilde{y}_i^{(k)} - y_i \right)^2$ of all samples in the minibatch, weighted according to the sample probabilities $\mathrm{Pr}^{(k)}(\mathbf{x}_i)$. This weighting scheme allowed the weights of DNN k to be updated in proportion to the probability that the output y_i was generated by the k^{th} Gaussian in the mixture model.

The means and covariance matrices were updated in the following manner,

$$\mu^{(k)} \leftarrow \sum_{i=1}^{N} \mathbf{x}_i \mathrm{Pr}^{(k)}(\mathbf{x}_i) \tag{4.13}$$

$$\mathbf{\Lambda}^{(k-1)} \leftarrow \sum_{i} \mathrm{Pr}^{(k)}(\mathbf{x}_i)\left(\mathbf{x}_i - \mu^{(k)}\right)\left(\mathbf{x}_i - \mu^{(k)}\right)^T \tag{4.14}$$

The above expressions were identical to those of the well-known expectation-maximization (EM) algorithm[155], an unsupervised learning algorithm that was widely used to train Gaussian mixture models. After initializing the means and covariances, the EM algorithm proceeded in an iterative manner. Each iteration of the algorithm consisted of an expectation step followed by a maximization step. In the expectation step, the probabilities $\mathrm{Pr}^{(k)}(\mathbf{x}_i)$ were computed using the Gaussian parameters $\mu^{(k)}$, $\mathbf{\Lambda}^{(k)}$, $k \in \{1, ..., K\}$ of the preceding iteration. The parameters were updated in the maximization step according to Eqns. (4.13) and (4.14).

A key difference between the EM algorithm and the present approach was the manner by which the probabilities $\mathrm{Pr}^{(k)}(\mathbf{x}_i)$ were determined in the expectation step. The EM algorithm computed the probabilities in a manner similar to that in Eqn. (4.7), but with $\Phi(\cdot)$ replaced with a set of K prior probabilities of the Gaussians. The priors were subjected to iterative updates using unsupervised learning in the maximization step. Therefore, the suggested approach may be regarded as a supervised extension of the EM algorithm. An important result of this study was that, whereas it was quite well established that the EM algorithm converged rather slowly, a maximum of 200 iterations was found to be large enough in the present case.

A small value $\beta \ll 1$ was used during training so that $\Phi(\cdot)$ was the dominant factor in determining $\mathrm{Pr}^{(k)}(\mathbf{x}_i)$. This was found to be suitable for faster training. The quantity τ was initialized to a very high value $\tau_\infty = 100$ so that $\mathrm{Pr}^{(k)}(\mathbf{x}_i) = K^{-1}$. In this manner, all DNNs were trained equally by each sample in the first iteration (the differences in their outputs $\widetilde{y}_i^{(k)}$ arising solely from the random initialization of their weights $\mathbf{w}^{(k)}$). In a manner akin to mean field annealing[156;157], τ was geometrically lowered at the end of every iteration by a factor $\gamma = 0.965$ so that each 3-tuple got increasingly trained based on the proximity of its own estimate $\widetilde{y}_i^{(k)}$ to the real response y_i.

4.5 Results and discussions

4.5.1 Performance metrics

Model performance was quantified using a set of four metrics, (i) the mean squared error E_2, (ii) the coefficient of determination R^2, (iii) the correlation coefficient C, and (iv) the slope of the regression line r. Letting $\bar{y}$ denoted the sample mean of all real responses and $\bar{\widetilde{y}}$, that of the corresponding estimates, the metrics were obtained according to the following expressions,

$$E_2 = N^{-1} \sum_i \left(y_i - \widetilde{y}_i\right)^2 \tag{4.15}$$

$$R^2 = 1 - \left(\sum_i \left(y_i - \widetilde{y}_i\right)^2 \right)^{-1} \sum_i \left(y_i - \bar{y}\right)^2 \tag{4.16}$$

$$C = \left(\sum_i \left(y_i - \bar{y}\right)^2 \sum_i \left(\widetilde{y}_i - \bar{\widetilde{y}}\right) \right)^{-\frac{1}{2}} \sum_i \left(y_i - \bar{y}\right) \left(\widetilde{y}_i - \bar{\widetilde{y}}\right) \tag{4.17}$$

$$r = \underset{r'}{\operatorname{argmin}} \sum_i \left(r' y_i - \widetilde{y}_i\right)^2 \tag{4.18}$$

The mean squared error E_2 can acquire any non-negative value, with lower values indicating better performance. The remaining metrics should be as close to unity as possible.

4.5.2 Regression models comparison for PN estimation

The first set of experiments was carried out to evaluate the performances of the most commonly used machine learning models with the data set, which were: (i) quadratic regression,

(ii) kernel regression, (iii) support vector regression, (iv) Gaussian process regression, and, (v) neural networks of various sizes.

All the models were evaluated for PN estimation. This task was found to be most suitable because the real PN values in our data set followed a very uneven distribution. Furthermore, the simplest model, quadratic regression, was picked to study the effectiveness of L_1 norm, L_2 norm, Hüber, and log Hüber loss functions. In particular, the Hüber and log Hüber losses were used to see if they were more effective in handling the unevenness.

Table 4.3 showed the performances of the regression models. Since the quadratic model did not involve any random initialization only a single trial was used. The results of a total of 20 trials was obtained for all other models and the one with the least E_2 was selected for representation. It was evident from the Table 4.3 that neural networks outperformed the others by significant margins. Moreover, deeper networks with more neurons were found to perform better. The best performing one was the 6×20×10×7×1 DNN. Despite its relatively large network size, the copious amount of data helped prevent overtraining, which would have resulted in performance degradation vis-à-vis test samples. This network's performance was only marginally better that those of the 6×13×7×3×1 DNN. However, the latter was selected for further analysis because its faster training was considered to be an effective trade-off for the relatively small reduction in performance. Moreover, of the 20 trials, the best performing 6×13×7×3×1 DNN had a lower value of E_2 than 85% of trials of the 6×20×7×3×1 DNN and 65% of those of the 6×20×10×7×1 network. The figures (Table 4.3) also showed that there was no clear benefit of using more complex Hüber loss or its logarithm. Wherever relevant, the other models were trained using the L_2 norm function (which was equal to $\sqrt{NE_2}$).

4.5.3 Deep neural network comparison

The next set of experiments was carried out to assess potential improvements in simultaneously training K DNNs and then using them for estimation. In addition to the proposed approach (Section 4.4), where the samples were weighted probabilistically using the DNN

Table 4.3: *Comparison of several regression models for PN estimation*

Model	Loss/Size	Trials	Performance Metric			
			E_2	R^2	C	r
Quadratic Regression	L_1 loss	-	5.3312	0.0753	0.3184	0.3198
	L_2 loss	-	5.5125	0.1454	0.3813	0.4247
	Hüber loss	-	5.1698	0.1304	0.3734	0.3785
	log Hüber loss	-	5.2521	0.1025	0.3551	0.523
Kernel Regression	-	20	5.2225	0.1126	0.3725	0.3434
Support Vector Regression	-	20	5.1515	0.1366	0.4138	0.3538
Gaussian Process Regression	-	20	4.2836	0.402	0.6352	0.6048
Neural networks	6×16×1	20	4.2032	0.4252	0.6521	0.6118
	6×13×3×1	20	3.4245	0.6184	0.7864	0.7382
	6×13×7×1	20	3.3745	0.6295	0.7935	0.7593
	6×13×7×3×1	20	2.7804	0.7485	0.8652	0.8303
	6×20×7×3×1	20	2.6096	0.7784	0.8823	0.8516
	6×20×10×7×1	20	2.5929	0.7813	0.8839	0.8579

with the mixture of K Gaussians, training the K DNNs with all training samples without prior probability weights was also taken up in this study. Here, the estimate $\widetilde{y}$ was obtained as,

$$\widetilde{y} = \frac{1}{K} \sum_{k=1}^{K} (\mathbf{x})\, \widetilde{y}^{(k)} \tag{4.19}$$

This will be referred to as the average-of-K-DNNs. It was shown in the Appendix that with test data, the average-of-K-DNNs performed better than the single best DNN.

Lastly, response estimation with a single DNN was also considered. Whereas 20 trials of each of the proposed models as well as of the average-of-K-DNNs were obtained, for fair comparison, the best performance out of a total of $K \times 20$ trials of the single DNN was considered.

The results of this study were shown in Table 4.5. The proposed approach yielded the best performance with $K = 6$, indicating the advantage of using Gaussian mixtures with the DNNs. Table 4.4 reported the performances of the proposed model with only $K = 4$ DNNs; which performed better that the average-of-K-DNNs with $K = 6$. Furthermore, average-of-

Table 4.4: *Comparison of deep neural networks for PN estimation*

Model	K	Trials	Performance Metric			
			E_2	R^2	C	r
DNN	K=1	120	2.7656	0.7511	0.8667	0.8322
Avg. DNN	K=6	20	2.7384	0.7560	0.8764	0.7789
Proposed	K=4	20	2.5936	0.7811	0.8848	0.8321
	K=6	20	**2.5573**	**0.7872**	**0.8876**	**0.8494**

Table 4.5: *Comparison of deep neural networks for TE, TR_L, and TR_R estimation*

Model	Response	Performance Metric			
		E_2	R^2	C	r
Avg. DNN	TR_L	0.1157	0.5692	0.7589	0.7155
Proposed		**0.1139**	**0.5825**	**0.7647**	**0.7540**
Avg. DNN	TR_R	0.1087	0.6116	0.7856	0.7413
Proposed		**0.1073**	**0.6213**	**0.7893**	**0.7785**
Avg. DNN	TE	0.0224	0.8826	0.9396	0.9753
Proposed		**0.0221**	**0.8858**	**0.9414**	**0.9787**

K-DNNs showed improved performance over using a single DNN. Although counter-intuitive, a brief explanation of this phenomenon was provided in the Appendix 4.6. It should be noted that in each trial, the DNNs in the proposed model and to maintained fairness, in the average-of-K-DNNs were initialized to the same random initial weights per trial.

Next, the proposed approach as well as the average-of-K-DNNs were investigated further for the tasks of estimating the other responses, TR_L, TR_R, and TE. As can be observed in Table 4.5, in all these tasks, the proposed approach outperformed the average-of-K-DNNs. We believe that the results provided enough empirical evidence to establish the advantage of using the proposed model.

4.5.4 Effect of noise reduction

From Tables 4.4 and 4.5, it can be seen that the performance of the proposed approach was satisfactory for PN and TE estimation in terms of R^2, C and r, unlike those for TR_L

Table 4.6: *Comparison of DNN for TR_L and TR_R estimation after noise reduction*

Model	Response	Performance Metric			
		E_2	R^2	C	r
Avg. DNN	TR_L	0.0936	0.6703	0.8240	0.7824
Proposed		**0.0910**	**0.6884**	**0.8313**	**0.8318**
Avg. DNN	TR_R	0.0894	0.6971	0.8380	0.8029
Proposed		**0.0610**	**0.7132**	**0.8456**	**0.8387**

and TR_R estimates. Further analysis revealed that the primary cause was the presence of a significant amount of noise in the dataset, particularly for TR.

Hence, a final set of experiments were performed to investigate if noise reduction by convolving the raw input and output signals with a Gaussian helped improve the model performance. The outcome of this investigation was provided in Table 4.6. In comparison to the performance metrics in Table 4.5, it was clear that those in Table 4.6 showed marked improvements.

Figure 4.4 showed scatter plots of the real values of all sample outputs y_i in the data (x-axis) and their estimates $\widetilde{y}_i$ (y-axis) using the proposed approach to estimate PN (top), TE (upper middle), TR_L (lower middle), and TR_R (bottom). Regression lines intersecting the origin and with slopes equal to r was also shown in the Figure.

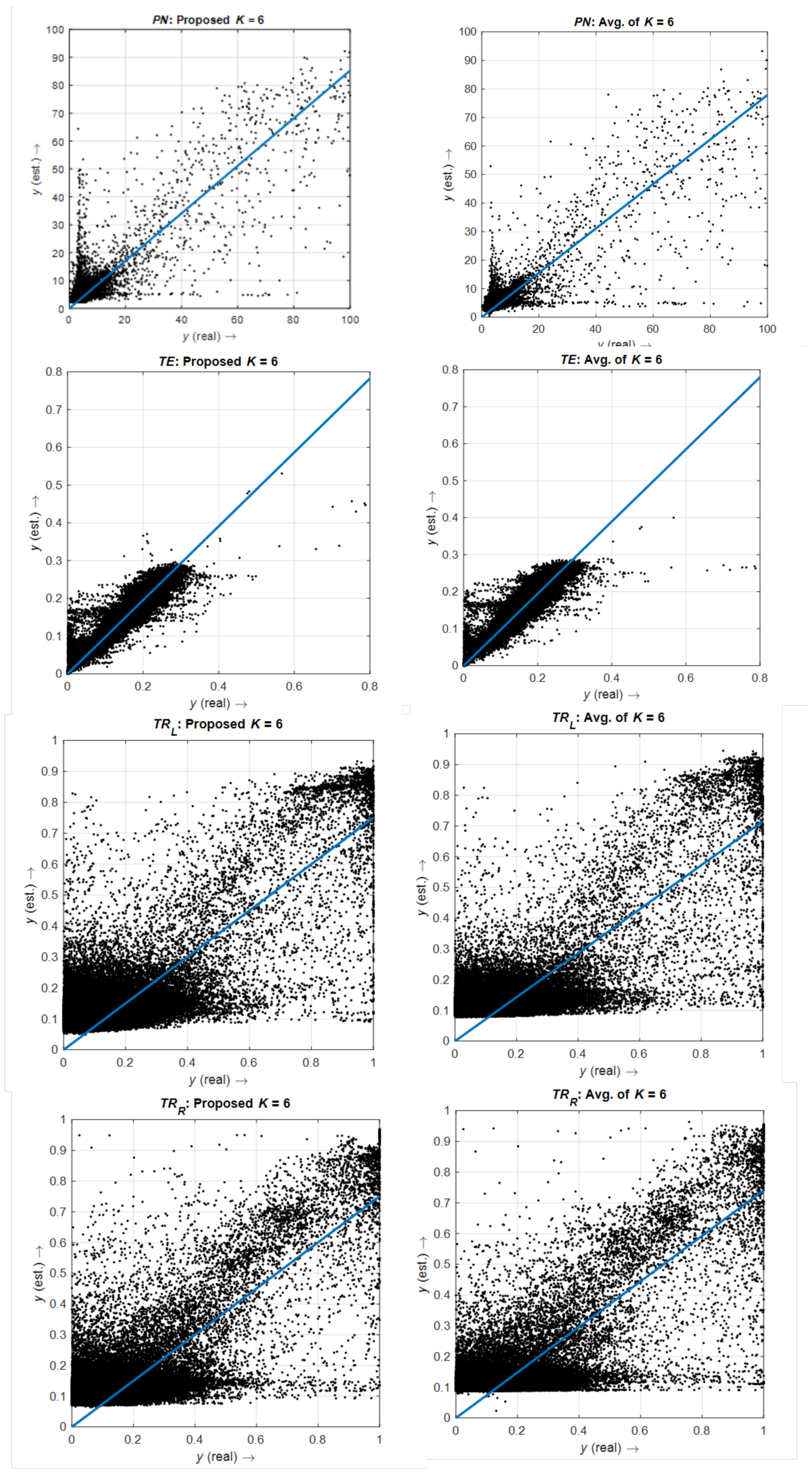

Figure 4.4: *Scatter plots of best out of 20 trials of the proposed approach (left) and average-of-K-DNNs (right) with K=6 (real output on the x-axis; estimated output on the y-axis)*

4.5.5 Discussion

The results discussed above showed that the proposed model consistently outperformed other approaches in predicting all four AGV responses. The authors attribute the superior performance of the proposed approach to localization. The Gaussian mixtures break up the six-dimensional input space into a set of K hyperellipsoidal domains. When an input was outside the domain of a Gaussian, the associated DNN did not play any tangible role in estimating the corresponding response. To simplify this discussion, let us introduce a (vanishingly) small quantity δ such that a point was considered to lie within a Gaussian if it was within a Mahalonobis radius of δ. In effect, δ established well-defined boundaries for each domain.

It was a common hypothesis in machine learning that data clouds were distributed within a lower dimensional manifold of the Euclidean input space. Localization divided the manifold into smaller domains with lower curvatures than that of the manifold. As each DNN specialized on points within its own domain, it was no longer encumbered with the task of handling an input space that was more pronouncedly "curved" [157]. Initialized with random weights, the proposed training algorithm allowed the DNNs to gradually migrate towards the domains that they were best equipped to handle.

Although the simulation results reported earlier did not show this, preliminary experiments suggested that, despite the computational overhead associated with the mixture of Gaussians, the overall training time can be reduced in comparison to that when training K separate DNNs (as in the average-of-K method). Before a DDN subjected to a new round of training, those samples in the dataset that were outside its Mahalonobis radius can be removed from the set of samples. In this manner, the number of gradient steps can be significantly reduced. Further investigation was necessary to corroborate this claim, which will be done in the future.

It must be noted that the proposed algorithm was best equipped to handle only low-dimensional datasets. Since the number of Gaussian needed to fully cover the input space increased exponentially with the latter's dimensionality, an input dimensionality above seven or eight would lead to a combinatorial explosion. Further investigation with other datasets must be performed to more firmly establish the algorithm's inherent limits.

The model proposed in this research was designed specifically with the present dataset, which had very unevenly distributed responses (especially in the power number). Its effectiveness with more evenly spaced, "simpler" datasets remains another task for future research.

Conclusions

In this study, the drawbar performance of an AGV was carried out in actual sloping field conditions at varying vehicle velocities and drawbar pull. The performance test quantified the AGV's traction, mobility, and energy consumption characteristics. The experimental data obtained in this test was employed and a new machine learning model was developed to predict the AGV's behavior in sloping terrain environments. The model was compared with other popular machine learning regression models, including quadratic regression, kernel regression, support vector regression, Gaussian process regression, and deep neural networks. The following conclusions can be drawn from the study.

- Deep neural networks were particularly well-suited for predicting AGV behavior, in terms of the mean squared error, coefficient of determination, correlation coefficient, and linear regression.

- Data localization using Gaussian mixtures was an effective strategy when dealing with experimental data that were characterized by manifolds with high curvatures, such as in AGV behavior.

- The proposed approach of incorporating DNN training steps within a broader supervised EM framework was able to perform training within a relatively small number of iterations, comparable to that of a single DNN.

- The study explored the capabilities of machine learning algorithms to simulate the

AGV's behavior on sloping terrain. The noisy real-world data made it difficult for the machine learning model to learn, particularly for the travel reduction ratio where the single to noise ratio was high.

- The AGV traction, mobility, and energy consumption models would empower the entire AGV system operation in sloping terrain.

4.6 Apendix A

It can be shown that the mean squared error of the average-of-K DNNs was lower than that of the best-of-K (independently trained) DNNs, i.e.,

$$E_2^{avg} < E_2^{best}$$

Proof: Let $\mathbf{y}$ and $\widetilde{\mathbf{y}}^{(k)}$ be the N×1 vectors of real values and the estimates of DNN k. Also let the N× K matrix of estimates produced by K independently trained DNNs be denoted as $\widetilde{\mathbf{Y}}$ so that,

$$\widetilde{\mathbf{Y}} = \left[\widetilde{\mathbf{y}}^{(1)} \ldots\ \widetilde{\mathbf{y}}^{(K)}\right]$$

The estimates of the average-of-K DNNs and the best-of-K DNNs are given as,

$$\widetilde{\mathbf{y}}^{avg} = \widetilde{\mathbf{Y}}\mathbf{a}$$

$$\widetilde{\mathbf{y}}^{best} = \widetilde{\mathbf{Y}}\mathbf{b}$$

In the above expressions, $\mathbf{a}$ and $\mathbf{b}$ are two K×1 vectors of the DNN output weights whose $k^t h$ elements (i.e. the weight of the kth DNN's output) were defined as,

$$a_k \triangleq K^{-1},$$

$$b_k \triangleq \begin{cases} 1, & k = \underset{r'}{\operatorname{argmin}} E_2^{(k')} \\ 0, & otherwise \end{cases}$$

The mean squared error of the average-of-K DNNs was,

$$E_2^{avg} = N^{-1} \|\widetilde{\mathbf{y}}^{avg} - y\|_2^2$$

$$E_2^{avg} = N^{-1} \left(\widetilde{\mathbf{Y}}\mathbf{a} - \mathbf{y}\right)^T \left(\widetilde{\mathbf{Y}}\mathbf{a} - \mathbf{y}\right)$$

$$E_2^{avg} = N^{-1}\left(\mathbf{a}^T\widetilde{\mathbf{Y}}^T\widetilde{\mathbf{Y}}\mathbf{a} - 2\mathbf{y}^T\widetilde{\mathbf{Y}}\mathbf{a} + \mathbf{y}^T\mathbf{y}\right)$$

Whence,

$$E_2^{avg} = \frac{1}{2}\mathbf{a}^T\mathbf{Q}\mathbf{a} - \mathbf{p}^T\mathbf{a} + r$$

Similarly, the mean squared error of the best-of-K DNNs was,

$$E_2^{best} = \frac{1}{2}\mathbf{b}^T\mathbf{Q}\mathbf{b} - \mathbf{p}^T\mathbf{a} + r$$

The three quantities, $\mathbf{Q}$, $\mathbf{p}$, and r were defined as,

$$\mathbf{Q} \triangleq 2N^{-1}\widetilde{\mathbf{Y}}^T\widetilde{\mathbf{Y}},$$

$$\mathbf{p} = 2N^{-1}\widetilde{\mathbf{Y}}^T\mathbf{y},$$

$$r = \mathbf{y}^T\mathbf{y}.$$

It can be seen that $\mathbf{Q}$ was symmetric and positive definite. Let $\mathbf{c}$ be the "optimal" weight vector that minimizes E_2, so that,

$$\mathbf{c} = \underset{x}{\operatorname{argmin}}\left(\frac{1}{2}\mathbf{x}^T\mathbf{Q}\mathbf{x} - \mathbf{p}^T\mathbf{x} + r\right) = \mathbf{Q}^{-1}\mathbf{p}.$$

At the end of the first training epoch of trial 1, the K=6 eigenvalues of $\mathbf{Q}$ were in the interval $[+0.0535,\ +3.6872]$ thereby verifying the positive definiteness of $\mathbf{Q}$. The distances of $\mathbf{a}$ and $\mathbf{b}$ from $\mathbf{c}$ were found to be $\|a-c\|_Q = 1.8168$, and $\|b-c\|_Q = 2.9047$ indicating that $\mathbf{b}$ lay further away than did $\mathbf{a}$ from the global minimum of E_2. The numerical values of the mean squared errors were found to be as follows, $E_2^{avg} = 0.0871$, and $E_2^{best} = 0.1087$.

Apendix B

Figure 4.5 showed the pseudocode of proposed supervised learning algorithm. For simplicity, it was assumed that the DNN weights ($\mathbf{w}^{(k)}$) were incremented only once per iteration of the outer loop. For comparison, pseudocode of the EM algorithm was provided in Figure 4.6.

for $k = 1$ **to** K — INITIALIZATION

  $\boldsymbol{\mu}^{(k)} \leftarrow$ **random**() $\boldsymbol{\Lambda}^{(k)} \leftarrow \mathbf{I}$ $\mathbf{w}^{(k)} \leftarrow$ **random**()

  converge $\leftarrow$ **false** $\tau \leftarrow \tau_\infty$

do while (*converge* == **false**)

  for $i = 1$ **to** N — EXPECTATION STEP

    for $k = 1$ **to** K

      $\tilde{y}_i^k \leftarrow f_{NN}(\mathbf{x}_i; \mathbf{w}^{(k)})$

      $\Pr^{(k)}(\mathbf{x}_i) \leftarrow Z^{-1} \cdot e^{-\frac{\beta}{\tau}(\mathbf{x}-\boldsymbol{\mu}^{(k)})^{\mathrm{T}}\boldsymbol{\Lambda}^{(k)^{-1}}(\mathbf{x}-\boldsymbol{\mu}^{(k)})} \cdot e^{-\frac{1-\beta}{\tau}(\tilde{y}_i^k - y_i)^2}$

  for $k = 1$ **to** K — MAXIMIZATION STEP

    $\mathbf{w}^{(k)} \leftarrow \mathbf{w}^{(k)} - \eta \nabla_{\mathbf{w}^{(k)}} \sum_i \Pr^{(k)}(\mathbf{x}_i) \mathcal{E}\left(\tilde{y}_i^{(k)}, y_i\right)$

    $\boldsymbol{\mu}^{(k)} \leftarrow \sum_i \mathbf{x}_i \Pr^{(k)}(\mathbf{x}_i)$

    $\boldsymbol{\Lambda}^{(k)} \leftarrow \sum_i \Pr^{(k)}(\mathbf{x}_i)(\mathbf{x}_i - \boldsymbol{\mu}^{(k)})(\mathbf{x}_i - \boldsymbol{\mu}^{(k)})^{\mathrm{T}}$

  $\tau \leftarrow \gamma\tau$ — "COOLING"

  converge $\leftarrow$ **convergence-criterion**() — CONVERGENCE CHECK

Figure 4.5: *Pseudocode of the proposed supervised learning approach.*

for $k = 1$ **to** K — INITIALIZATION

  $\boldsymbol{\mu}^{(k)} \leftarrow$ **random**() $\boldsymbol{\Lambda}^{(k)} \leftarrow \mathbf{I}$ $\pi^{(k)} \leftarrow K^{-1}$

  converge $\leftarrow$ **false**

do while (*converge* == **false**)

  for $i = 1$ **to** N — EXPECTATION STEP

    for $k = 1$ **to** K

      $\Pr^{(k)}(\mathbf{x}_i) \leftarrow Z^{-1} \cdot e^{-\alpha(\mathbf{x}-\boldsymbol{\mu}^{(k)})^{\mathrm{T}}\boldsymbol{\Lambda}^{(k)^{-1}}(\mathbf{x}-\boldsymbol{\mu}^{(k)})} \cdot \pi^{(k)}$

  for $k = 1$ **to** K — MAXIMIZATION STEP

    $\pi^{(k)} \leftarrow \sum_i \Pr^{(k)}(\mathbf{x}_i)$

    $\boldsymbol{\mu}^{(k)} \leftarrow \sum_i \mathbf{x}_i \Pr^{(k)}(\mathbf{x}_i)$

    $\boldsymbol{\Lambda}^{(k)} \leftarrow \sum_i \Pr^{(k)}(\mathbf{x}_i)(\mathbf{x}_i - \boldsymbol{\mu}^{(k)})(\mathbf{x}_i - \boldsymbol{\mu}^{(k)})^{\mathrm{T}}$

  converge $\leftarrow$ **convergence-criterion**() — CONVERGENCE CHECK

Figure 4.6: *Pseudocode for expectation-maximization.*

Chapter 5

Design, fabrication & experimental investigation of screw auger type feed mechanism for a robotic wheat drill[1]

5.1 Abstract

Cultivating the arable, highly sloped hills and uneven terrain is challenging and unsafe with large agricultural machines. Therefore, a fleet of small Autonomous Ground Vehicles (AGV) was proposed to farm sloped or uneven terrain. The fleets need a robotic grain drill operating on varying slopes, and the success of the fleet depends on the performance of the robotic seeder or grain drill. The feed mechanism is the heart of the seeder, and its design and performance influence the plant population and crop yield. In this study, an auger-type feed mechanism was designed and fabricated for robotic wheat drilling. Feed mechanisms with augers having three different pitches were developed as per the ASABE standards. The developed feed mechanism was investigated in a laboratory setup for flow rate and flow uniformity in accordance with ISO standards. The predictor variables were auger type (pitch), auger rotational speed, vibration, and slope. The auger flow rate for flat slope was a linear function of auger speed and varied from 30 g/min to 170 g/min. The coefficient

[1]Results published as a peer-review article. Badgujar, C., Wu, H., Flippo, D., & Brokesh, E. (2022) Design, Fabrication & Experimental Investigation of Screw Auger Type Feed Mechanism for a Robotic Wheat Drill. Journal of the ASABE. doi: 10.13031/ja.15199

of variation (CV) for flow rate ranged from 2 to 10%. The CV was within the acceptable limits, which was an excellent indicator of the bulk feed mechanism's flow uniformity. The feed mechanism performance was influenced by vibration and slope. However, the auger flow rate remained constant for vibration frequencies of 0, 6, and 14 Hz, suggesting that the feed mechanism was vibration-proof and can tolerate the vibration frequency up to 14 Hz. The flat, downhill (descending) , and uphill (ascending) slope levels did not affected the feed mechanism performance. However, the side slopes (right and left slope) significantly affected the feed mechanism flow rate but did not affect the flow uniformity. The study delivered a feed mechanism for a sloped-ground prototype seeder, which can be easily scaled and adopted by small autonomous vehicles or mobile robots.

5.2 Introduction

A continuously growing global population and escalating food, fiber, and fuel demands are the major drivers of agriculture cropland intensification and expansion to achieve global food security[87]. In cropland intensification, advanced tools and techniques improve crop resource use efficiencies to boost crop production on existing land[158]. In contrast, cropland expansion brings the new land under cultivation by either clearing grasslands, or, forests, or bringing unsuitable marginal land under cultivation. The pace of cropland expansion was accelerated in recent decades, and it was estimated that global cropland area was increased by 9%, that was 101.9 ± 45.1 Mha, between 2003-2019[159]. In the United States, the rate of cropland expansion was over 404.6 thousand ha per year between 2008 and 2016[160]. Some parts of the Great Plains (U.S.) have uncultivated rolling hills, steep grasslands, and uneven terrain often characterized as marginal land. The excessive steepness of marginalized grasslands, hills, and uneven terrain precludes crop cultivation with conventional agricultural equipment. Land steeper than 6° is challenging and unsafe to cultivate, and accidents involving large tractors killed over 120 farmers per year in the U.S., mainly from roll-overs[161]. Solving this technical impediment to slope farming could significantly expand the agricultural land to boost sustainable food production. It is estimated that a sustainable expansion of wheat production to these steep grasslands and uneven terrain would almost double the land area used for this crop from current 4% to 7% in the Great Plains region.

Mobile robots and small autonomous ground vehicles are being employed to perform repetitive agricultural tasks with human assistance/intervention and have the potential to become prime candidates for outdoor agriculture in the near future. Therefore, a fleet of small Autonomous Ground Vehicles (AGV) is proposed to drill wheat on the highly sloped grassland, hills, and uneven terrain[150]. The drilled wheat crop is for cattle grazing and will not be harvested for grain. A self-propelled robotic wheat drill (two rows & row spacing of 30.4 cm) dispersing the controlled amount of seeds on marginalized grasslands is the critical component of AGV fleet operation. The success of a AGV fleet largely depends upon the wheat drill performance. The feed mechanism is the heart of the grain drill, and its performance influences the optimum plant population and determines the crop yield. Fluted rollers are the most common feed mechanism employed on conventional grain and fertilizer drills for bulk metering. The construction, operation, and control of the fluted roller feed mechanism are relatively simple and easy. It has a flute roller periphery, and each flute acts as a seed pocket. The seeds are filled in pockets and released at the seed outlet with fixed velocity. The action of discharging seeds, pocket by pocket, results in loss of seed uniformity and uneven flow pattern. Multiple studies reported that discontinuous batch flow was the major constraint of the fluted roller feed mechanism[162–164]. In fluted roller fitted grain drills, farmers often opt for an increased seeding rate to ensure a better yield per unit area, which resulted in either the loss of costly seeds or undesired plant population[165].

The screw conveyors or multi-flight augers have been extensively employed in bulk material handling in agriculture, chemical, processing, construction, and other industries. Jafari (1991)[162] first studied the applicability of a multi-flight screw auger as a feed unit for grain drills. The study fabricated the nine types of screw augers varying in dimensions and tested them on fifteen kinds of bulk material, including common seeds and hollow spheres. A grain flow rate equation as a function of screw auger operational, constructional parameters, and seed properties was developed based on dimensional analysis. The study established a design and construction guidelines for the screw auger as the grain drill feed mechanism. Maleki et al., (2006)[163] developed twelve types of screw augers varying in auger dimension as a metering unit for a wheat grain drill and compared the seed distribution uniformity of the multi-flight auger against the fluted roller. The study found that the auger mechanism had more uniform discharge characteristics than the fluted type. The seed uniformity coefficient was also significantly higher for the auger unit than for the fluted roller. They tested the screw auger having outside diameter of 50 mm and 70 mm to the maximum speed of 30 rpm, so currently, the auger performance at a higher speed is unknown.

The literature survey suggested that the screw auger is an alternative to the fluted roller as a feed mechanism in grain drills. Different augers were developed for bulk metering of grains and tested against varying operational settings, mostly auger rotational speed. However, robotic grain drill operation on sloped and uneven terrain is challenging and introduces a unique variable that has not been previously considered in the literature. In conventional grain drills, an engine-powered tractor provides sufficient drawbar pull to operate a heavy grain drill equipped with a passive tillage tool for furrow opening. In contrast, AGVs are lightweight, often weigh less than 200 kg, and do not have drawbar pull and downforce for furrow creation with passive tillage tools. Therefore, actively powered tillage tools are a suitable option for furrow opening. Powered tools or blades assemblies generates vibration as the tool cuts the grasses, soil and encounters rocks. These induced vibrations would affect the feed mechanism performance, such as seed flow rate and flow uniformity[166]. Hence, the feed unit performance must be tested against the varying vibration levels. Moreover, a robotic drill has to operate on continuously varying sloped or uneven terrain up to 20° (downhill, uphill and side slope). The feed unit inclination would affect the seed flow in the metering unit and its performance; hence, it is essential to assess the feed mechanism performance on varying slope inclination.

This study aimed to design, fabricate, and investigate a multi-flight auger type feed mechanism for wheat drilling on sloped and uneven terrain. The specific objectives of the study were to (1) design and fabricate a multi-flight auger feed unit for a robotic wheat seed drill and, (2) investigate the developed feed mechanism performance at varying speed, vibration, and slope inclination. The developed feed mechanism would be incorporated into the prototype robotic grain drill.

5.3 Materials and methods

5.3.1 Seeder design and fabrication

Physical characteristics of seed

The seed dimension such as length, width, and thickness were essential in designing the auger groove and seeder dimensions. The bulk density of seed affected the seed flowability in the auger groove, and test weight (thousand seed weight) was required to compute the auger flow rate in gram/min. The study selected the wheat seed variety called "Zenda" without seed treatment. The seed variety was primarily grown in the Kansas region (USA). The physical characteristics of wheat, such as dimension (length, width, and thickness), thousand seed weight, and bulk density, were measured as per the procedures mentioned in Badgujar et. al., (2018)[167] from a randomly selected seed batch. Measured characteristics were presented in Table 5.1.

Table 5.1: *Physical characteristics of wheat seed used in the study*

Length (mm)	Width (mm)	Thickness (mm)	Thousand seed weight (g)	Bulk density (kg/m^3)
6.02±0.34	2.99±0.20	2.67±0.19	31.6±0.2	811-809

Auger design parameters

The physical characteristics of wheat seeds were considered for the screw auger design. The ASAE Standard: EP389 (2019)[168] was followed for the auger design and explained as follows.

Inside diameter (d): Nominal inside diameter selection depends upon the drive shaft diameter. A six mm diameter drive shaft (D-shaft) was used to drive the auger, resulted in an auger inside diameter of nine mm with a 1.50 mm wall thickness.

Flighting strip width: The strip width was the depth of the groove which accommodated the seeds. The depth and width of the groove must be greater than the maximum seed dimension for free movement of seed particles inside the auger groove[163]. Length was the maximum dimension of wheat, and the observed average length was 6.02 mm. Therefore, the strip width of 7.60 mm was selected, which was 25% greater than the maximum seed dimension.

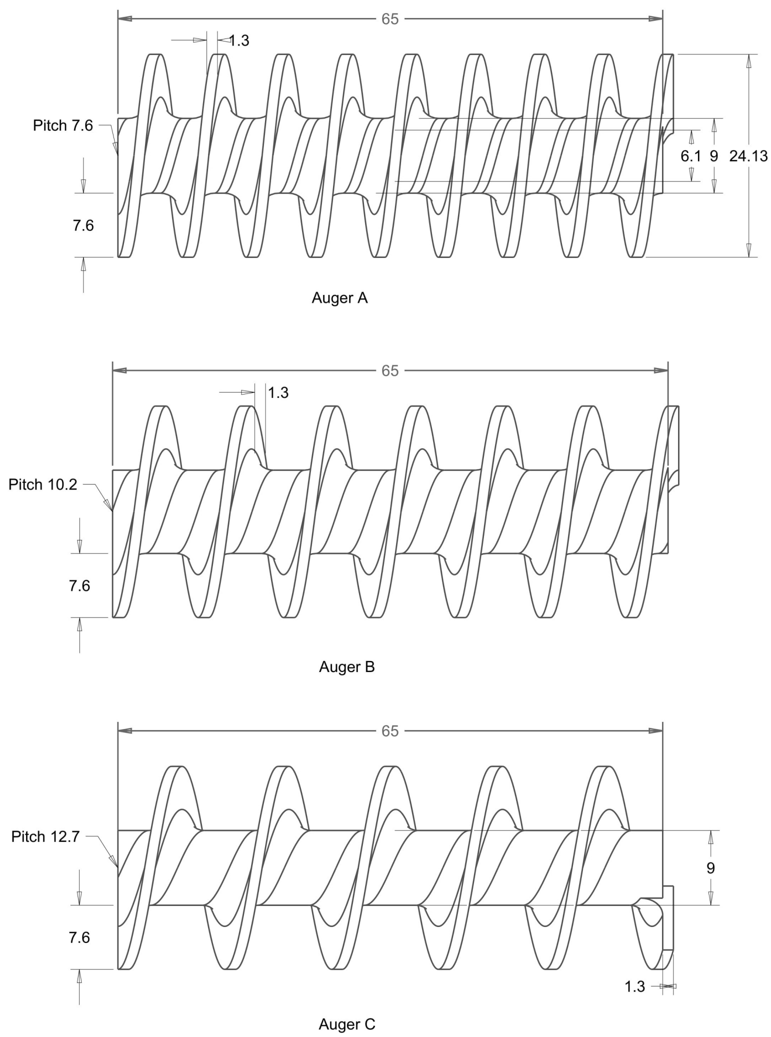

Figure 5.1: *Augers with three different pitches were developed in this study. Figure depicted only left-hand augers (All dimensions in mm)*

Outside diameter (D): The auger size was specified by the auger flight outside diameter.

The outside diameter was determined by adding two times the strip width to the inside diameter (d), which resulted in an outside diameter of 24.2 mm. The length of the auger was 65 mm, and this auger length did not allow the auger to self-discharge when not in motion on flat and side slopes up to 11° .

Pitch of flighting (P): The width of the auger groove was defined by the auger flighting pitch. It was the distance parallel to the shaft axis of one revolution of the flight strip around the center shaft. To prevent seed blockage, the pitch should be greater than the sum of seed width and length[163]. Three different types of augers pitches were used. The selected pitches were 7.60 mm, 10.20 mm, and 12.70 mm, which resulted in an auger with nine, seven, and five flights, respectively, as shown in Figure 5.1. The augers were fabricated with a 3D printer (F410, Fusion3 3D Printers, Greensboro, NC, US) using Thermoplastic Polyurethane (TPU) filament. TPU was a flexible and durable material that would significantly reduce seed damage compared to a hard-plastic material. The flexible material auger flights did not move relative to a point on the shaft while metering wheat, so the effective pitch and strip width were not affected.

Auger housing: The housing was a rectangular box shape. The augers were fitted into the hollow auger housing with 1.5 mm clearance, less than the seed thickness which prevented seed entrapment between auger flighting periphery and the auger housing. The auger housing was 3D printed with a durable hard plastic filament called Acrylonitrile Butadiene Styrene (ABS). The seeder housing was fitted into a readily available and standard aluminum U-channel section with a fixed hole pattern (Actobotics U-channel, Servocity, Winfield, KS, US). An adjustable rectangular seed entrance was located between the bottom of the seed hopper and the top of the housing. Each auger had an independent exit hole for seed discharge located at the bottom, as shown in Figure 5.2. Each exit hole had a seed discharge tube, one on the left and one on the right (Figure 5.2). The U-channel accommodated two auger housings, in which the right-hand and left-hand flighting augers were fitted. The left-auger housing was made of transparent acrylic material. This see-through housing allowed direct observation of seed particle behavior, blockage, and seed flow. The right auger housing was ABS plastic filament and did not allow for seed flow observation. These different housing material types had relatively different surface roughness; therefore, their flow rate was recorded separately, i.e., LH and RH. A gravity seed hopper was attached to the top of the auger housing. The hopper and other seed parts were 3D printed with ABS plastic filament.

Drive assembly: A six mm diameter drive shaft (D-shaft) was used to drive the two augers. The 3D-printed augers were press fitted on the driveshaft, and a separating wall was placed in between these augers. The high torque D.C stepper motor (Nema 23, OMC Corporation Limited, Nanjing City, China) was fixed to one end of the U-channel and connected to the D-shaft with a coupler. At the other end of the U-channel, a rotary encoder (755A Nema, Encoder products company, Sagle, ID, USA) was mounted onto the drive shaft, which measured the auger rotational speed. As desired, the motor speed was controlled by a stepper motor driver (DM542T, OMC Corporation Limited, Nanjing City, China). The auger shaft was supported on three bearings; one was at the center and two at the ends.

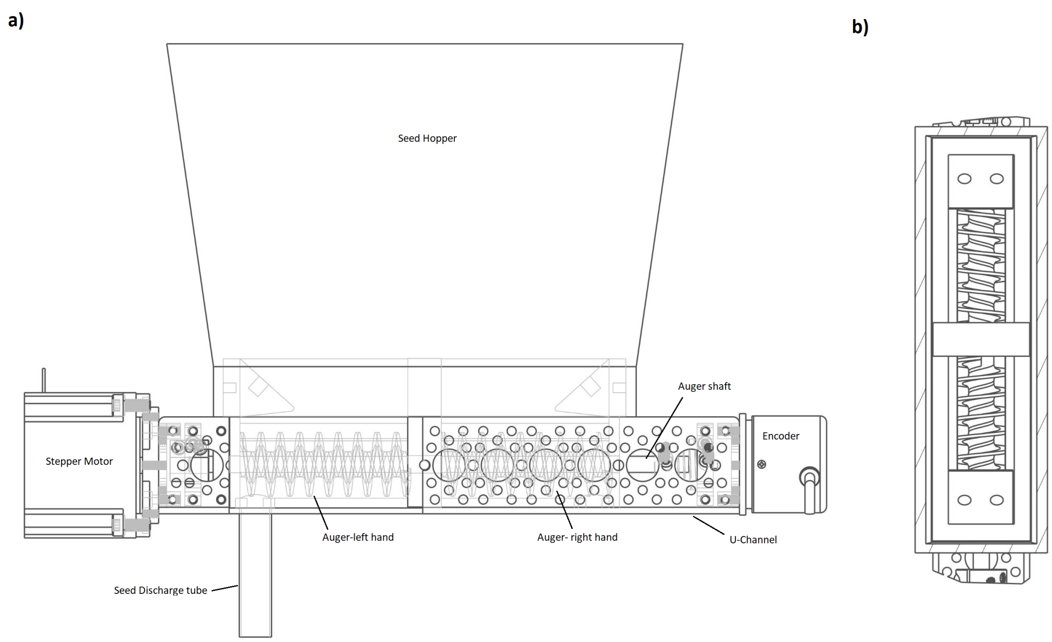

Figure 5.2: *a) Schematic diagram of the feed mechanism showing the main components, b) top cross-sectional view of the auger housing.*

5.3.2 Experimental investigation

Experimental variables

The study included the four predictor variables (n=4), and their levels were listed in Table 5.2. The three different types of augers described above were investigated. Each revolution of the auger flight moved a theoretical volume of material. The auger rotational speed was varied from 10 to 70 rev/min with an 10 rev/min increments. The vibration levels (frequency and amplitude) were decided based on the acceleration data collected from the prototype robotic grain drill during field operation. The source of vibration was motor rpm, soil cutting action of blades, and field irregularities. The collected acceleration data was transformed to the frequency domain from the time domain by applying the Fast-Fourier Transform (FFT). Figure 5.3(a) showed the actual observed acceleration, the vibration frequency was randomly distributed, and there was no dominant frequency observed. However, we noticed the frequency peaks around 6, 22, and 35 Hz. Therefore, we attempted to generate the vibration of frequency around 6 Hz (level 2), 14 Hz (level 3), and 23 Hz (level 4) with higher amplitude, as shown in Figure 5.3(b,c,d). Vibration level 1 included no vibration. The robotic grain drill would be traversing the varying sloped terrain on an uphill, downhill, and side slopes. Hence, the metering unit slope levels included the flat, ascending (uphill), descending (downhill), and side slopes (right slope and left slope). The slope magnitude (11 deg) was decided in accordance with ISO 7256/2[169] and Table 5.2.

The experimental design was divided into two separate procedures, which significantly reduced the number of experiments. Both of the experimental design procedures implemented the Split-Split Plot design. The treatment structure of the first study was arranged in a 3 x 7 x 2 factorial manner with three levels of auger pitch (types A, B, C), seven levels of speed (10, 20, 30, 40, 50, 60, and 70 rev/min), two levels of location (left hand auger, right hand auger) and five replications. In the first design, auger types were randomly assigned to whole plots, then different levels of speed were randomly assigned to subplots within the auger type. Both locations were assigned to each subplot. The total number of experimental units for main plots was 15, for subplots was 105, and for sub-sub-plots was 210. The optimal combination of auger type and speed were fixed according to the application needs (desired flow rate) from the first experiment. The selected auger and speed combination were further studied in the second experimental design to check the influence of vibration and metering unit inclination on flow rate. The treatment structure of the second study was arranged in a 5 x 4 x 2 factorial manner with five levels of slope (flat, asc., desc., left slope, and right slope), four levels of vibration (level 1, level 2, level 3, and level 4), two levels of location (left-hand auger and right-hand auger), and five replications. In the second design, different slopes were randomly assigned to whole plots, then different levels of vibration were randomly assigned to subplots within the slope. Both locations were assigned to each subplot. The total number of experimental units for main plots was 25, for subplots was 100 and for sub-sub-plots 200. For these two studies, analysis of variance tests were conducted to determine if there were any significant difference among the treatment means. All tests were conducted at the 0.05 significance level. The Holm-Tukey multiple means comparison test was used to determine which means were significantly different. Statistical analysis was executed via Statistical Analysis Software (SAS version 9.4; Cary, NC).

Table 5.2: *Experimental variables under the study.*

Predictor				Response
Auger types	Speed, rev/min	Vibration, level (Hz)	Metering unit slope, deg	
Auger A	10, 20,	Level 1 (none)	Flat	Flow rate (g/min)
Auger B	30, 40,	Level 2 (6)	Ascending slope (11)	Flow uniformity, (%)
Auger C	50,	Level 3 (14)	Descending slope (11)	
	60,	Level 4 (24)	Side slope to the left (11)	
	70		Side slope to the right (11)	

Seeder test bench

A seeder test bench was established for feed mechanism testing, which accommodated the necessary instrumentation setup. The test bench allowed control of auger speed, measurement of seed flow rate, and setting the slope and vibration level. A microcontroller (myRio, National Instruments, Austin, TX, USA) was fitted on the test bench. The microcontroller

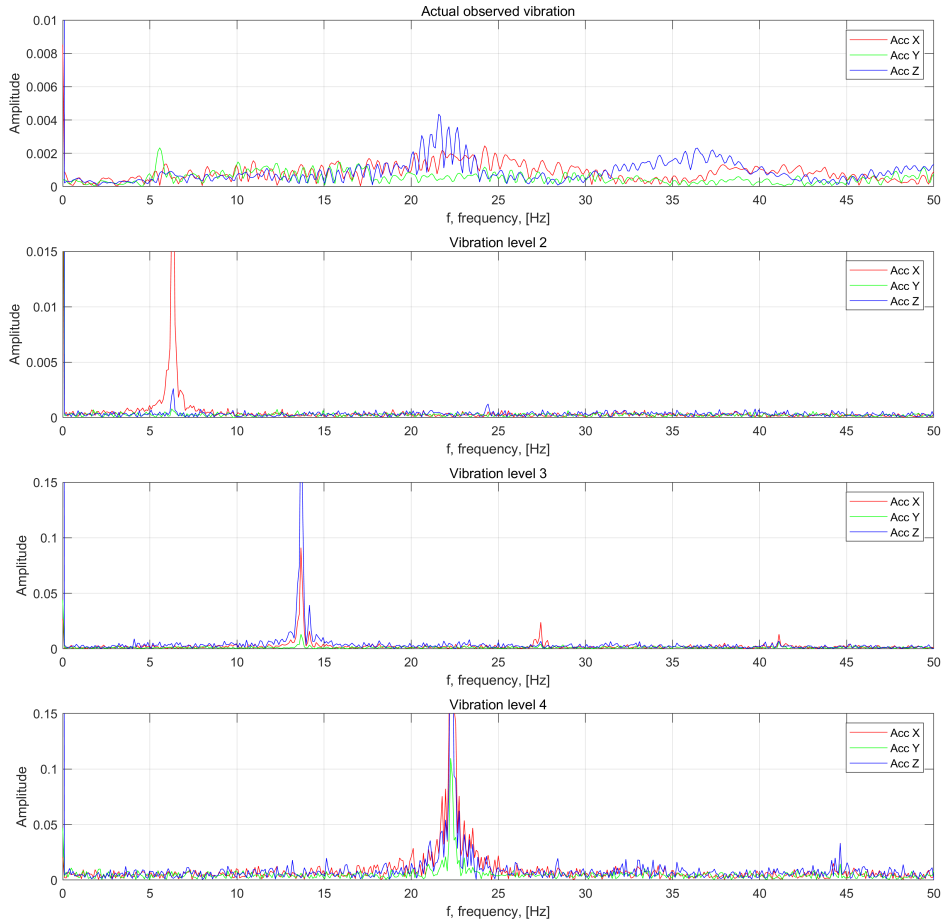

Figure 5.3: *Actual field vibration and experimental levels of vibration. (Note: amplitude in* $g = 9.81\ m/s^2$*)*

controlled the stepper motor driver for auger speed. A straight bar mini load cell (TAL221, Sparkfun Electronics, Boulder, CO, U.S.) with 100 g capacity was used to measure seed weight. The load cell was calibrated (static calibration), and signals were amplified to 0-5 voltage with a load cell amplifier (JY-S60, Calt sensor, Shanghai, China). The amplified load cell signals were recorded by the microcontroller. The test bench setup included the two load cells, one for the left-hand auger (LH) and the other for the right-hand auger (RH). These load cells were part of test bench but not attached directly to test bench. The inclination of the metering unit was manually adjusted with clamping attachments, and a digital protractor (Fowler high precision, Newton, MA, U.S.) was used to measure the feed mechanism inclination. A dual shaft DC electric motor was rigidly mounted in the center of the test bench to generate varying levels of vibrations. Unbalanced center weights were attached to both shafts. As the motor rotated, the unbalanced center weights induced the test bench vibration. The vibration frequency increased with motor speed, and amplitude was adjusted to approximately 0.2 g (where g = $9.81 m/s^2$) by using weights (200g). The test bench vibration was measured with the in-built accelerometer (8 G, 12 bits accuracy) of the microcontroller. The test bench rested on a vibration isolater to reduce the vibration intensity to the ground. A LabView program was developed to control, observe and record the testing procedure.

5.3.3 Seeder testing procedure

The testing procedure for the auger-type feed mechanism was conducted in accordance with ISO 7256/2 (1984)[169], which specified a test method for grain drills (sowing in lines) and permitted the reproducibility of tests. The test procedure aimed to establish the flow rate and the flow uniformity of the feed mechanism under varying rotational speed, slope, and vibration levels. Briefly, the test procedure started with the gravity hopper filled with wheat seeds to a $^3/_4$th level (75 mm depth). During each run, the same hopper level was maintained to eliminate the influence of hopper fill percentage on flow rate. The wheat seeds flowing through the feed mechanism were collected in a trough (material: Styrofoam) placed over the load cell. Two troughs separately collected the seeds from each feed mechanism, i.e., left-hand (LH) and right-hand (RH) augers; called location. Since the metering unit would be installed on an AGV, which would traverse varying slope inclinations, we were interested in knowing how the auger location influenced the flow rate. The load cell cumulatively measured the weight of seeds collected on each trough at a 100 Hz sampling rate throughout each test run. Each test was conducted for a duration of 35 seconds and replicated five times as recommended by ISO 7256/2 (1984)[169]. During the test, the data from the auger speed encoder, load cells measuring seed mass, and vibration in the X, Y, Z plane were time-stamped, recorded by the microcontroller and stored in an external thumb-drive at a frequency of a 100 Hz. The microcontroller was connected to the desktop computer and the LabView program enabled real-time data visualization and control of the test. For each replication, the initial five seconds of data were discarded (initial transient phase), and the remaining 30 seconds of data with 3000 data points were used to compute the flow rate in grams per 30 seconds. The 3000 flow rate values were converted to gram per minute (g/min) for each replication, and the mean flow rate was computed. The flow rate of the left-hand (LH) and the right-hand (RH) auger feed mechanism was calculated and reported independently. The flow uniformity was represented by the coefficient of variation (CV) of flow rate and computed for both left-hand (LH) and right-hand augers (RH).

5.4 Results and discussion

5.4.1 Influence of rotational speed

In the first experiment, the three types of auger performance were investigated in terms of flow rate and flow uniformity (CV) as a function of rotational speed. The influence of auger rotational speed on flow rate and CV was presented in Figures 5.4a and 5.4b. For all augers tested in the study, the flow rate was a linear function of speed. The flow rate of the left-hand auger (A_{LH}, B_{LH}, C_{LH}) and right-hand augers (A_{RH}, B_{RH}, C_{RH}) were closely following the slope line, as shown in Figure 5.4a. The increased auger pitch increased the flow rate; therefore, significantly higher flow rates were observed for augers B and C than for auger A. A few seeds lodged longitudinally in the auger groove (width) for auger A, as shown in Figure 5.5. Therefore, it was recommended that the auger pitch be at least 150% of the maximum seed dimension to avoid seed lodging. The CV of right-hand augers (A_{RH}, B_{RH}, C_{RH}) and left-hand augers (A_{LH}, B_{LH}, C_{LH}) varied from 2-12% and 2-6%, respectively. These CV values were well within acceptable limits for the bulk feed mechanism. Guler (2005)[165] reported that a CV of less than 5% was considered "Very Good", and a CV between 5-10% was regarded as "Good". The CV of right-hand augers was relatively higher than left-hand augers. This could be explained by different auger housing materials (ABS plastics and acrylic material) and their surface roughness. The lower CV was reported at a higher speed (above 50 rpm). At lower speed (less than 40 rpm), the augers flow was not uniform, seeds were discharged pocket by pocket, and a series of discrete steps resembling the staircase was observed, as shown in Figure 5.6.

The statistical analysis of flow rate in the first experiment showed there was no significant three-way interaction among auger type, speed and location (P = 0.278). Also, no significant two-way interaction was observed between auger and location (P=0.070). However, auger ×speed and speed×location two-way interactions were significantly difference (P < 0.01).

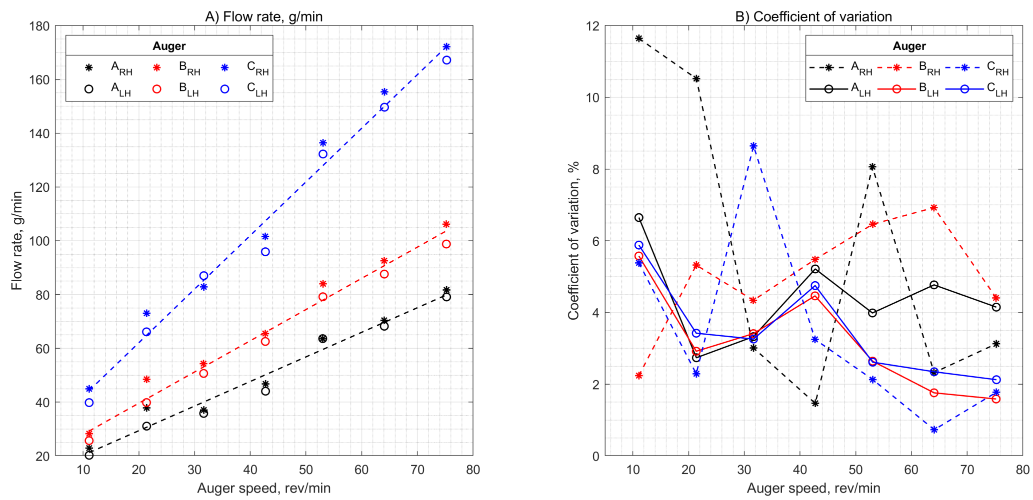

Figure 5.4: *Influence of auger speed (rev/min) on (a) auger flow rate (g/min) and (b) Coefficient of variation*

Table 5.3: *The analysis of variance for wheat flow rate from the first experiment*

Effect	df	F Value	Pr >F
Auger	2	3498.04	<.0001
Speed	6	2588.83	<.0001
Replication	4	3.78	0.0518
Location	1	84.02	<.0001
Auger×Speed	12	152.3	<.0001
Auger× Location	2	2.74	0.0705
Speed×Location	6	3.76	0.0023
Auger×Speed×Location	12	1.23	0.2787

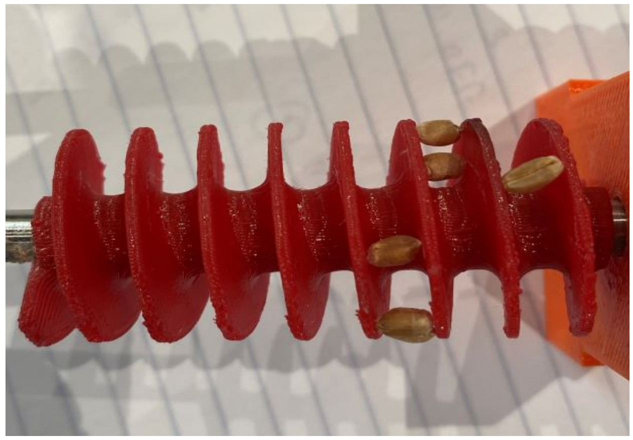

Figure 5.5: *The seed blockage was observed in auger A during the test period*

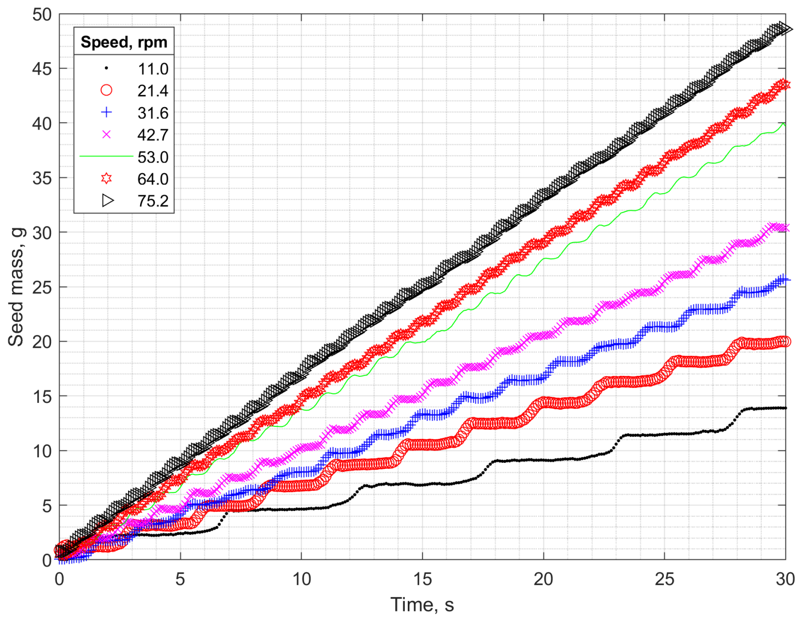

Figure 5.6: *A seed discharge pattern in the first experiment observed with LH auger B during the test period*

The augers A, B, and C delivered the flow rate of around 80, 100, and 170 g/min at 75 rev/min. The AGVs recommended operating speed varies from 1 to 2 km/h (16.6 m/min to 33.2 m/min) on sloping terrain. The recommended wheat seed rate for cattle grazing is 120-180 seeds per meter and varies with the row spacing. The AGV traveling at 1 km/h (16.6 m/min) has to deliver ~2,500 seeds per min (16.6×150 =2,500 seeds) at the seed rate of at 150 seeds/min. The 2,500 seeds weigh around 81.6 grams. The auger B operating at

55 rev/min delivered the 80 g/min seed rate. Therefore, auger B at 55 rev/min was selected to study the influence of vibration and slope in the second experiment.

On sloping terrain, the forward speed of AGV would vary as the slope varies. An established linear relationship between auger rotational speed and flow rate would be used to control the seed rate as the forward speed of AGV changes on sloping hills and uneven terrain. In a commercial application, a control algorithm for the AGV would keep track of forward speed and adjust the auger speed to change the seed rate.

5.4.2 Influence of vibration and slope

There was a significant three-way interaction on flow rate (Table 5.4). Therefore, a multiple comparison procedure was applied to check the conditional effect of vibration and slopes, and the results were presented in Tables 5.5 and 5.6, respectively. The auger flow rate remained nearly constant for vibration level 1, level 2, and level 3 for each given combination of slope and location conditions, as shown in Figure 5.7. However, level 4 showed a significantly increased flow rate. From Figure 5.7 and Table 5.5, it can be concluded that the developed feed mechanism was vibration proof and can handle the vibration frequency up to 14 Hz (level 3). The Holm-Tukey multiple comparison test results were presented in Table 5.5, and a group within a column with a similar mean was assigned a similar letter. The vibration level 1, level 2, and level 3 were assigned the same letter, and a different letter was assigned to level 4 for the given slope.

The mean flow rate between flat, ascending slope (asc.) and descending (desc.) slope did not vary significantly for each combination of vibration and location, as shown in Figure 5.8a and Table 5.6. The flat, ascending, and descending slopes were placed in a similar group for a given vibration level (Table 5.6) except that the flow rate for the ascending slope was slightly higher for level 1 and LH location for level 2. However, the slope to the right (R slope) and slope to the left (L slope) showed significant differences compared to flat (Fig. 5.8b & Table 5.6). When the feed mechanism was inclined towards the right (R slope), the right-side auger (R slope_{RH}) delivered a relatively higher flow rate compared to the left-side auger (R $slope_{LH}$) and vice-versa. The gravity effect could explain this; when inclined to the right slope, the seed in the left side auger had to climb against the gravity, which reduced the flow rate, and for the right-side auger gravity helped increase the flow rate.

In short, the AGV downhill and uphill run would not influence the feed mechanism performance, that was, flow rate. However, operating the seeder on the side slope would significantly influence the performance of the feed mechanism. To compensate for the flow rates on the side slope, we recommend a separate auger drive (D.C. motor), so the seed rate of each auger was independently controlled and adjusted by a controlled algorithm. The CV was presented in Figure 8 and showed that the observed CV was less than 5%, which indicated a flow uniformity of "very good" according to Guler (2005)[165]

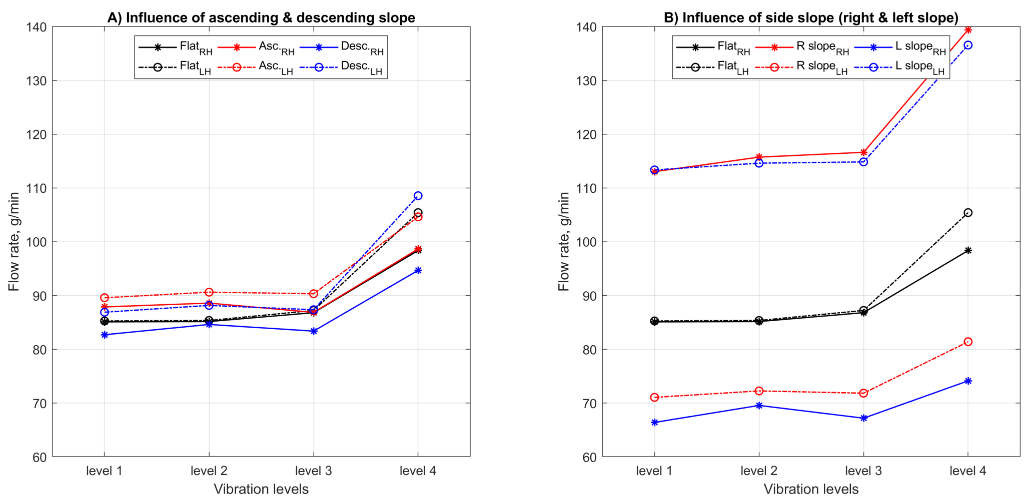

Figure 5.7: *Influence of vibration levels on flow rate at (a) flat, ascending and descending slope (b) flat, side slope i.e., slope to right (R slope) and slope to left (L slope).*

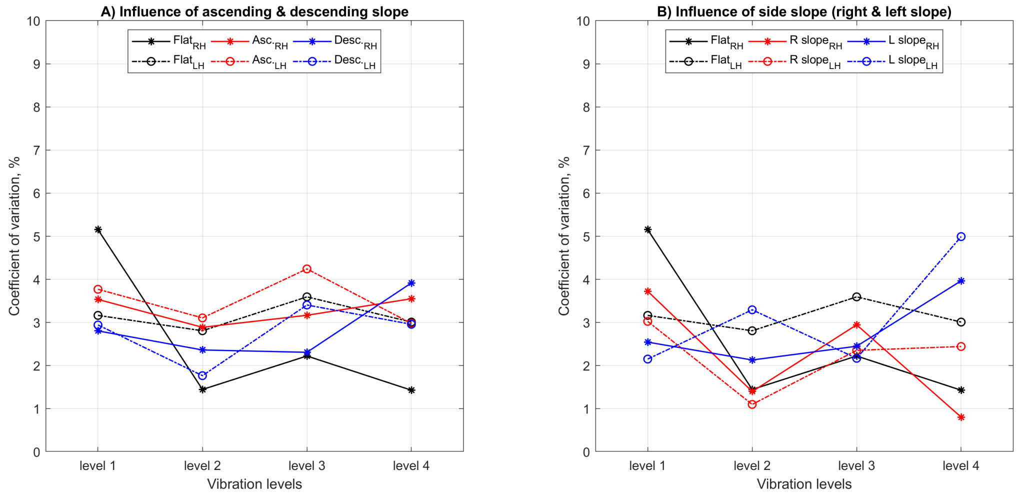

Figure 5.8: *Influence of vibration levels on the CV at a) flat, ascending, and descending slope b) flat, side slope, i.e., slope to the right (R slope) and slope to left (L slope).*

Table 5.4: *The variance analysis for flow rate values for wheat*

Effect	df	F Value	Pr >F
Slope	4	44.26	<.0001
Vibration	3	276.53	<.0001
Location	1	88.48	<.0001
Replication	4	2.4	0.0573
Slope×vibration	12	1.03	0.427
Slope×Location	4	2313.39	<.0001
Vibration×Location	3	11.61	<.0001
Slope×Vibration×Location	12	16.37	<.0001

Table 5.5: *Holm-Tukey multiple comparison test for wheat flow rate (g/min) values (conditional vibration influence)*

	Flat		Asc. slope		Desc. slope		R slope		L Slope	
	LH	RH	LH	RH	LH	RH	LH	RH	LH	RH
Level 1	85.2[a]	85.1a	89.5a	86.8a	86.9a	82.7a	71.0a	113.0a	113.3a	66.4a
Level 2	85.3a	85.2a	90.3a	87.8a	87.3a	83.4a	71.8a	115.7a	114.6a	67.2a
Level 3	87.2a	86.8a	90.6a	88.6a	88.2a	84.6a	72.3a	116.6a	114.8a	69.6ab
Level 4	105.4b	98.4b	104.6b	98.6b	108.5b	94.7b	81.4b	139.4b	136.6b	74.1ab

[a] Means in the same column having the same letter are not significantly different at P<0.05

Table 5.6: *Holm-Tukey multiple comparison test for wheat flow rate (g/min) values (conditional slope influence)*

	Level 1		Level 2		Level 3		Level 4	
	LH	RH	LH	RH	LH	RH	LH	RH
Flat	85.3[a]	85.1ab	85.3a	85.2a	87.2a	86.8a	105.4a	98.4a
Asc. slope	89.6b	87.8b	90.6b	88.6a	90.3a	86.8a	104.6a	98.6a
Desc. slope	86.9a,b	82.7a	88.2ab	84.6a	87.3a	83.4a	108.5a	94.7a
R slope	71.0c	113.0c	72.3c	115.7b	71.8b	116.6b	81.4b	139.4b
L slope	113.3d	66.4d	114.6d	69.5c	114.8c	67.2c	136.5c	74.1c

[a] Means in the same column having same letter are not significantly different at $P<0.05$

5.5 Conclusions

In this study, a screw auger-type feed mechanism was designed, fabrication, and investigated in a laboratory setup for robotic wheat drilling. The performance of the metering device depended upon the physical characteristics of bulk material (seeds), constructional design, and operational parameters. Three different types of screw augers were developed, and a laboratory investigation was carried out on varying auger rotational speed, vibration, and slope. From this study, the following conclusions can be drawn:

- The recommended auger pitch must be at least 150% of the maximum seed dimension to avoid seed lodging in the flighting with corresponding blockage. Hence, augers B and C can be used for a grain drill operation.

- The investigation established the linear relationship between flow rate and auger rotational speed for augers operating on flat, ascending, or descending slopes, which would be essential to control the seed rate on continuously sloping terrain as the slopes would influence the AGV forward speed.

- The auger flow rate should be determined as a function of both side slope and auger speed for proper control of seed rate on side slopes to the left (L slope), or side slope to the right (R slope).

- The coefficient of variation (CV) for flow rate for augers of sufficient pitch (augers B and C) ranged from 2 to 8%. The CV was within the acceptable limits, which was an excellent indicator of the bulk feed mechanism's flow uniformity. The CV of auger B was not affected by slope.

- The feed mechanism was vibration-proof up to a certain frequency, and its performance was unaffected for the vibration frequency up to 14 Hz.
- The study delivered a bulk feed mechanism for a sloped-ground prototype seeder, which can be easily scaled and adopted by small autonomous vehicles or mobile robots.
- The developed feed mechanism would be fitted into the prototype robotic grain drill for seeding on high sloped hills and uneven terrain.

Chapter 6

Summary and conclusions

Arable steep grassland (>6° slopes), hills, or uneven terrain presents difficulties for farming with large conventional agricultural machinery and equipment. The current equipment technology is unsafe and unsuitable to operate on the highly sloped terrain for cultivation. This technological barrier to slope farming has prevented thousands of hectares of arable land from being cultivated, primarily in the United States Great Plains region. Therefore, we proposed a fleet of small AGVs to expand agriculture to marginal, uneven, and highly sloped terrain or grassland. The proposed fleet aims to perform essential agricultural operations ranging from seeding to harvesting on sloping and uneven terrain. Fleets of small AGVs have the potential to significantly increase the land area available for cropping because they can farm the land too steep for conventional large machinery. We predict that a sustainable expansion of wheat production to these steep grasslands and uneven terrain with the help of the proposed robotic fleet would almost double the land area used for this crop from 4% to 7% in the region. It would help in alleviating the 2050 food security goals.

In this study, we employed multiple small AGVs to operate on slopes up to 20°. The successful operation of the proposed AGV fleet on continuously sloping terrain consisted of multiple components. The dissertation dealt with three components or modules: (1) AGV's characteristics analysis, (2) vehicle behavior modeling, and (3) seeder prototype development. The goal of each component, significant findings, and conclusions were briefly discussed below.

6.1 Component 1. AGV's characteristics

The module aimed to lay the foundation for a AGV fleet by determining it's suitability and capabilities and quantifying the physical limits (boundary conditions) for sloped crop work. A standard drawbar pull test was performed in a controlled laboratory soil bin setup. The major findings and conclusions were as follows:

- This component explored the suitability and established the boundary conditions of small size ground vehicles for a high slope farming operation.
- Laid the groundwork for AGV mobility models for high slope terrain operations.
- The AGV generated the drawbar pull equivalent to its weight only on the downhill run for reduced power efficiency.
- The power efficiency of the vehicle varied with slope direction and magnitude. The power efficiency ranged between 7% (18 ° uphill run) to 30% (18 ° downhill run).
- The AGV delivered optimum power efficiency and generated enough drawbar pull with optimum travel reduction and power number.
- The study suggested that the prototype AGV can successfully operate on slopes up to 18°, so high sloped terrain or hills could be farmed with the proposed AGV system.
- **Scholarly work:**
  1. Badgujar, C., Flippo, D., Brokesh, E., & Welch, S. (2022). Experimental Investigation on Traction, Mobility & Energy usage of the Tracked Autonomous Ground Vehicle on a Sloped Soil Bin. Journal of ASABE, 10.13031/ja.14860.
- **Presentation:**
  1. Poster Presentation on *"Traction performance of Autonomous Ground Vehicle on soil bin"*, ASABE Annual International Meeting- 2019, Boston, MA.

2. Poster Presentation on *"Performance of Autonomous Ground Vehicle on varying slope"*, Kansas State University, Research and State-2020, Manhattan, KS.

3. Poster Presentation on *"Performance of Autonomous Ground Vehicle on varying slope"*, 18^{th} Capitol Graduate Research Summit- 2021, Kansas State Capital Building, Topeka, KS.

6.2 Component 2. AGV's predictive behavior models

The vehicle behavior models on a sloping environment are essential for fleet operation, path planning, and control algorithm. Therefore, the AGV's predictive behavior models were developed from the data obtained from laboratory soil bin setup and actual sloping terrain field. For AGV behavior models, a machine learning and deep learning-based approach were implemented. Shallow ANN-based models were developed from the laboratory soil bin setup data. Similarly, deep neural network models were developed from the actual field terrain data. The following conclusions were drawn from this module.

- The component explored the capabilities of machine learning algorithms to simulate the AGV's behavior on sloping terrain.

- Shallow ANNs were fast, accurate, and reliable tools to predict AGV traction performance in a controlled laboratory setup (sloped soil bin).

- Deep neural networks (DNN) were well-suited for predicting AGV field performance in an actual sloping terrain field environment.

- A special model was proposed which combined the multiple DNN with a Gaussian mixture; trained with a hybrid method for data obtained on actual sloping terrain.

- The noisy real-world data obtained from the actual sloped field made it difficult for the machine learning model to learn, particularly for the travel reduction ratio where the single-to-noise ratio was high. Therefore, noise reduction methods were employed for the travel reduction ratio, which ultimately increased the model performance.

- The developed predictive traction models can empower the entire AGV system operation in a dynamic agricultural environment by assisting in vehicle control variables optimization, establishing the vehicle boundary conditions on slopes, energy optimization, and decision making regarding the application feasibility and go-no-go situation ahead of time.

- **Scholarly work:**

  1. Badgujar, C., Flippo, D., & Welch, S. (2022). Artificial neural network to predict traction performance of autonomous ground vehicle on a sloped soil bin and uncertainty analysis. Computers and Electronics in Agriculture, 196:106867, 2022. doi: 10.1016/j.compag.2022.106867.

  2. Badgujar, C., Flippo, D., & Welch, S. (2022). Deep Neural Network-Based Approach to Predict the Traction, Mobility, and Energy Consumption of Autonomous Ground Vehicle on Sloping Terrain Field. Journal of Field Robotics (Under review).

- **Presentation:**

  1. Poster Presentation on *"Artificial neural network to predict traction performance of Autonomous Ground Vehicle on varying slope"*, Kansas State University, Research and State-2021, Manhattan, KS.

  2. Presentation on *"A deep neural network-based approach to predict the traction, mobility and energy consumption of autonomous ground vehicle on sloping terrain."*, ASABE Annual International Meeting- 2022, Houston, TX.

6.3 Component 3. Robotic seeder prototype.

The robotic fleet needed a grain drill that would open up the furrow and disperse the seeds at a pre-determined rate into the furrow while operating on varying sloped terrain. The feed mechanism unit is a crucial component of the seeder, and its design and performance influence the plant population and crop yield. Therefore, we designed and developed a multi-flight auger type feed mechanism and tested it in a laboratory setup against speed, vibration, and slope as control variables.

- The performance of the feed mechanism was influenced by auger speed, vibration, and slope.
- The investigation established the linear relationship between flow rate and auger rotational speed, which would be essential to control the seed rate on continuously sloping terrain as the slopes would influence the AGV forward speed.
- The feed mechanism's performance was unaffected on the flat, downhill, and uphill slopes. However, the side slope significantly affected the feed mechanism's performance, so an appropriate solution was recommended.
- The feed mechanism was vibration-proof up to a specific frequency, and its performance was unaffected for the vibration frequency up to 14 Hz.
- The study delivered a bulk feed mechanism for wheat drilling, which can be easily scaled and adopted by small autonomous vehicles or mobile robots.
- **Scholarly work:**
    1. Badgujar, C., Wu, H., Flippo, D., & Brokesh, E. (2022) Design, Fabrication & Experimental Investigation of Screw Auger Type Feed Mechanism for a Robotic Wheat Drill. Journal of the ASABE. doi: 10.13031/ja.15199.

The dissertation laid the foundation study on robotic farming on marginal and highly sloped land. It provided a valid solution by implementing and adopting the fleet of AGV to expand the agricultural land to uneven and highly sloped marginal terrain, which is unsafe and unsuitable presently. Moreover, the system proved that automation and applied robotics has the potential to solve the emerging problems in the food production system by producing food, fuel, and fiber for the growing population.

Bibliography

[1] United Nations. *World Population Prospects 2019: Highlights.* United Nations, Department of Economic and Social Affairs, Population Division, 2019. ISBN 978-92-1-148316-1.

[2] FAO. How to feed the world in 2050: Food and agriculture organization of the united nations. Technical report, Food and Agriculture Organization of the United Nations, Oct 2009.

[3] C Nelleman, M Macdevette, T Manders, B Eickhout, B Svihus, and A Gerdien Prins. The Environmental Food Crisis: the environment's role in averting future food crises. Technical 978-82-7701-054-0, United Nations, 2009.

[4] BCFN. The challenges of food security - BCFN Foundation. Technical report, Barilla Center For Food & Nutrition, 2010.

[5] C. Sheela Reddy. *Food Security and Food Production: Institutional Challenges in Governance Domain.* Cambridge Scholars Publishing, 2015. ISBN 9781443881579.

[6] Arulbalachandran Dhanarajan. *Sustainable Agriculture towards Food Security.* Springer Singapore, 2017. ISBN 9789811066467. doi: 10.1007/978-981-10-6647-4.

[7] Robert Costanza, Cumberland John H., Herman E. Daly, Robert J. A. Goodland, Richard B. Norgaard, Ida Kubiszewski, and Carol Franco. *An introduction to ecological economics.* CRC Press, Boca Raton, FL, 2015. ISBN 9781566706841.

[8] Pinstrup-Andersen and Rajul Pandya-Lorch. Food security and sustainable use of natural resources: a 2020 vision. *Ecological Economics*, 26(1):1 – 10, 1998. doi: https://doi.org/10.1016/S0921-8009(97)00067-0.

[9] C. Nellemann, M. MacDevette, United Nations Environment Programme, and GRID-Arendal. *The Environmental Food Crisis: The Environment's Role in Averting Future Food Crises : a UNEP Rapid Response Assessment*. Rapid response assessment. UNEP, 2009. ISBN 9788277010540.

[10] J. Popp, Z. Lakner, M. Harangi-Rákos, and M. Fári. The effect of bioenergy expansion: Food, energy, and environment. *Renewable and Sustainable Energy Reviews*, 32:559 – 578, 2014. doi: https://doi.org/10.1016/j.rser.2014.01.056.

[11] Tim Searchinger and Ralph Heimlich. Avoiding Bioenergy Competition for Food Crops and Land. Technical report, Working Paper, Installment 9 of Creating a Sustainable Food Future. Washington, DC: World Resources Institute., 2015.

[12] Carol A. Johnston. Agricultural expansion: land use shell game in the U.S. Northern Plains. *Landscape Ecology*, 29(1):81–95, 2014. ISSN 0921-2973, 1572-9761. doi: 10.1007/s10980-013-9947-0.

[13] N Alexandratos and J Bruinsma. World agriculture: towards 2030/2050 – the 2012 revision . ESA Working paper 12-03., Food and Agriculture Organization of the United Nations, Rome, 2012.

[14] FAO. FAO in the 21st century ensuring food security in a changing world. Technical report, Food and Agriculture Organization of the United Nations, 2011.

[15] G Philip Robertson and Scott M. Swinton. Reconciling agricultural productivity and environmental integrity: a grand challenge for agriculture. *Frontiers in Ecology and the Environment*, 1(3):38–46, 2005.

[16] James Kendrick. *Water-related Technologies for Sustainable Agriculture in U.S. Arid/semiarid Lands*. Congress of the United States, Office of Technology Assessment, 1983. Google-Books-ID: i8iwX5xIWqQC.

[17] Tyler J Lark, J Meghan Salmon, and Holly K Gibbs. Cropland expansion outpaces

agricultural and biofuel policies in the united states. *Environmental Research Letters*, 10(4):044003, 2015. doi: 10.1088/1748-9326/10/4/044003.

[18] W. Gerwin, F. Repmann, S. Galatsidas, D. Vlachaki, N. Gounaris, W. Baumgarten, C. Volkmann, D. Keramitzis, F. Kiourtsis, and D. Freese. Assessment and quantification of marginal lands for biomass production in europe using soil-quality indicators. *Soil*, 4(4):267–290, 2018. doi: 10.5194/soil-4-267-2018.

[19] David Pimentel, David Cerasale, Rose Stanley, Rachel Perlman, Elise Newman, Lincoln Brent, Amanda Mullan, and Debbie Chang. Annual vs. perennial grain production. *Agriculture, Ecosystems & Environment*, 161:1–9, 10 2012. doi: 10.1016/j.agee.2012.05.025.

[20] Shujiang Kang, Wilfred M. Post, Jeff A. Nichols, Dali Wang, Tristram O. West, Varaprasad Bandaru, and Roberto C. Izaurralde. Marginal Lands: Concept, Assessment and Management. *Journal of Agricultural Science*, 5(5):129, 2013. doi: 10.5539/jas.v5n5p129.

[21] Daniel G. Milchunas. Responses of plant communities to grazing in the southwestern United States. *Gen. Tech. Rep. RMRS-GTR-169. Fort Collins, CO: U.S. Department of Agriculture, Forest Service, Rocky Mountain Research Station. 126 p.*, 169, 2006. doi: 10.2737/RMRS-GTR-169.

[22] John B. Doolette and William Magrath. *Watershed development in Asia: strategies and technologies*. World Bank technical paper, No., 127. World Bank, Washington, D.C, 1990.

[23] F. Shaxson. *New Concepts and Approaches to Land Management in the Tropics with Emphasis on Steeplands*. Food and Agriculture Organization of the United Nations, Rome, Italy., 1999. ISBN 9789251043196.

[24] Lucia Vigoroso, Federica Caffaro, and Eugenio Cavallo. Warning against Critical Slopes in Agriculture: Comprehension of Targeted Safety Signs in a Group of Machinery

Operators in Italy. *International Journal of Environmental Research and Public Health*, 16(4), 2019. doi: 10.3390/ijerph16040611.

[25] R. Oberti and A. Shapiro. Advances in robotic agriculture for crops. *Biosystems Engineering*, 146:1–2, 2016. doi: 10.1016/j.biosystemseng.2016.05.010.

[26] Avital Bechar and Clément Vigneault. Agricultural robots for field operations. Part 2: Operations and systems. *Biosystems Engineering*, 153:110–128, 2017. doi: 10.1016/j.biosystemseng.2016.11.004.

[27] Trygve Utstumo, Frode Urdal, Anders Brevik, Jarle Dørum, Jan Netland, Øyvind Overskeid, Therese W. Berge, and Jan Tommy Gravdahl. Robotic in-row weed control in vegetables. *Computers and Electronics in Agriculture*, 154:36–45, 2018. doi: 10.1016/j.compag.2018.08.043.

[28] Wyatt McAllister, Denis Osipychev, Adam Davis, and Girish Chowdhary. Agbots: Weeding a field with a team of autonomous robots. *Computers and Electronics in Agriculture*, 163:104827, 2019. doi: 10.1016/j.compag.2019.05.036.

[29] Baohua Zhang, Yuanxin Xie, Jun Zhou, Kai Wang, and Zhen Zhang. State-of-the-art robotic grippers, grasping and control strategies, as well as their applications in agricultural robots: A review. *Computers and Electronics in Agriculture*, 177:105694, 2020. doi: 10.1016/j.compag.2020.105694.

[30] Azlan Zahid, Md Sultan Mahmud, Long He, Paul Heinemann, Daeun Choi, and James Schupp. Technological advancements towards developing a robotic pruner for apple trees: A review. *Computers and Electronics in Agriculture*, 189:106383, 2021. doi: 10.1016/j.compag.2021.106383.

[31] Daniel Albiero, Angel Pontin Garcia, Claudio Kiyoshi Umezu, and Rodrigo Leme de Paulo. Swarm robots in mechanized agricultural operations: A review about challenges for research. *Computers and Electronics in Agriculture*, 193:106608, 2022. doi: 10.1016/j.compag.2021.106608.

[32] Santosh Pitla, Sreekala Bajwa, Santosh Bhusal, Tom Brumm, Tami Brown-Brandl, Dennis Buckmaster, Isabella Condotta, John Fulton, Todd Janzen, Manoj Karkee, Mario Lopez, Robert Moorhead, Michael Sama, Leon Schumacher, Scott Shearer, and Alex Thomasson. Ground and Aerial Robots for Agricultural Production: Opportunities and Challenges. *Biological Systems Engineering: Papers and Publications*, 2020.

[33] O. Spykman, A. Gabriel, M. Ptacek, and M. Gandorfer. Farmers' perspectives on field crop robots – Evidence from Bavaria, Germany. *Computers and Electronics in Agriculture*, 186:106176, 2021. doi: 10.1016/j.compag.2021.106176.

[34] Latief Ahmad and Syed Sheraz Mahdi. Components of Precision Agriculture. In *Satellite Farming*. Springer International Publishing, 2018. doi: 10.1007/978-3-030-03448-1_2.

[35] Avital Bechar and Clément Vigneault. Agricultural robots for field operations: Concepts and components. *Biosystems Engineering*, 149:94–111, 2016. doi: 10.1016/j.biosystemseng.2016.06.014.

[36] Melvin L. Myers, Henry P. Cole, and Susan C. Westneat. Injury severity related to overturn characteristics of tractors. *Journal of Safety Research*, 40(2):165–170, 2009. doi: 10.1016/j.jsr.2009.02.007.

[37] John R. Myers and Kitty J. Hendricks. Agricultural tractor overturn deaths: Assessment of trends and risk factors. *American Journal of Industrial Medicine*, 53(7): 662–672, 2010. doi: 10.1002/ajim.20775.

[38] Jonathan A. Foley, Navin Ramankutty, Kate A. Brauman, Emily S. Cassidy, James S. Gerber, Matt Johnston, Nathaniel D. Mueller, Christine O'Connell, Deepak K. Ray, Paul C. West, Christian Balzer, Elena M. Bennett, Stephen R. Carpenter, Jason Hill, Chad Monfreda, Stephen Polasky, Johan Rockström, John Sheehan, Stefan Siebert, David Tilman, and David P. M. Zaks. Solutions for a cultivated planet. *Nature*, 478 (7369):337–342, 2011. doi: 10.1038/nature10452.

[39] USDA. The Great Plains including the Black Hills - Grassland, Shrubland and Desert Ecosystems - RMRS, 2020.

[40] Collin Homer, Jon Dewitz, Limin Yang, Suming Jin, Patrick Danielson, George Xian, John Coulston, Nathaniel Herold, James Wickham, and Kevin Megown. Completion of the 2011 National Land Cover Database for the Conterminous United States – Representing a Decade of Land Cover Change Information. *Photogrammetric Engineering and Remote Sensing*, 81(5):346–354, 2015.

[41] Simon Blackmore, Henrik Have, and Spyros Fountas. Specification of Behavioural Requirements for an Autonomous Tractor. In *Automation Technology for Off-Road Equipment Proceedings of the 2002 Conference*. ASABE, 2002. doi: 10.13031/2013.10067.

[42] Pablo Gonzalez-De-Santos, Roemi Fernández, Delia Sepúlveda, Eduardo Navas, and Manuel Armada. Unmanned Ground Vehicles for Smart Farms. In *Agronomy*. IntechOpen, 2020. doi: 10.5772/intechopen.90683.

[43] Luis Emmi, Mariano Gonzalez-de Soto, Gonzalo Pajares, and Pablo Gonzalez-de Santos. New Trends in Robotics for Agriculture: Integration and Assessment of a Real Fleet of Robots. *The Scientific World Journal*, 2014:1–21, 2014. doi: 10.1155/2014/404059.

[44] Pablo Gonzalez-de Santos, Angela Ribeiro, Cesar Fernandez-Quintanilla, Francisca Lopez-Granados, Michael Brandstoetter, Slobodanka Tomic, Stefania Pedrazzi, Andrea Peruzzi, Gonzalo Pajares, George Kaplanis, Manuel Perez-Ruiz, Constantino Valero, Jaime del Cerro, Marco Vieri, Gilles Rabatel, and Benoit Debilde. Fleets of robots for environmentally-safe pest control in agriculture. *Precision Agriculture*, 18(4):574–614, 2017. doi: 10.1007/s11119-016-9476-3.

[45] Santosh K Pitla, Joe D Luck, and Scott A Shearer. Multi-Robot System Control

Architecture (MRSCA) for Agricultural Production. In *2010 Pittsburgh, Pennsylvania*. ASABE, 2010. doi: 10.13031/2013.36212.

[46] Stavros G. Vougioukas. A distributed control framework for motion coordination of teams of autonomous agricultural vehicles. *Biosystems Engineering*, 113(3):284–297, 2012. doi: 10.1016/j.biosystemseng.2012.08.013.

[47] Luis Emmi, Leonel Paredes-Madrid, Angela Ribeiro, Gonzalo Pajares, and Pablo Gonzalez-de-Santos. Fleets of robots for precision agriculture: a simulation environment. *Industrial Robot: An International Journal*, 40(1):41–58, 2013. doi: 10.1108/01439911311294246.

[48] Ralph Alcock. Vehicle Performance. In *Tractor-Implement Systems*. Springer US, 1986. doi: 10.1007/978-1-4684-6879-3_7.

[49] J.Y. Wong. Chapter 6 - performance of off-road vehicles. In *Terramechanics and Off-Road Vehicle Engineering (Second Edition)*. Butterworth-Heinemann, 2010. doi: https://doi.org/10.1016/B978-0-7506-8561-0.00006-3.

[50] Colin Creager, Vivake Asnani, Heather Oravec, and Adam Woodward. Drawbar Pull (DP) Procedures for Off-Road Vehicle Testing. Technical Report NASA/TP-2017-219384, E-19292, GRC-E-DAA-TN31725, NASA, 2017.

[51] David Wettergreen, Scott Moreland, Krzysztof Skonieczny, Dominic Jonak, David Kohanbash, and James Teza. Design and field experimentation of a prototype Lunar prospector. *The International Journal of Robotics Research*, 29(12):1550–1564, 2010. doi: 10.1177/0278364910370217.

[52] Liang Ding, Haibo Gao, Zongquan Deng, Keiji Nagatani, and Kazuya Yoshida. Experimental study and analysis on driving wheels' performance for planetary exploration rovers moving in deformable soil. *Journal of Terramechanics*, 48(1):27–45, 2011. doi: 10.1016/j.jterra.2010.08.001.

[53] Haibo Gao, Weihua Li, Liang Ding, Zongquan Deng, and Zhen Liu. A method for on-line soil parameters modification to planetary rover simulation. *Journal of Terramechanics*, 49(6):325–339, 2012. doi: 10.1016/j.jterra.2012.12.002.

[54] Masataku Sutoh, Junya Yusa, Tsuyoshi Ito, Keiji Nagatani, and Kazuya Yoshida. Traveling performance evaluation of planetary rovers on loose soil. *Journal of Field Robotics*, 29(4):648–662, 2012. doi: 10.1002/rob.21405.

[55] C. Senatore, P. Jayakumar, and K. Iagnemma. Experimental Study of Lightweight Tracked Vehicle Performance on Dry Granular Materials. Technical report, Army Tank Automotive Research Development and Engineering Center Warren, MI, 2013.

[56] Said Al-Milli, Lakmal D. Seneviratne, and Kaspar Althoefer. Track–terrain modelling and traversability prediction for tracked vehicles on soft terrain. *Journal of Terramechanics*, 47(3):151–160, 2010. doi: 10.1016/j.jterra.2010.02.001.

[57] Adam Charles Woodward. *Experimental Analysis of the Effects of the Variation of Drawbar Pull Test Parameters for Exploration Vehicles on GRC-1 Lunar Soil Simulant*. Thesis, Virginia Tech, 2011.

[58] Meng Wang, Chao Wu, Tong Ge, Zhi Min Gu, and Yuan Hong Sun. Modeling, calibration and validation of tractive performance for seafloor tracked trencher. *Journal of Terramechanics*, 66:13–25, 2016. doi: 10.1016/j.jterra.2016.03.001.

[59] W.Y. Park, Y.C. Chang, S.S. Lee, J.H. Hong, J.G. Park, and K.S. Lee. Prediction of the tractive performance of a flexible tracked vehicle. *Journal of Terramechanics*, 45 (1-2):13–23, 2008. doi: 10.1016/j.jterra.2007.11.002.

[60] Laura R. Ray, Devin C. Brande, and James H. Lever. Estimation of net traction for differential-steered wheeled robots. *Journal of Terramechanics*, 46(3):75–87, 2009. doi: 10.1016/j.jterra.2008.03.003.

[61] J. H. Esch, L. L. Bashford, K. Von Bargen, and R. E. Ekstrom. Tractive Performance Comparison Between a Rubber Belt Track and a Four-Wheel-Drive Tractor. *Transactions of the ASAE*, 33(4):1109–1115, 1990. doi: 10.13031/2013.31446.

[62] G. Molari, L. Bellentani, A. Guarnieri, M. Walker, and E. Sedoni. Performance of an agricultural tractor fitted with rubber tracks. *Biosystems Engineering*, 111(1):57 – 63, 2012. doi: https://doi.org/10.1016/j.biosystemseng.2011.10.008.

[63] Alex Keen, Nigel Hall, Peeyush Soni, Madhav D. Gholkar, Simon Cooper, and Jannatul Ferdous. A review of the tractive performance of wheeled tractors and soil management in lowland intensive rice production. *Journal of Terramechanics*, 50(1):45–62, 2013. doi: 10.1016/j.jterra.2012.08.001.

[64] Wan-Soo Kim, Yong-Joo Kim, Seung-Yun Baek, Seung-Min Baek, Yeon-Soo Kim, Yong Choi, Young-Keun Kim, and Il-Su Choi. Traction performance evaluation of a 78-kW-class agricultural tractor using cone index map in a Korean paddy field. *Journal of Terramechanics*, 91:285–296, 2020. doi: 10.1016/j.jterra.2020.08.005.

[65] Ozoemena A. Ani, B.B. Uzoejinwa, A.O. Ezeama, A.P. Onwualu, S.N. Ugwu, and C.J. Ohagwu. Overview of soil-machine interaction studies in soil bins. *Soil and Tillage Research*, 175:13–27, 2018. doi: 10.1016/j.still.2017.08.002.

[66] S. J. Clark and J. B. Liljedahl. Model Studies of Single, Dual and Tandem Wheels. *Transactions of the ASAE*, 12(2):0240–0245, 1969. doi: 10.13031/2013.38808.

[67] R. K. Wood and E. C. Burt. Thrust and Motion Resistance from Soil-Tire Interface Stress Measurements. *Transactions of the ASAE*, 30(5):1288–1292, 1987. doi: 10.13031/2013.30560.

[68] Thomas R Way and Tadashi Kishimoto. Interface Pressures of a Tractor Drive Tyre on Structured and Loose Soils. *Biosystems Engineering*, 87(3):375–386, 2004. doi: 10.1016/j.biosystemseng.2003.12.001.

[69] R.K. Sahu and H. Raheman. Draught Prediction of Agricultural Implements using Reference Tillage Tools in Sandy Clay Loam Soil. *Biosystems Engineering*, 94(2): 275–284, 2006. doi: 10.1016/j.biosystemseng.2006.01.015.

[70] Jude Liu, David A. Lobb, and Ying Chen. Innovative design features of a soil bin to facilitate research on soil-tool interaction. In *2002 ASABE conference Chicago, IL, 2002*, 2002. doi: 10.13031/2013.9374.

[71] TOP 2-2-604. Test Operations Procedure (TOP) 2-2-604 Drawbar Pull. Technical Report :0704-0188, Combat and Automotive Systems Division US Army, Yuma Test Center, AZ, 2007.

[72] William R Gill and Glen E Vanden Berg. *Soil dynamics in tillage and traction*. Agricultural Research Service, U.S. Dept. of Agriculture, Washington, D.C., 1967.

[73] K. Domier and A. Willans. Tractive efficiency–maximum or optimum? *Transactions of the ASAE*, 21(4):650–0653, 1978.

[74] Wan-Soo Kim, Yong-Joo Kim, Seong-Un Park, Kyu-Chul Nam, and Chang-Hyun Choi. Analysis of traction performance for an agricultural tractor according to soil moisture content during plow tillage. In *2019 ASABE conference Boston, MA 2019*, 2019. doi: 10.13031/aim.201900994.

[75] John C. Hayes and James T. Ligon. Traction Prediction Using Soil Physical Properties. *Transactions of the ASAE*, 24(6):1420–1425, 1981. doi: 10.13031/2013.34464.

[76] G. T. Cohron, Nicholas C. Costes, and D. C. Moss. Cone penetration resistance test - An approach to evaluating in-place strength and packing characteristics of lunar soils. 2:1973, 1971.

[77] ASAE Standards. Soil Cone Penetrometer. ASAE S313.3, ASABE Technical Information Library, 2018.

[78] ASAE Standards. Procedures for Using and Reporting Data Obtained with the Soil Cone Penetrometer. EP542.1, ASABE Technical Information Library, 2019.

[79] ASAE Standards. General Terminology for Traction of Agricultural Traction and Transport Devices and Vehicles. ANSI/ASAE S296.5, ASABE Technical Information Library, 2018.

[80] P. W. L. Lyne and E. C. Burt. Real-Time Optimization of Tractive Efficiency. *Transactions of the ASAE*, 32(2):0431–0435, 1989. doi: 10.13031/2013.31021.

[81] Frank Zoz and Robert Grisso. *Traction and Tractor Performance : ASAE Distinguish Series*, volume 27. 2012.

[82] D.R Freitag, A.J Green, and K.J Melzer. Performance evaluation of wheels for lunar vehicles. Technical Report :M-70-4, NASA, 1970.

[83] D.R. Freitag, A.J. Green, K.-J. Melzer, and N.C. Costes. Wheels for lunar vehicles. *Journal of Terramechanics*, 8(3):89–105, 1972. doi: 10.1016/0022-4898(72)90096-1.

[84] Kevin Rooke. Tesla Vehicle Efficiency: The Gold Standard Among EVs, 2020. URL https://www.kevinrooke.com/post/tesla-vehicle-efficiency.

[85] M. Garber. Tractive efficiency of a tracked vehicle. *Journal of Agricultural Engineering Research*, 32(4):359–368, 1985. doi: 10.1016/0021-8634(85)90100-3.

[86] Peter J. Gregory and Timothy S. George. Feeding nine billion: the challenge to sustainable crop production. *Journal of Experimental Botany*, 62(15):5233–5239, 2011. doi: 10.1093/jxb/err232.

[87] Florian Zabel, Ruth Delzeit, Julia M. Schneider, Ralf Seppelt, Wolfram Mauser, and Tomáš Václavík. Global impacts of future cropland expansion and intensification on agricultural markets and biodiversity. *Nature Communications*, 10(1):2844, 2019. doi: 10.1038/s41467-019-10775-z.

[88] Pablo Gonzalez-De-Santos, Roemi Fernández, Delia Sepúlveda, Eduardo Navas, and Manuel Armada. Unmanned Ground Vehicles for Smart Farms. In *Agronomy - Climate Change and Food Security*. IntechOpen, 2020. doi: 10.5772/intechopen.90683.

[89] L. García-Pérez, M. C. García-Alegre, A. Ribeiro, and D. Guinea. An agent of behaviour architecture for unmanned control of a farming vehicle. *Computers and Electronics in Agriculture*, 60(1):39–48, 2008. doi: 10.1016/j.compag.2007.06.004.

[90] Luis Emmi, Mariano Gonzalez-de Soto, Gonzalo Pajares, and Pablo Gonzalez-de Santos. New Trends in Robotics for Agriculture: Integration and Assessment of a Real Fleet of Robots. *The Scientific World Journal*, 2014:1–21, 2014. doi: 10.1155/2014/404059.

[91] Jesús Conesa-Muñoz, Mariano Gonzalez-de Soto, Pablo Gonzalez-de Santos, and Angela Ribeiro. Distributed Multi-Level Supervision to Effectively Monitor the Operations of a Fleet of Autonomous Vehicles in Agricultural Tasks. *Sensors*, 15(3):5402–5428, 2015. doi: 10.3390/s150305402.

[92] Ni Li, Charles Remeikas, Yunjun Xu, Suhada Jayasuriya, and Reza Ehsani. Task Assignment and Trajectory Planning Algorithm for a Class of Cooperative Agricultural Robots. *Journal of Dynamic Systems, Measurement, and Control*, 137(051004), 2015. doi: 10.1115/1.4028849.

[93] Chi Zhang, Noboru Noguchi, and Liangliang Yang. Leader–follower system using two robot tractors to improve work efficiency. *Computers and Electronics in Agriculture*, 121:269–281, 2016. doi: 10.1016/j.compag.2015.12.015.

[94] Jianping Hu, Xiaoyue Yan, Jun Ma, Chunhui Qi, Kumi Francis, and Hanping Mao. Dimensional synthesis and kinematics simulation of a high-speed plug seedling transplanting robot. *Computers and Electronics in Agriculture*, 107:64–72, 2014. doi: 10.1016/j.compag.2014.06.004.

[95] Lin Haibo, Dong Shuliang, Liu Zunmin, and Yi Chuijie. Study and Experiment on a Wheat Precision Seeding Robot. *Journal of Robotics*, 2015:1–9, 2015. doi: 10.1155/2015/696301.

[96] Sneha A. Amrita, E. Abirami, A. Ankita, R. Praveena, and R. Srimeena. Agricultural Robot for automatic ploughing and seeding. In *2015 IEEE Technological Innovation in ICT for Agriculture and Rural Development (TIAR)*, Chennai, 2015. IEEE. doi: 10.1109/TIAR.2015.7358525.

[97] Manuel Pérez-Ruíz, David C. Slaughter, Fadi A. Fathallah, Chris J. Gliever, and Brandon J. Miller. Co-robotic intra-row weed control system. *Biosystems Engineering*, 126:45–55, 2014. doi: 10.1016/j.biosystemseng.2014.07.009.

[98] Keun Ha Choi, Sang Kwon Han, Sang Hoon Han, Kwang-Ho Park, Kyung-Soo Kim, and Soohyun Kim. Morphology-based guidance line extraction for an autonomous weeding robot in paddy fields. *Computers and Electronics in Agriculture*, 113:266–274, 2015. doi: 10.1016/j.compag.2015.02.014.

[99] Zhao De-An, Lv Jidong, Ji Wei, Zhang Ying, and Chen Yu. Design and control of an apple harvesting robot. *Biosystems Engineering*, 110(2):112–122, 2011. doi: 10.1016/j.biosystemseng.2011.07.005.

[100] Zhiguo Li, Pingping Li, Hongling Yang, and Yuqing Wang. Stability tests of two-finger tomato grasping for harvesting robots. *Biosystems Engineering*, 116(2):163–170, 2013. doi: 10.1016/j.biosystemseng.2013.07.017.

[101] S.S. Mehta and T.F. Burks. Vision-based control of robotic manipulator for citrus harvesting. *Computers and Electronics in Agriculture*, 102:146–158, 2014. doi: 10.1016/j.compag.2014.01.003.

[102] S. Se, D.G. Lowe, and J.J. Little. Vision-based global localization and mapping for mobile robots. *IEEE Transactions on Robotics*, 21(3):364–375, 2005. doi: 10.1109/TRO.2004.839228.

[103] Gustav Jagbrant, James Patrick Underwood, Juan Nieto, and Salah Sukkarieh. *LiDAR Based Tree and Platform Localisation in Almond Orchards*, pages 469–483. Springer International Publishing, 2015. doi: 10.1007/978-3-319-07488-7_32.

[104] Gokhan Bayar, Marcel Bergerman, A. Bugra Koku, and E. ilhan Konukseven. Localization and control of an autonomous orchard vehicle. *Computers and Electronics in Agriculture*, 115:118–128, 2015. doi: 10.1016/j.compag.2015.05.015.

[105] E. C. Burt, C. A. Reaves, A. C. Bailey, and W. D. Pickering. A Machine for Testing Tractor Tires in Soil Bins. *Transactions of the ASAE*, 23(3):0546–0547, 1980. doi: 10.13031/2013.34620.

[106] Serafettin Ekinci, Kazım Carman, and Humar Kahramanlı. Investigation and modeling of the tractive performance of radial tires using off-road vehicles. *Energy*, 93:1953–1963, 2015. doi: 10.1016/j.energy.2015.10.070.

[107] Z.X. Zhu, R. Torisu, J.I. Takeda, E.R. Mao, and Q. Zhang. Neural Network for estimating Vehicle Behaviour on Sloping Terrain. *Biosystems Engineering*, 91(4):403–411, 2005. doi: 10.1016/j.biosystemseng.2005.05.003.

[108] D.R. Freitag. A dimensional analysis of the performance of pneumatic tires on clay. *Journal of Terramechanics*, 3(3):51–68, January 1966. ISSN 00224898. doi: 10.1016/0022-4898(66)90106-6.

[109] R. D. Wismer and H. J. Luth. Off-Road Traction Prediction for Wheeled Vehicles. *Transactions of the ASAE*, 17(1):0008–0010, 1974. doi: 10.13031/2013.36772.

[110] R.N. Yong and E.A. Fattah. Prediction of wheel-soil interaction and performance using the finite element method. *Journal of Terramechanics*, 13(4):227–240, 1976. doi: 10.1016/0022-4898(76)90044-6.

[111] J.Y. Wong. Computer aided analysis of the effects of design parameters on the performance of tracked vehicles. *Journal of Terramechanics*, 23(2):95–124, 1986. doi: 10.1016/0022-4898(86)90017-0.

[112] Ashmore Colin, Eddie C. Burt, and John L. Turner. An Empirical Equation for Predicting Tractive Performance of Log-Skidder Tires. *Transactions of the ASAE*, 30 (5):1231–1236, 1987. doi: 10.13031/2013.30550.

[113] M.J. Dwyer. Prediction of drawbar test performance. *Journal of Terramechanics*, 24 (2):169–177, 1987. doi: 10.1016/0022-4898(87)90007-3.

[114] S.K. Upadhyaya, D. Wulfsohn, and G. Jubbal. Traction prediction equations for radial ply tyres. *Journal of Terramechanics*, 26(2):149–175, 1989. doi: 10.1016/0022-4898(89) 90004-9.

[115] Z. Wang and K. W. Domier. Prediction of Drawbar Performance for a Tractor With Dual Tires. *Transactions of the ASAE*, 32(5):1529–1533, 1989. doi: 10.13031/2013. 31184.

[116] H Nakashima and A Oida. Algorithm and implementation of soil–tire contact analysis code based on dynamic FE–DE method. *Journal of Terramechanics*, 41(2-3):127–137, 2004. doi: 10.1016/j.jterra.2004.02.002.

[117] V.K. Tiwari, K.P. Pandey, and P.K. Pranav. A review on traction prediction equations. *Journal of Terramechanics*, 47(3):191–199, 2010. doi: 10.1016/j.jterra.2009.10.002.

[118] Idris Idris Sunusi, Jun Zhou, Zhen Zhen Wang, Chenyang Sun, Ibrahim Eltayeb Ibrahim, Samwel Opiyo, Tchalla korohou, Shakeel Ahmed Soomro, Nura Alhaji Sale, and Olanrewaju T.O. Intelligent tractors: Review of online traction control process. *Computers and Electronics in Agriculture*, 170:105176, 2020. doi: 10.1016/j.compag.2019.105176.

[119] J. Y. Wong. *Terramechanics and off-road vehicle engineering: Terrain behavior, off-road vehicle performance and design.* Elsevier, Oxford, 2010.

[120] Yanbo Huang, Yubin Lan, Steven J. Thomson, Alex Fang, Wesley C. Hoffmann, and Ronald E. Lacey. Development of soft computing and applications in agricultural and

biological engineering. *Computers and Electronics in Agriculture*, 71(2):107–127, 2010. doi: 10.1016/j.compag.2010.01.001.

[121] A.S. Tohmaz and A.E. Hassan. Application of artificial neural networks to skidder traction performance. *Journal of Terramechanics*, 32(3):105–114, 1995. doi: 10.1016/0022-4898(95)00010-0.

[122] Hamid Taghavifar and Aref Mardani. Application of artificial neural networks for the prediction of traction performance parameters. *Journal of the Saudi Society of Agricultural Sciences*, 13(1):35–43, 2014. doi: 10.1016/j.jssas.2013.01.002.

[123] Hamid Taghavifar and Aref Mardani. Use of artificial neural networks for estimation of agricultural wheel traction force in soil bin. *Neural Computing and Applications*, 24 (6):1249–1258, 2014. doi: 10.1007/s00521-013-1360-8.

[124] Hamid Taghavifar, Aref Mardani, and Ashkan Haji Hosseinloo. Appraisal of artificial neural network-genetic algorithm based model for prediction of the power provided by the agricultural tractors. *Energy*, 93:1704–1710, 2015. doi: 10.1016/j.energy.2015.10.066.

[125] Salim Almaliki, Reza Alimardani, and Mahmoud Omid. Artificial Neural Network Based Modeling of Tractor Performance at Different Field Conditions. *Agricultural Engineering International: CIGR Journal*, 18(4):262–274, 2016.

[126] S.M. Shafaei, M. Loghavi, and S. Kamgar. An extensive validation of computer simulation frameworks for neural prognostication of tractor tractive efficiency. *Computers and Electronics in Agriculture*, 155:283–297, 2018. doi: 10.1016/j.compag.2018.10.027.

[127] Katarzyna Pentoś, Krzysztof Pieczarka, and Krzysztof Lejman. Application of Soft Computing Techniques for the Analysis of Tractive Properties of a Low-Power Agricultural Tractor under Various Soil Conditions. *Complexity*, 2020:1–11, 2020. doi: 10.1155/2020/7607545.

[128] Rafael Marcé, Marta Comerma, Juan Carlos García, and Joan Armengol. A neuro-fuzzy modeling tool to estimate fluvial nutrient loads in watersheds under time-varying human impact. *Limnology and Oceanography: Methods*, 2(11):342–355, 2004. doi: https://doi.org/10.4319/lom.2004.2.342.

[129] Roohollah Noori, Gholamali Hoshyaripour, Khosro Ashrafi, and Babak Nadjar Araabi. Uncertainty analysis of developed ANN and ANFIS models in prediction of carbon monoxide daily concentration. *Atmospheric Environment*, 44(4):476–482, 2010. doi: 10.1016/j.atmosenv.2009.11.005.

[130] Majid Dehghani, Bahram Saghafian, Farzin Nasiri Saleh, Ashkan Farokhnia, and Roohollah Noori. Uncertainty analysis of streamflow drought forecast using artificial neural networks and Monte-Carlo simulation. *International Journal of Climatology*, 34 (4):1169–1180, 2014. doi: https://doi.org/10.1002/joc.3754.

[131] Davor Antanasijević, Viktor Pocajt, Aleksandra Perić-Grujić, and Mirjana Ristić. Modelling of dissolved oxygen in the Danube River using artificial neural networks and Monte Carlo Simulation uncertainty analysis. *Journal of Hydrology*, 519:1895–1907, 2014. doi: 10.1016/j.jhydrol.2014.10.009.

[132] Jeongwoo Lee, Chul-Gyum Kim, Jeong Eun Lee, Nam Won Kim, and Hyeonjun Kim. Medium-Term Rainfall Forecasts Using Artificial Neural Networks with Monte-Carlo Cross-Validation and Aggregation for the Han River Basin, Korea. *Water*, 12(6):1743, 2020. doi: 10.3390/w12061743.

[133] Katarzyna Pentoś and Krzysztof Pieczarka. Applying an artificial neural network approach to the analysis of tractive properties in changing soil conditions. *Soil and Tillage Research*, 165:113–120, 2017. doi: 10.1016/j.still.2016.08.005.

[134] Wenyan Wu, Graeme C. Dandy, and Holger R. Maier. Protocol for developing ANN models and its application to the assessment of the quality of the ANN model de-

velopment process in drinking water quality modelling. *Environmental Modelling & Software*, 54:108–127, April 2014. doi: 10.1016/j.envsoft.2013.12.016.

[135] M.T. Hagan and M.B. Menhaj. Training feedforward networks with the Marquardt algorithm. *IEEE Transactions on Neural Networks*, 5(6):989–993, 1994. doi: 10.1109/72.329697.

[136] Hao Yu and Bogdan M. Wilamowski. Levenberg–marquardt training. In *Intelligent Systems*, pages 12–1–12–16. CRC Press, 2 edition, 2018. ISBN 9781315218427. doi: 10.1201/9781315218427-12.

[137] Leo Breiman and Philip Spector. Submodel selection and evaluation in regression. The x-random case. *International Statistical Review / Revue Internationale de Statistique*, 60(3):291, 1992. doi: 10.2307/1403680.

[138] Rudy Setiono. Feedforward neural network construction using cross validation. *Neural Computation*, 13(12):2865–2877, 2001. doi: 10.1162/089976601317098565.

[139] Mansour Talebizadeh, Saeid Morid, Seyyed Ali Ayyoubzadeh, and Mehdi Ghasemzadeh. Uncertainty Analysis in Sediment Load Modeling Using ANN and SWAT Model. *Water Resources Management*, 24(9):1747–1761, July 2010. doi: 10.1007/s11269-009-9522-2.

[140] Evdokia Tapoglou, Emmanouil A. Varouchakis, and George P. Karatzas. Uncertainty estimations in different components of a hybrid ANN - Fuzzy - Kriging Model for water table level simulation. In *13th International Conference on Hydroinformatics*, 2018.

[141] Meng Gao, Liting Yin, and Jicai Ning. Artificial neural network model for ozone concentration estimation and Monte Carlo analysis. *Atmospheric Environment*, 184:129–139, 2018. doi: 10.1016/j.atmosenv.2018.03.027.

[142] Karim C. Abbaspour, Jing Yang, Ivan Maximov, Rosi Siber, Konrad Bogner, Johanna Mieleitner, Juerg Zobrist, and Raghavan Srinivasan. Modelling hydrology and water

quality in the pre-alpine/alpine Thur watershed using SWAT. *Journal of Hydrology*, 333(2-4):413–430, 2007. doi: 10.1016/j.jhydrol.2006.09.014.

[143] Lucia Vigoroso, Federica Caffaro, and Eugenio Cavallo. Warning against Critical Slopes in Agriculture: Comprehension of Targeted Safety Signs in a Group of Machinery Operators in Italy. *International Journal of Environmental Research and Public Health*, 16(4):611, 2019. doi: 10.3390/ijerph16040611.

[144] Ramon Gonzalez and Karl Iagnemma. Slippage estimation and compensation for planetary exploration rovers. State of the art and future challenges. *Journal of Field Robotics*, 35(4):564–577, 2018. doi: 10.1002/rob.21761.

[145] Tianyou Guo, Junlong Guo, Bo Huang, and Huei Peng. Power consumption of tracked and wheeled small mobile robots on deformable terrains–model and experimental validation. *Mechanism and Machine Theory*, 133:347–364, 2019. doi: 10.1016/j.mechmachtheory.2018.12.001.

[146] Matt Heverly, Jaret Matthews, Justin Lin, Dan Fuller, Mark Maimone, Jeffrey Biesiadecki, and John Leichty. Traverse Performance Characterization for the Mars Science Laboratory Rover: Traverse Performance Characterization - Mars Science Laboratory Rover. *Journal of Field Robotics*, 30(6):835–846, 2013. doi: 10.1002/rob.21481.

[147] Ramon Gonzalez, Dimi Apostolopoulos, and Karl Iagnemma. Slippage and immobilization detection for planetary exploration rovers via machine learning and proprioceptive sensing. *Journal of Field Robotics*, 35(2):231–247, 2018. doi: 10.1002/rob.21736.

[148] Ramon Gonzalez, Samuel Chandler, and Dimi Apostolopoulos. Characterization of machine learning algorithms for slippage estimation in planetary exploration rovers. *Journal of Terramechanics*, 82:23–34, 2019. doi: 10.1016/j.jterra.2018.12.001.

[149] Kazım Çarman and Alper Taner. Prediction of Tire Tractive Performance by Using Artificial Neural Networks. *Mathematical and Computational Applications*, 17(3):182–192, 2012. doi: 10.3390/mca17030182.

[150] Chetan Badgujar, Daniel Flippo, and Stephen Welch. Artificial neural network to predict traction performance of autonomous ground vehicle on a sloped soil bin and uncertainty analysis. *Computers and Electronics in Agriculture*, 196:106867, 2022. doi: 10.1016/j.compag.2022.106867.

[151] Christopher Fisher. Using an Accelerometer for Inclination Sensing | Analog Devices. Application Note AN-1057, Analog Devices, 2010.

[152] Kostantinos N Plataniotis and Dimitris Hatzinakos. Gaussian mixtures and their applications to signal processing. *Advanced signal processing handbook*, pages 89–124, 2017.

[153] Ian Goodfellow, Yoshua Bengio, and Aaron Courville. *Deep learning*. MIT press, 2016.

[154] Peyman Setoodeh, Saeid Habibi, and Simon Haykin. *Expectation Maximization*, pages 185–201. 2022. doi: 10.1002/9781119078166.ch10.

[155] Celeux Gilles, Forbes Florence, and Peyrard Nathalie. EM procedures using mean field-like approximations for Markov model-based image segmentation. *Pattern Recognition*, 36(1):131–144, 2003. doi: https://doi.org/10.1016/S0031-3203(02)00027-4.

[156] Ryo Yoshida and Mike West. Bayesian learning in sparse graphical factor models via variational mean-field annealing. *J Mach Learn Res*, 11:1771–1798, 2010.

[157] Georgios Arvanitidis. *Geometrical Aspects of Manifold Learning*. PhD thesis, Technical University of Denmark, 2019.

[158] Bruce A. Robertson and Patrick J. Doran. Biofuels and Biodiversity: The Implications of Energy Sprawl. In *Encyclopedia of Biodiversity*, pages 528–539. Elsevier, 2013. doi: 10.1016/B978-0-12-384719-5.00341-5.

[159] Peter Potapov, Svetlana Turubanova, Matthew C. Hansen, Alexandra Tyukavina, Viviana Zalles, Ahmad Khan, Xiao-Peng Song, Amy Pickens, Quan Shen, and Jocelyn Cortez. Global maps of cropland extent and change show accelerated crop-

land expansion in the twenty-first century. *Nature Food*, 3(1):19–28, 2022. doi: 10.1038/s43016-021-00429-z.

[160] Tyler J. Lark, Seth A. Spawn, Matthew Bougie, and Holly K. Gibbs. Cropland expansion in the United States produces marginal yields at high costs to wildlife. *Nature Communications*, 11(1):4295, 2020. doi: 10.1038/s41467-020-18045-z.

[161] Great Plains Center for Agricultural Health. Tractor overturns promoting and protecting the safety & health of farm workers & their families. Technical report, The University of Iowa College of Public Health, 2014.

[162] J F Jafari. A Study of the Metering of Free Flowing Particulate Solids Using Multi-Flight Screws. *Proceedings of the Institution of Mechanical Engineers, Part E: Journal of Process Mechanical Engineering*, 205(2):113–121, 1991. doi: 10.1243/PIME_PROC_1991_205_209_02.

[163] M. R. Maleki, J. F. Jafari, M. H. Raufat, A. M. Mouazen, and J. De Baerdemaeker. Evaluation of Seed Distribution Uniformity of a Multi-flight Auger as a Grain Drill Metering Device. *Biosystems Engineering*, 94(4):535–543, 2006. doi: 10.1016/j.biosystemseng.2006.04.003.

[164] Yuxiang Huang, Botao Wang, Yuxiang Yao, Shangpeng Ding, Junchang Zhang, Ruixiang Zhu, and College of Mechanical and Electric Engineering, Northwest A&F University, Yangling 712100, Shaanxi, China. Parameter optimization of fluted-roller meter using discrete element method. *International Journal of Agricultural and Biological Engineering*, 11(6):65–72, 2018. doi: 10.25165/j.ijabe.20181106.3573.

[165] I Guler. Effects of flute diameter, fluted roll length, and speed on alfalfa seed flow. *Applied Engineering in Agriculture*, 21(1):5–7, 2005.

[166] M. G. Boydas and N. Turgut. Effect of Vibration, Roller Design, and Seed Rates on the Seed Flow Evenness of a Studded Feed Roller. *Applied Engineering in Agriculture*, 23(4):413–418, 2007. doi: 10.13031/2013.23482.

[167] C M Badgujar, H S Dhingra, G S Manes, R Khurana, and Anand Gautam. Engineering properties of okra (*Abelmoschus esculentus*) seed. *Agricultural Research Journal*, 55 (4):722, 2018. doi: 10.5958/2395-146X.2018.00131.X.

[168] ASAE Standards. Auger flighting design considerations. EP389.2, ASABE Technical Information Library, 2019.

[169] ISO Standards . Sowing equipment- test methods- part 2: seed drills for sowing in lines- 7256/2. Technical report, International organization for standardaziation, 1984.